

# REPORT DOCUMENTATION PAGE

*Form Approved*  
**OMB No. 0704-0188**

Public reporting burden for this collection of information is estimated to average 1 hour per response, including the time for reviewing instructions, searching existing data sources, gathering and maintaining the data needed, and completing and reviewing this collection of information. Send comments regarding this burden estimate or any other aspect of this collection of information, including suggestions for reducing this burden to Department of Defense, Washington Headquarters Services, Directorate for Information Operations and Reports (0704-0188), 1215 Jefferson Davis Highway, Suite 1204, Arlington, VA 22202-4302. Respondents should be aware that notwithstanding any other provision of law, no person shall be subject to any penalty for failing to comply with a collection of information if it does not display a currently valid OMB control number. PLEASE DO NOT RETURN YOUR FORM TO THE ABOVE ADDRESS.

<b>1. REPORT DATE (DD-MM-YYYY)</b> September 30, 2006		<b>2. REPORT TYPE</b> Final Progress Report		<b>3. DATES COVERED (From - To)</b> 5/1/2001 – 9/30/2006	
<b>4. TITLE AND SUBTITLE</b> Center for Research on Infrared Detectors (CENTROID)				<b>5a. CONTRACT NUMBER</b>	
				<b>5b. GRANT NUMBER</b> DAAD19-01-1-0462	
				<b>5c. PROGRAM ELEMENT NUMBER</b>	
<b>6. AUTHOR(S)</b> Professor Pallab Bhattacharya (Solid State Electronics Laboratory, Electrical And Computer Science Department, University of Michigan, 1301 Beal Avenue, Ann Arbor, MI 48109-2122)				<b>5d. PROJECT NUMBER</b>	
				<b>5e. TASK NUMBER</b>	
				<b>5f. WORK UNIT NUMBER</b>	
<b>7. PERFORMING ORGANIZATION NAME(S) AND ADDRESS(ES)</b> Regents of the University of Michigan 1053 Wolverine Tower – DRDA 3003 S State Street Ann Arbor, MI 48109-1274				<b>8. PERFORMING ORGANIZATION REPORT</b>  UM# 041529 / F004488	
<b>9. SPONSORING / MONITORING AGENCY NAME(S) AND ADDRESS(ES)</b> U. S. Army Research Office Attn: AMSRL-RO-BI (TR) P O Box 12211 Research Triangle Park, 27709-2211 NC 27709-2211				<b>10. SPONSOR/MONITOR'S ACRONYM(S)</b> ARO	
				<b>11. SPONSOR/MONITOR'S REPORT NUMBER(S)</b> 42211.22-EL-mur	
<b>12. DISTRIBUTION / AVAILABILITY STATEMENT</b> Approved for public release, distribution unlimited.					
<b>13. SUPPLEMENTARY NOTES</b> The views, opinions and/or findings contained in this report are those of the author(s) and should not be construed as an official Department of the Army position, policy or decision, unless so designated by other documentation.					
<b>14. ABSTRACT</b> The proposed objectives of the five year MURI contract for the Microphysics Laboratories (MPL) were as follows: (1) detailed investigation of the origin and control of various defects in mercury cadmium telluride heteroepitaxial structures grown on cadmium zinc telluride substrates by molecular beam epitaxy; (2) identification and control over lifetime-limiting defects to achieve material homogeneity over large areas; (3) establishment of a reproducible method to grow high quality multi-layer device structures suitable for SWIR/MWIR two-color detector arrays and fabrication of test detectors; and (4) transfer of a reproducible technology to industrial partners, HgCdTe layers with low defect density and long lifetime suitable for multi-color detector arrays. The results and achievements obtained during the past five years are discussed in detail in our final progress report under the headings of: (1) scientific progress and accomplishments, (2) interactions with ARO and other DoD personnel, (3) technology transfer/initiatives, and (4) student training.					
<b>15. SUBJECT TERMS</b> Integrated Circuits.                      Semiconductors.                      Solid-State Electronics.					
<b>16. SECURITY CLASSIFICATION OF:</b>			<b>17. LIMITATION OF ABSTRACT</b>	<b>18. #OF PAGES</b>  Cover + 106pg	<b>19a. NAME OF RESPONSIBLE PERSON</b>
<b>a. REPORT</b>	<b>b. ABSTRACT</b>	<b>c. THIS PAGE</b>			<b>19b. TELEPHONE NUMBER</b> (include area code)



---

**Army Research Office MURI Program**

*Center for Research on Infrared Detectors*  
**(CENTROID)**

**DAAD19-01-1-0462 (UM# 041529)**

**Final Progress Report**  
**Prepared September 30, 2006**



## Final Progress Report

1. **Title of Project:** Center for Research of Infrared Detectors (CENTROID)
2. **Grant Number:** DAAD19-01-1-0462
3. **Period Covered by Report:** 05/01/2001 – 09/30/2006
4. **Name of Institution:** University of Michigan, Ann Arbor
5. **Principle Investigator:** Pallab Bhattacharya
6. **Scientific Progress and Accomplishments:**

### **I. Fundamental Research on MBE-grown $\text{Hg}_{1-x}\text{Cd}_x\text{Te}$ (Sivananthan, Grein and Smith)**

#### ***A. Introduction and Overview***

The principal role of the Microphysics Laboratory of the University of Illinois at Chicago in the ARO-MURI program was to establish standardized portable techniques for the fully controllable and optimized Molecular Beam Epitaxial (MBE) growth of HgCdTe. The proposed objectives of the five year MURI contract for the Microphysics Laboratories (MPL) were as follows: (1) detailed investigation of the origin and control of various defects in mercury cadmium telluride heteroepitaxial structures grown on cadmium zinc telluride substrates by molecular beam epitaxy; (2) identification and control over lifetime-limiting defects to achieve material homogeneity over large areas; (3) establishment of a reproducible method to grow high quality multi-layer device structures suitable for SWIR/MWIR two-color detector arrays and fabrication of test detectors; and (4) transfer of a reproducible technology to industrial partners, HgCdTe layers with low defect density and long lifetime suitable for multi-color detector arrays. The results and achievements obtained during the past five years are discussed in detail below under the headings of: (1) scientific progress and accomplishments, (2) interactions with ARO and other DoD personnel, (3) technology transfer/initiatives, and (4) student training.

#### ***B. Selected Scientific Progress and Accomplishments***

##### **Identified and resolved some key issues in the MBE growth of HgCdTe**

###### ***Substrate screening***

With the aid of Dr. J. Markunas, Dr. S. Lewis and Dr. J. H. Dinan of the US Army Night Vision and Electronic Sensors Directorate (NVESD), we performed extensive screening measurements on commercially purchased CdZnTe substrates. So far, 12 substrates have been tested. 5 of them (41.7%) show large area crystalline imperfections, as shown in Fig. 1(a) and (b); 3 of them (25%) show moderate areas of crystalline imperfections, as shown in Fig. 1(c); and only 4 of them (33.3%) show reasonably good surface crystalline perfection, as shown in Fig. 1(d). We also demonstrated that all substrate defects are likely to be transferred directly to

the HgCdTe epilayer if no effective interfacial layer is present, as is shown in Fig. 2<sup>1</sup> Without an effective interfacial layer, a high density of threading dislocation and short defect-mediated carrier recombination lifetimes in HgCdTe epilayers are very likely to be obtained. The substrate quality is clearly an important bottleneck limiting the improvement of the MBE HgCdTe growth yield. We have been working with NVESD and Brookhaven National Laboratory to further develop interfacial layers and hope that they will be capable of effectively blocking substrate crystalline imperfections to enhance the HgCdTe MBE growth yield.

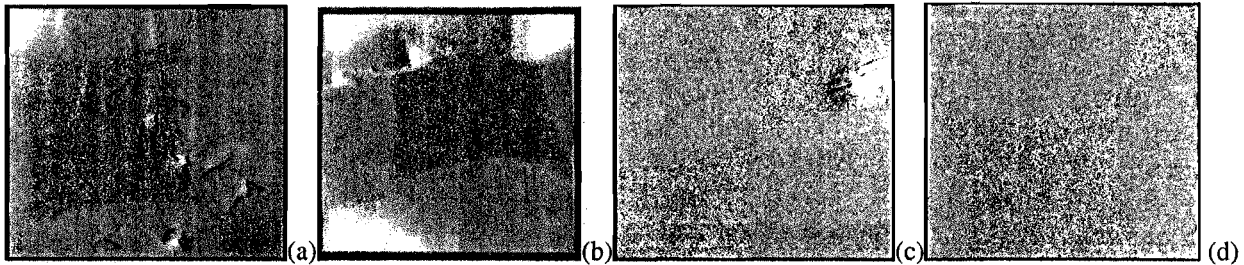


Fig. 1 Typical X-ray topographic mapping measurement results from our commercially purchased CdZnTe wafers (a) and (b) show poor crystalline perfection, (c) shows a substrate with small area of poor crystalline quality and (d) a reasonably good sample. (Measured by Dr. J. Markunas, Dr. S. Lewis and Dr. J. H. Dinan from the US Army NVSED)

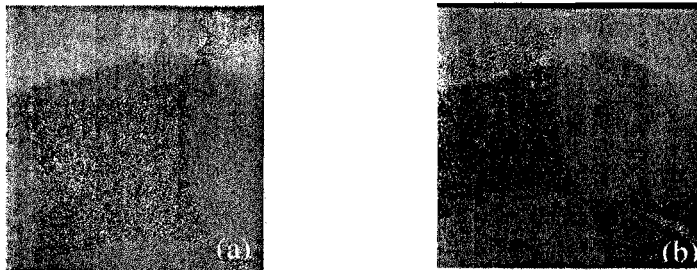


Fig. 2 X-ray topographic mapping measurement results from one CdZnTe wafers (a) and (b) after MBE HgCdTe growth, which shows that all defective features on the substrate are one-to-one transferred to the HgCdTe epilayer after MBE growth. (Measured by Dr. J. Markunas, Dr. S. Lewis and Dr. J. H. Dinan from the US Army NVSED)

### Optimization of the sample mounting configuration

The standard mounting arrangement for MBE substrates is a contactless configuration, in which the sample is fastened to a molybdenum ring. 3" CdTe/Si substrates were not used for the MURI program, which focuses uniquely on growth on CdZnTe substrates. However, they are included in the discussion for the sake of completeness. 3" samples can be either (i) directly exposed to the heating radiation, or (ii) juxtaposed to a diffuser plate. In the former case, the sample is heated by irradiation, whereas in the latter mainly by conduction. Smaller area substrates, such as CdZnTe, are (iii) mounted using a molybdenum spring plate that holds the substrate in contact with a diffuser plate, which faces the heater. The heating power is determined by a closed-loop feedback involving a thermocouple, which floats in the gap between

<sup>1</sup> H. Abad, J. Zhao, G. Badano, Y. Chang, S. Sivananthan, Correlation of Pre-growth Surface Morphology of CdZnTe Substrates with the Quality of HgCdTe Epilayers, Military Sensing Symposium, 22-26 March 2004, Tucson, Arizona

heater and sample. Its readings are related both to the heater and sample temperatures, and in some cases even to the temperature of the cells. Thus, it might not indicate the actual temperature of the substrate. Therefore the grower of  $\text{Hg}_{1-x}\text{Cd}_x\text{Te}$  (MCT) faces a serious problem of temperature stabilization during the growth, since MCT is characterized by a small growth window *vis-à-vis* other MBE-grown materials.

It is experimentally observed that in case (i) one has to ramp the heater temperature down<sup>2</sup>, whereas in cases (ii) and (iii) (which have some similarity to mounting on a full molybdenum block) a temperature increase is necessary to keep the real sample temperature constant<sup>3</sup>.

Case (i) has been the most widely investigated, especially for III-V MBE-grown materials<sup>4-5</sup>. Here the temperature transient is believed to stem from the fact that the substrate is largely transparent to infrared radiation, whereas the growing material is not. Thus the energy absorption of the sample increases strongly with the deposition of material, which results in an increase in sample temperature during growth.

If the sample heating mechanism is not irradiation but conduction, as in cases (ii) and (iii), material deposition results in a temperature decrease, because the emissivity of the front face will increase. On the other hand, the radiant energy coming from the effusion cells (common to (ii) and (iii)) can increase the sample and substrate temperatures, especially at nucleation, when temperature stability is especially essential to achieving good crystalline quality<sup>6</sup>.

For these reasons, numerous *in-situ* sensors have been used to measure the HgCdTe temperature *in situ*, such as (a) Spectroscopic Ellipsometry (SE)<sup>7</sup>, (b) *in-situ* FTIR Spectroscopy<sup>8</sup>, (c) Dynamic Reflectance Spectroscopy<sup>9</sup> and ABES<sup>10</sup>, both on II-VI and III-V materials. In the case of MCT, measurements of type (c) must be carried out from the back face of the sample, and generally require the deposition of a reflecting intermediate layer. It has been shown that good reproducibility can be attained from SE, even though one of the limits of the current analysis method is that it gives no direct information on the growth temperature. All optical techniques, except for SE<sup>11</sup>, share the same limitation, namely that the MCT has to be optically thick in order to give reliable readings. In this project, we have mainly relied on the indirect information provided by SE and RHEED spectra to assess the temperature stability, since no sensor except SE and RHEED has so far shown the ability to monitor growth nucleation.

### *Thermodynamic equivalent growth conditions*

<sup>2</sup> G. Brill, S. Velicu, Y. Chen, N. K. Dhar, T. S. Lee, Y. Selamet, and S. Sivananthan (in press).

<sup>3</sup> S. Sivananthan, PhD Thesis, University of Illinois at Chicago, 1988.

<sup>4</sup> B. V. Shanabrook, J. R. Waterman, J.L Davis and R. J. Wagner, Appl. Phys. Lett. **61** (19), 2338-40, 1992

<sup>5</sup> B. V. Shanabrook, J. R. Waterman, J.L Davis, R. J. Wagner and D. S. Katzer, J. Vac. Sci. Technol. B, **11**(3), 1993, 994-997

<sup>6</sup> P. Thompson, Y. Li, J. Zhou, D. I. Sato, L. Flanders, and H. P. Lee, Appl. Phys. Lett., **70** (12) 1997, 1605-07

<sup>7</sup> L.A. Almeida, N.K. Dhar, M. Martinka, and J.H. Dinan, *Journal of Electronic Materials*, **29** (2000), pp. 754-759

<sup>8</sup> M. Daraselia, C.H. Grein, R. Rujirawat, B. Yang, S. Sivananthan, F. Aqariden and S. Shih, *Journal of Electronic Materials*, **28** (1999) pp. 743-748

<sup>9</sup> T. P. Pearsall et al, Rev. Sci. Instrum. **66** (10), 1995, 4977- 4980

<sup>10</sup> T. J. de Lyon, J. A. Roth and D.H. Chow, J. Vac. Sci. Technol., B **15**(2), 1997, 329-331

<sup>11</sup> M. Daraselia, PhD thesis and private communication.

Based on the thermodynamic model of Gailliard and Colin<sup>12</sup>, Piquette, *et al.*<sup>13</sup> suggested a formula that predicts the substrate temperature for optimized growth relative to a reference value as a function of the Hg flux, composition, and growth rate:  $T_S \cong T_R / (1 + T_0 / T_R \cdot \ln A^*)$ . Here,  $T_0$  is a constant incorporating several material thermal parameters, including enthalpy and entropy constants, which is roughly equal to  $12400\text{K}^{13}$ , and  $T_R$  is a reference temperature defined to be the optimal growth temperature for a particular set of reference conditions (flux, composition, and growth rate).  $A^*$  is defined by  $A^* = [v J_R (1-x)] / [v_R J_{Hg} (1-x_R)]$ , where  $v$  is the growth rate,  $v_R$  is the reference growth rate,  $x$  is the composition,  $x_R$  is the composition of the sample grown under reference conditions,  $J_{Hg}$  is the Hg flux and  $J_R$  is the Hg flux under reference conditions. In actual HgCdTe MBE growth, the Hg flux is measured and expressed by the beam equivalent pressure of the corresponding flux gauge ( $P_{Hg}$ ), which has a linear relationship with the actual flux, thus we get the result:

$$\log_{10} \left( \frac{P_{Hg}}{v(1-x)} \right) - \log_{10} \left( \frac{P_{Hg_R}}{v_R(1-x_R)} \right) = -\log_{10} e \cdot T_0 \left( \frac{1}{T_S} - \frac{1}{T_R} \right) = -5385.25 \cdot \left( \frac{1}{T_S} - \frac{1}{T_R} \right).$$

The same result can also be obtained based on MPL/UIC's thermodynamical model. This equation shows that all thermodynamically equivalent growth conditions near the optimized growth conditions will lie on a single line with a slope of -5385.25 on a graph of  $\log_{10} [P_{Hg} / v(1-x)]$  vs.  $1/T$ . Please see Ref.14 for a detailed discussion. If one can identify a particular set of optimized growth conditions, all other optimized growth conditions must lie on the same line, even with different compositions, growth rates, Hg fluxes and/or growth temperatures. We also introduce a parameter  $D$  that measures the distance between this optimal line and another line parallel to it.  $D$  is defined by the equation  $D = (Y_i - Y_R) / 5385.25 + (1/T_i - 1/T_R)$ , where  $Y_i = \log_{10} [P_{Hg_i} / v_i(1-x_i)]$   $i = 1, R$ , and measures the distance between the actual growth conditions and the line defining optimal growth conditions. It can be used *in situ* to control the growth. One can calculate  $D$  to determine whether the growth is good or not, and can use that value of  $D$  to determine the changes in growth parameters which would give optimal growth conditions. The  $D$  value is determined by the growth rate, composition and temperature. The growth rate can be obtained from *in situ* spectroscopic ellipsometry (SE) by fitting the dynamic model in the beginning stage of growth,  $x$  is also monitored *in situ* by SE, and  $T$  is measured by a thermocouple, a pyrometer and indirectly by the heating power and is calibrated by SE in the beginning stage of growth. All of these parameters can be acquired *in situ*. Moreover, these *in situ* parameters can be correlated one to another. However, considering the existence of errors in the *in situ* data acquisition, they are measured by different techniques in order to obtain the redundancy useful in making the *in situ* growth control system as reliable as possible. This is particularly useful for the growth of sophisticated multilayer detector structures.

### *Identification and investigation of the origin and control of various surface defects in HgCdTe*

#### *a) Crater defects (also called void or, V-shaped defects)*

Figs 3 to 5 show typical crater defects. Some porous polycrystalline material was found inside the larger voids, characterized by random or aligned patterns, as is shown in Fig. 5. EDX

<sup>12</sup> T. Colin and T. Skauli, J. Electron. Mater. 26, 688 (1997)

<sup>13</sup> E. C. Piquette, M. Zandian, D. D. Edwall, and J. M. Arias, J. Electron. Mater., 30, 637 (2001)

<sup>14</sup> Y. Chang, G. Badano, J. Zhao, C. H. Grein, S. Sivananthan, T. Aoki, and David. J. Smith, Appl. Phys. Lett., 83, 4785(2003)

measurements were performed at different positions in the vicinity of the large void defect shown in Fig. 6 to determine the stoichiometric properties of the material. The results, given in Table 1, show that the material inside the voids examined is highly nonstoichiometric.

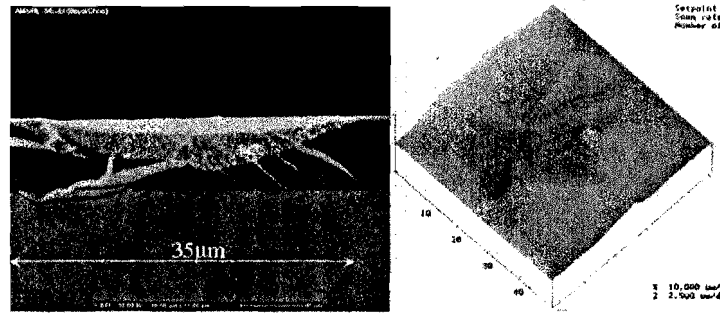


Fig.3. SEM and AFM photos of a large crater defect that shows distinguished edges and shape.

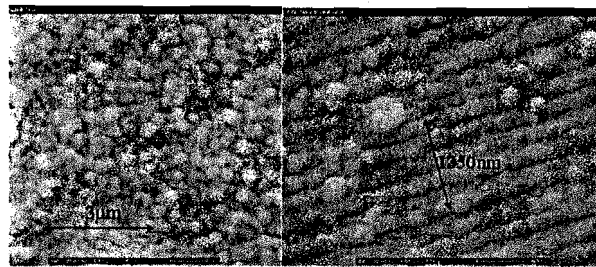


Fig. 4. SEM photographs of the porous polycrystalline material inside void defects.

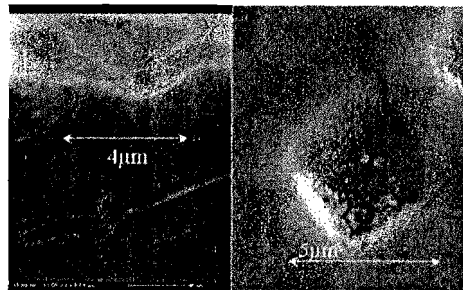


Fig. 5. SEM photographs of small void defects that show undistinguished edges.

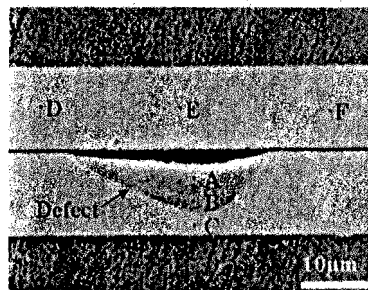


Fig. 6. Cross sectional SEM photograph of a void defect from EDX measurements. Each labeled measurement position corresponds with the data shown in Table 1.

Table 1. DX results for each position inside or nearby the void defect shown in Fig. 6

	Hg %	Cd %	Te %	(Hg%+Cd%)/Te%
A	12.3	23.0	64.7	54.6%
B	9.4	25.5	65.1	53.6%
C	33.6	16.3	50.1	99.6%
D	35.2	15.8	49.0	104.1%
E	34.7	15.2	50.1	99.6%
F	35.6	15.2	49.2	103.2%

Based on the aforementioned thermodynamic model, we found our samples with surface crater defects to correspond to growth conditions in the lower left part of a  $\log_{10}\left(\frac{P_{Hg}}{\nu(1-x)}\right)$  vs.  $\frac{1}{T}$  graph, as shown in Fig. 7, namely below the line which goes through the optimized growth conditions. This region corresponds to “Te-rich” conditions when compared with samples possessing good surface morphology and grown under optimized conditions. He *et al.*<sup>15,16,17</sup> reported the existence of an empirical regularity when they plotted their growth data on a graph with  $T$  as the abscissa and the Hg to Te pressure ratio ( $P_{Hg}/P_{Te}$ ) as the ordinate. Specifically, all their data showed that those layers with surface crater defects only appeared in the lower right part of the graph, namely in the area with higher temperature and lower Hg flux. In contrast, microtwins were found in the opposite quadrant of the diagram.

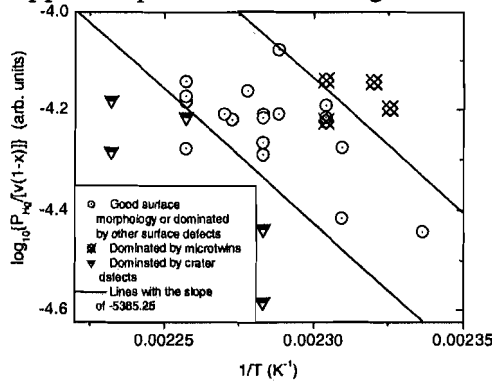


Fig. 7.  $\log_{10}\left(\frac{P_{Hg}}{\nu(1-x)}\right)$  vs.  $1/T$  graph of MBE grown HgCdTe with different composition, growth rate and growth temperatures. The lines have a slope of -5385.25 and thus are parallel to the line giving optimal growth conditions. The positions of the lines are for the aid of eyes.

If a first order Taylor series is used for small changes in composition, growth rate and growth temperature, the  $\log_{10}\left(\frac{P_{Hg}}{\nu(1-x)}\right)$  vs.  $1/T$  graph is similar to a  $P_{Hg}/P_{Te}-T$  graph with the direction of the abscissa reversed. The observation of He *et al.* that any deviation of the growth conditions toward lower Hg flux or a higher temperature triggered the formation of crater void

<sup>15</sup> L. He, Y. Wu, L. Chen, S. L. Wang, M. F. Yu, Y. M. Qiao, J. R. Yang, Y. J. Li, R. J. Ding and Q. Y. Zhang, *J. Cryst. Growth*, 227, 677 (2001)

<sup>16</sup> L. Chen, Y. Wu, M. F. Yu, S. L. Wang, Y. M. Qiao and L. He, *J. Infrared Millim. Waves*, 20, 406 (2001)

<sup>17</sup> L. He, Y. Wu, L. Chen, M. F. Yu, J. Wu, J. R. Yang, Y. J. Li, R. J. Ding and Q. Y. Zhang, in *Materials for Infrared Detectors II*, R. E. Longshore and S. Sivanathan, Editor, *Proceedings of SPIE Vol. 4795*, 17 (2002)

defects thus is in good agreement with our observation and model. Crater void defects were also found by several other authors<sup>18,19</sup> on the surfaces of samples grown at higher substrate temperature or a low Hg flux.

Equation (3) shows that variations of composition or growth rate, in addition to temperature and Hg flux, can trigger the formation of surface crater defects. When growth is performed under low Hg flux or the temperature is so high that the Hg sticking coefficient on the surface is low<sup>20</sup>, excess Te atoms exist on the surface. Excess Te atoms on the reacting surface hinder the Te<sub>2</sub> dissociation rate so that the probability of Te<sub>2</sub> existing on the reacting surface is dramatically increased. However, if the growth temperature is too low, the Te<sub>2</sub> dissociation rate decreases. Even if the increased surface Hg atom density at lower temperatures (due to an increased sticking coefficient<sup>19</sup>) pushes Te atoms to form HgCdTe and tends to decrease the Te<sub>2</sub> molecular density, the slow Te<sub>2</sub> dissociation rate still makes Te<sub>2</sub> a stable molecule on the reacting surface. Te<sub>2</sub> cannot directly react with Hg or Cd to form HgCdTe before dissociation; instead, it is more likely to form metallic Te. The dissociation energy of an isolated Te<sub>2</sub> molecule is 54.2kcal, which is reduced to 10 kcal at a monolayer step on a HgCdTe crystal surface<sup>21</sup>. If a Te<sub>2</sub> molecule sticks to a surface with some contamination, or Te precipitates are present on the substrate, it will be difficult to dissociate Te<sub>2</sub>.

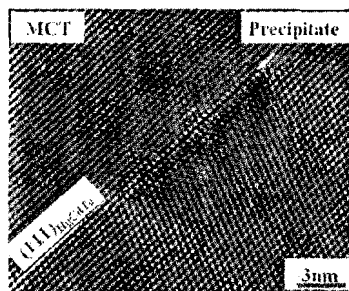


Fig. 8. High-resolution cross-sectional electron micrograph of a Te precipitate. The plane of the precipitate lies along the  $\langle 111 \rangle$  direction and is almost coherent with the HgCdTe lattice due to nearby lattice relaxation.

Our TEM measurements<sup>22</sup> have also already revealed that the surface crater defects originate primarily within the HgCdTe films, and are associated with the local development of a polycrystalline morphology. Within a surface crater defect, crystals of both HgCdTe and Te continue to nucleate, with HgCdTe grains being either semicoherent or incoherent to the Te grains. EDX data also confirmed the existence of elemental Te in the surface crater defects. It appears that molecular Te<sub>2</sub> plays an important role in the formation of crater defects. TEM observations conclude that the densities of Te precipitates are relatively low near crater void defects. A high-resolution cross-sectional TEM image of a Te precipitate at an atomic scale is shown in Fig. 8. This micrograph shows that the plane of the precipitate is aligned along the  $\langle 111 \rangle$  direction and is almost coherent with the HgCdTe lattice. The distance between adjacent

<sup>18</sup> D. Chandra, H. D. Shih, F. Aqariden, R. Dat, Gutzler, M. J. Bevan, and T. Orent, *J. Electron. Mater.* 27, 640 (1998)

<sup>19</sup> J. M. Arias, Growth of HgCdTe by molecular-beam epitaxy, in *Properties of Narrow Gap Cadmium-based Compounds*, Edit by P. Capper, INSPEC, London, United Kingdom, 1994, Chapter A1.4, Page 30

<sup>20</sup> S. Sivananthan, X. Chu, J. Reno and J. P. Faurie, *J. Appl. Phys.*, 60, 1359 (1986)

<sup>21</sup> V. S. Varavin, S. A. Dvoretzky, V. I. Liberman, N. N. Mikhailov and Y. G. Sidorov, *Thin Solid Films*, 267, 121 (1995)

<sup>22</sup> T. Aoki, D. J. Smith, Y. Chang, J. Zhao, G. Badano, C. Grein and S. Sivananthan, *Appl. Phys. Lett.* 82, 2275 (2003)

Te atomic layers is larger than in normal HgCdTe (111) monolayers so the HgCdTe lattice surrounding the Te lattice applies compressive stress. The size of Te precipitates observed in our sample is typically 10 to 30 nm in length and a few monolayers in thickness. The size of precipitates observed in MBE HgCdTe by TEM is normally small, less than 50 nm in diameter. Large Te precipitates (up to 100 nm) are only reported in low temperature MBE-grown CdTe<sup>23</sup>. This is due to the different binding energy between Cd-Te and Hg-Te, so that the CdTe lattice can tolerate larger Te precipitates than HgTe. When Te precipitates are large enough that they cannot be tolerated by the HgCdTe lattice, the bonds will be broken, especially Hg-Te, and low-energy small-index surfaces, especially (111) planes, are exposed because of desorption, so that crater voids appear and continually grow upwards. Hence Te<sub>2</sub> molecules can trigger the formation of crater void defects and act as an origin of crater defects on HgCdTe surfaces. It has also been reported that the crater void defects on some HgCdTe layers may be associated with the contamination of deionized water, however, they normally display special shapes and can be removed or controlled by optimizing the treatment procedures before MBE growth. Therefore, they are not discussed here in detail.

In conclusion, the observation of many crater defects on a particular sample means that either the growth conditions have changed from the optimized values to the "Te-rich" side, which leads to poor compositional homogeneity, or there is some problem with the pretreatment procedures. Note that some samples with substantial numbers of surface crater defects are found to have low etch pit density values and result in devices fabricated on materials with defects having good device performance. However, the homogeneity is poor. The density of surface crater defects can be controlled by adjusting the growth conditions and tightly controlling the pretreatment procedures. Since Te<sub>2</sub> dissociation plays an important role in defect formation, promoting Te<sub>2</sub> dissociation, e.g. using a Te cracker cell, will be helpful. Photoassisted<sup>24,25</sup> MBE growth has been reported to increase Te desorption and might be helpful to enhance the Te<sub>2</sub> dissociation in a way that decreases the possibility of crater formation.

The crater defects as well as their formation mechanisms are discussed in detail in our publications.<sup>25,26,27</sup>

#### *b) Microtwins*

Twinning is also a common source of defects in MBE-grown HgCdTe under lower surface temperature or higher Hg flux. The formation mechanism of microtwins can be explained using the TLK model<sup>28</sup>. Under optimal growth conditions the temperature is high enough that the diffusion length is approximately the terrace width but not greater than the desorption temperature. Under these conditions, incoming atoms on the surface will sublime at the highest entropy lattice position. In an ideal crystal this will be a kink. If a kink is not within the surface diffusion length, a step edge will act as a nucleation point. This allows for a step flow growth mode (van-der Merwe mode). In the presence of threading, glide, vacancy or adatom defects the nucleation can occur on the step terrace which then forces the growth to either coalesce forming either grain boundaries or laminar twins. Similarly, if the surface temperature is too low or the

<sup>23</sup> N. G. Chew, A. G. Cullis, and G. M. Williams, Appl. Phys. Lett. 45 1090 (1984)

<sup>24</sup> T. H. Myers, K. A. Harris, R. W. Yanka, L. M. Mohnkern, R. J. Williams, and G. K. Dudoff, J. Vac. Sci. Technol. B 10, 1438 (1992)

<sup>25</sup> K. A. Harris, T. H. Myers, R. W. Yanka, L. M. Mohnkern, R. W. Green, and N. Otsuka, J. Vac. Sci. Technol. A 8, 1013(1990)

<sup>26</sup> T. Aoki, D.J. Smith, Y. Chang, J. Zhao, G. Badano, C. Grein, and S. Sivananthan, Appl. Phys. Lett., 82,2275(2003)

<sup>27</sup> T. Aoki, Y. Chang, G. Badano, J. Zhao, C. Grein, S. Sivananthan, and David J. Smith, J. Electron. Mater., 32, 703(2003)

<sup>28</sup> J. Venables, Introduction to Surface and Thin Film Processes, Cambridge University Press, 2000

Hg flux is too high, i.e. at the upper-right side of Fig. 7, then the diffusion length of the adatoms is insufficient to assure nucleation at an edge or kink site. Of course, if the substrate is too rough, even higher temperatures or lower Hg fluxes are required to sustain a normal MBE growth, which causes a narrowing down of the optimized growth window. When a columnar twin emerges at the surface, it produces hillocks, as is shown in Fig.9. Twins are also known as microdefects because their typical size rarely exceeds  $2\mu\text{m}$ . Zandian *et al.* reported that the density of microdefects is a function of the II-VI flux ratio and is inversely proportional to the growth temperature.<sup>29</sup> Even under optimized growth conditions, voids and microdefects still can be discovered simultaneously on the sample surface. However, the total density of voids and microdefects on the surface should be only of the order of  $10^2\text{ cm}^{-2}$  if the substrates are properly treated to decrease the density of Te precipitates on the surface<sup>30</sup>.

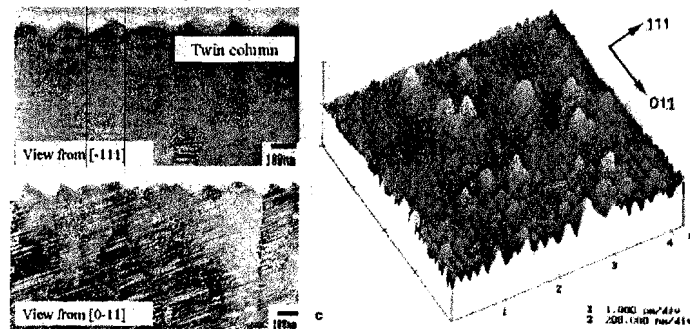


Fig.9. SEM and TEM photos showing that surface hillocks are usually due to the formation of adjacent columns of twins. Size:  $0.1-0.2\mu\text{m}$ <sup>31</sup>

### c) Needle defects

HgCdTe epilayers grown on CdZnTe substrates characterized by a high SE roughness parameter were characterized by a high density of needle defects (Fig.10), which appear on most samples regardless of growth conditions. An excellent correlation was found between the needle defect density and the CdZnTe SE roughness. As is shown in Fig.11, in general, layers grown on substrates for which the SE roughness was  $<10\text{\AA}$  had very low densities of needle defects or no such defects at all. Rougher substrates resulted in proportionally higher densities of needle defects. The interpolation lines on the plot are meant to show this trend.

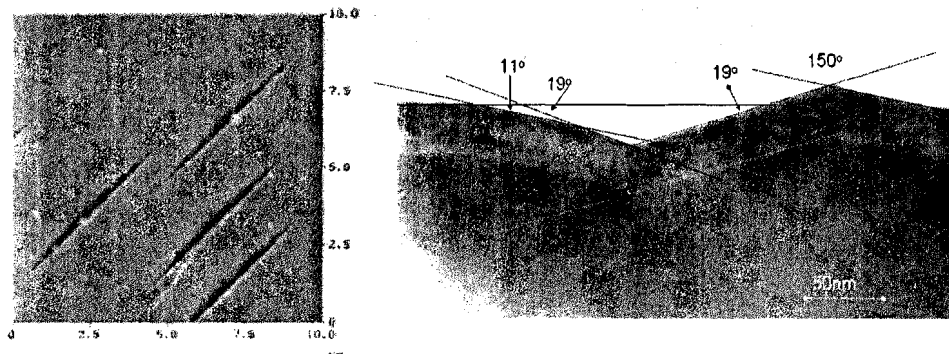


Fig. 10. The AFM (left) and TEM (right) photograph of a needle defect

<sup>29</sup> M. Zandian and E. Goo, J. Electron. Mater., 30, 623(2001)

<sup>30</sup> E. C. Piquette, M. Zandian, D. D. Edwall and J. M. Arias, J. Electron. Mater., 30, 627(2001)

<sup>31</sup> L. Zhao, J. S. Speck, R. Rajavel, J. Jensen, D. Leonard, T. Strand and W. Hamilton, J. Electron. Mater., 29, 732(2000)

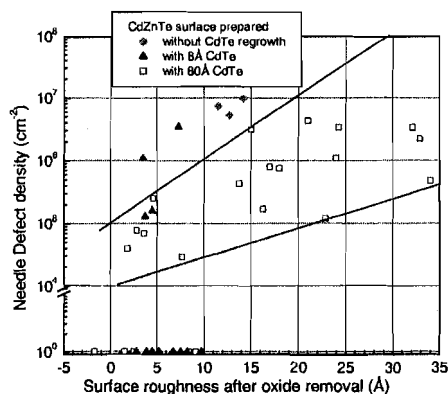


Fig.11. Plot of the HgCdTe needle defect density versus the CdZnTe surface roughness as measured by in-situ ellipsometry.

We found that Te annealing and CdTe growth on the CdZnTe substrates smoothed out the surface and substantially lowered the density of needle defects. A comparison of the samples with only 8 Å of CdTe or without CdTe interfacial layers (the rhombs and the triangles in Fig.11), with those samples with 80Å CdTe layers (the squares) showed the latter to have much lower needle defect densities. An 80 Å CdTe layer grown before the nucleation of HgCdTe helps to smooth out the CdZnTe substrate, hence lower the needle defect density. Additionally, a variety of other interfacial layers was also introduced to reduce the defect density and improve the overall quality of the epilayer, even in the presence of less than perfect substrates.

In summary, the perfection of the substrate surface and of its crystalline structure both are essential for the growth of high-quality material. Suppression of the CdZnTe substrate-induced defects in HgCdTe epilayers may require the use of appropriate interfacial layers or the growth of CdZnTe “smoothing” buffer layers on the CdZnTe substrates. Our detailed discussion of needle defect is given in Ref.32.

#### d ) Other defects

Tellurium precipitates and cross-hatches are other defects found on the MCT surface. Tellurium precipitates consist of crystalline clusters of Te, which are identified as such by their lattice constant and by a stoichiometric analysis (using for example EDX). Very often Te precipitates are found in MCT layers by cross-sectional TEM and SEM. Arias et al.<sup>33</sup> concluded that Te precipitates appear together with void defects under a constant Hg flux when the growth temperature is approximately 10°C above the upper end of the optimized growth temperature region. They have been previously reported on the MCT surface by only one author.<sup>34</sup> The cross-hatch pattern shown in Fig. 12 is characteristic of this type of problematic defect. It appears when the crystalline quality of MCT is very good, after defect decoration etching or even before etching.. It has been reported that the density of cross-hatch defects correlates with the etch pit density of MBE epilayers.<sup>35</sup>

<sup>32</sup> J. Zhao, Y. Chang, G. Badano, S. Sivananthan, J. Markunas, S. Lewis, J. H. Dinan, P. S. Wijewarnasuria, Y. Chen, G. Brill and N. Dhar, J. Electron. Mater., 33, 881(2004)

<sup>33</sup> J. M. Arias, Growth of HgCdTe by molecular-beam epitaxy, in Properties of Narrow Gap Cadmium-based Compounds, Edit by P. Capper, INSPEC, London, United Kingdom, 1994, Chapter A1.4, Page 30

<sup>34</sup> P.S. Wijewarnasuriya, M. Zandian, D. B. Young, J. Waldrop, D. D. Edwall, W. V. Mclevice, D. Lee, J. Arias and A. I. D'souza, J. Electron. Mater., 28, 649(1999)

<sup>35</sup> M. Martinka, L. A. Almeida, J. D. Benson and J. H. Dinan, J. Electron. Mater., 30, 632(2001)

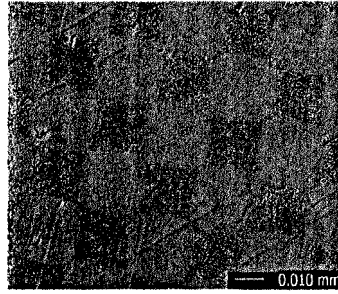


Fig. 12. Nomarski micrograph of defect etched MBE-grown HgCdTe epilayers showing crosshatches

We try to explain the formation mechanism of such phenomena. Assuming CdZnTe and HgCdTe to relax with  $\mathbf{a}/2 \langle 011 \rangle$  Burger's vectors which prefer to propagate on the  $\{111\}$  family of glide planes ( $\mathbf{g}$ ), Fig 13 illustrates the possible dislocation lines, i.e. the  $\{111\}$  planes intersecting the  $(211)$  surface ( $\mathbf{n}$ ) at  $u = \mathbf{n} \times \mathbf{g}$  resulting in the set  $\{u\} = \{[0\bar{1}\bar{1}], [\bar{2}13], [0\bar{1}\bar{1}], [2\bar{3}\bar{1}]\}$

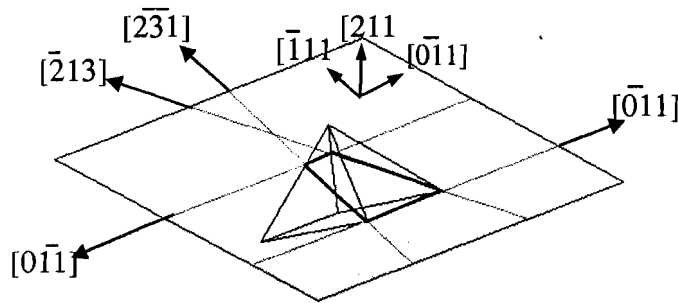


Fig 13.  $\{111\}$  family of planes intersecting  $(211)$  surface to form dislocation lines  $u$

Misfit dislocations from the small but sufficient lattice mismatch and later from the thermal mismatch allow threading dislocations to propagate on the  $\{111\}$  glide planes and close their dislocation loop at the surface along the  $\mathbf{u}$  directions. It has been observed that  $[\bar{2}13]$  and  $[2\bar{3}\bar{1}]$  dislocation lines are prominent at high growth temperatures with lower EPD counts while  $[0\bar{1}\bar{1}]$  and  $[0\bar{1}\bar{1}]$  lines are exhibited at low temperatures with higher EPDs.<sup>35</sup> This implies a greater in-plane biaxial strain at higher temperatures, presumably from the thermal mismatch, since the  $\langle 011 \rangle$  exhibits no shear. This may getter dislocations to these planes. Low temperature deposition would exhibit a lower thermal mismatch and thus have a more balanced shear between the planes. Dislocations will then prefer planes with the greatest biaxial strain. This will be determined by the angle the plane makes with the normal, i.e. the greater the angle the less the biaxial strain. The  $[\bar{1}\bar{1}\bar{1}]$  plane has the greatest angle to the surface, indicating this plane has the smallest biaxial strain, however the  $[111]$  plane is at the shallowest angle and thus exhibits the greatest biaxial strain and thus is the most probable glide plane.

### Optimization of interfacial layers

To improve reproducibility and growth yield as well as the quality of the material grown, we researched and developed superlattice (SL) interfacial layers for the MBE growth of HgCdTe.<sup>36</sup> A schematic of a SL-based interfacial layer is shown on the left side of Fig. 14(a), and a corresponding bright-field diffraction contrast electron micrograph is shown in the right. A darker contrast in the micrograph corresponds to a higher Hg concentration. After annealing, the SL layers interdiffuse to form an SWIR HgCdTe layer having a Cd composition of about 0.5; this layer offers a transparent window for backside-illuminated infrared light, as illustrated in Fig. 14(b), which is essential for the fabrication of most infrared detector arrays.

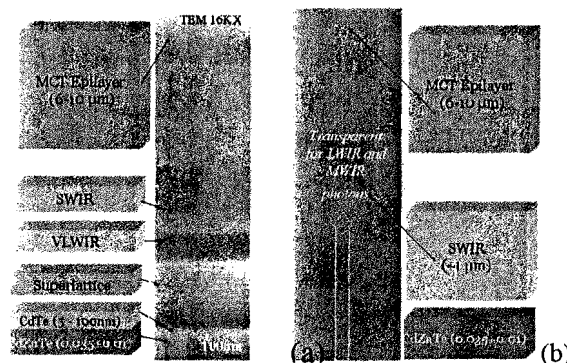


Fig. 14 Schematic of the interfacial layer structure (left) and corresponding cross-sectional transmission electron micrograph (right) of sample (a) as grown, and (b) after a 24hour anneal at 250°C under a Hg saturated atmosphere.

Cross-sectional electron micrographs were taken to document the effects of the SL interfacial layers on defects arising from the substrate. Fig. 15 shows that the substrate surface roughness can be smoothed out after the growth of several periods of a HgTe/CdTe SL. The SL roughly reproduces the shape of pits only over 5 to 6 periods. After that, the pits are smoothed out. The smoothing of pits occurs primarily during the growth of HgTe layers. As shown in Fig. 15, the Hg-rich region inside the pit is of relatively large thickness, indicating a higher HgTe growth rate inside the pit than outside. Fig. 16 (a) and (b) show threading dislocations that were bent or possibly terminated at a HgTe-CdTe interface within a SL. Since HgTe has a smaller lattice constant ( $0.6461\text{nm}^{37}$ ) than CdTe ( $0.6483\text{nm}^{38}$ ), and also considering that Hg-Te bonds are weaker than Cd-Te ones, stress relaxation is more likely to occur in CdTe layers, while defects will tend to form in HgTe layers.

<sup>36</sup> Y. Chang, J. Zhao, H. Abad, C. H. Grein, S. Sivananthan, T. Aoki, D. J. Smith, Applied Physics Letters, 86, (131924)2005

<sup>37</sup> A. Tanaka, Y. Masa, S. Seto, T. Kawasaki, J. Crystal Growth, 94, 166(1989)

<sup>38</sup> W. Jua, D. A. Gulino and R. Higgins, J. Crystal Growth, 263, 30(2004)

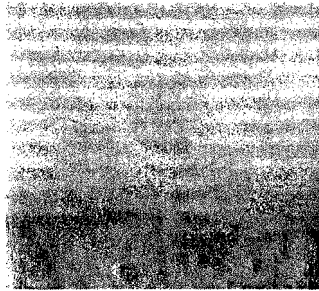


Fig. 15. Cross-sectional electron micrograph showing that microscopic surface roughness smoothed out after several periods of HgTe/CdTe superlattice growth.

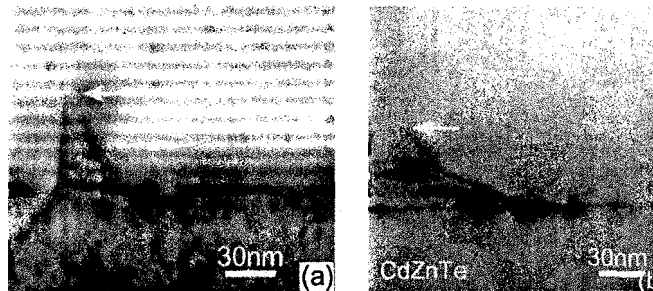


Fig. 16 (a) and (b): cross-sectional electron micrograph showing a threading dislocation that terminated or bent (as indicated by white arrows) at an HgTe-CdTe interface within the superlattice.

Substantial experimental and theoretical efforts have been directed towards reducing the densities of threading dislocations in epitaxially grown semiconductor materials, especially III-V materials grown for laser diode fabrication. Previous work on threading dislocation reduction in mismatched layers showed that the threading dislocation density in laterally uniform layers is reduced only through reactions between threading dislocations. Relative motion between dislocations is necessary to bring them within a reaction distance. Because different threading dislocations have different line directions, one possible source is trajectory motion of the threading dislocations with changing film thickness.<sup>39,40</sup> Most important, motion may be induced by the intentional growth of a strained layer<sup>41,42</sup> in which the generation of misfit dislocations accompanies the glide motion of threading dislocations when the film exceeds a critical thickness. Unlike III-V systems, which have large lattice mismatches, the II-VI HgTe/CdTe system has only a very small lattice mismatch (0.32%), which is normally considered insufficient to induce the motion of threading dislocations. However, our TEM observations of MBE grown HgCdTe suggest the partial or complete glide of threading dislocation along interfaces. Similar results also have been observed by Carmody *et al.*<sup>43,44</sup>, who found that the bending of threading dislocations can reach 25  $\mu\text{m}$ . Such bending forces 3-dimensional dislocations to move/glide in a 2-dimensional interfacial plane, which offers a much higher chance that the dislocations merge

<sup>39</sup> P. Sheldon, K. M. Jones, M. M. Al-Jassim, and B. G. Yacobi, *J. Appl. Phys.*, 63, 5609(1988)

<sup>40</sup> M. Tachikawa and M. Yamaguchi, *Appl. Phys. Lett.*, 56, 484(1990)

<sup>41</sup> R. Hull, J. C. Bean, R. E. Lenbenguth, and D. J. Werder, *J. Appl. Phys.*, 65, 4723(1989)

<sup>42</sup> H. Nishino, I. Sugiyama, and Y. Nishijima, *J. Appl. Phys.*, 80, 3238(1996)

<sup>43</sup> M. Carmody, D. Lee, M. Zandian, J. Phillips and J. Arias, Threading and Misfit Dislocation Motion in MBE Grown HgCdTe Epi-layers, presentation on 2002 U.S. Workshop for Physics and Chemistry of II-VI materials, San Diego, CA, USA, Nov 13, 2002

<sup>44</sup> M. Carmody, D. Lee, M. Zandian, J. Phillips and J. Arias, *J. Electron. Mater.*, 32, 701(2003)

together along an interface even if the dislocations are not completely free to glide, which in turn greatly reduces the possibility of dislocations propagating within the active HgCdTe layers, and leads to enhanced material properties.

However, we found that if the substrate surface damage is too great, the SL interfacial layers may not be able to fully cover all substrate defects, as shown in Fig. 17, although certain scales of improvement have been found. The x-ray topograph and rocking curve data shown in Fig. 18 confirm this conclusion.



Fig. 17. cross-sectional electron micrograph showing SL interfacial layer help partly block the defective substrate; however, certain amount of defects (indicated using black arrows) still are observed beyond the interfacial layers.

In a former MURI presentation and report, we presented characterization data for a typical MBE HgCdTe sample grown on a CdZnTe (211)B substrate with SL interfacial layers. For samples with average EPD values of  $1 \times 10^5 \text{ cm}^{-2}$  using Schaake's etchant<sup>45</sup> and n-type doping levels of about  $1.3 \times 10^{15} \text{ cm}^{-3}$ , reasonably good Auger-1 plus radiative limited carrier lifetimes and mobilities were reproducibly obtained as long as the substrate surface roughness was in a tolerable range.

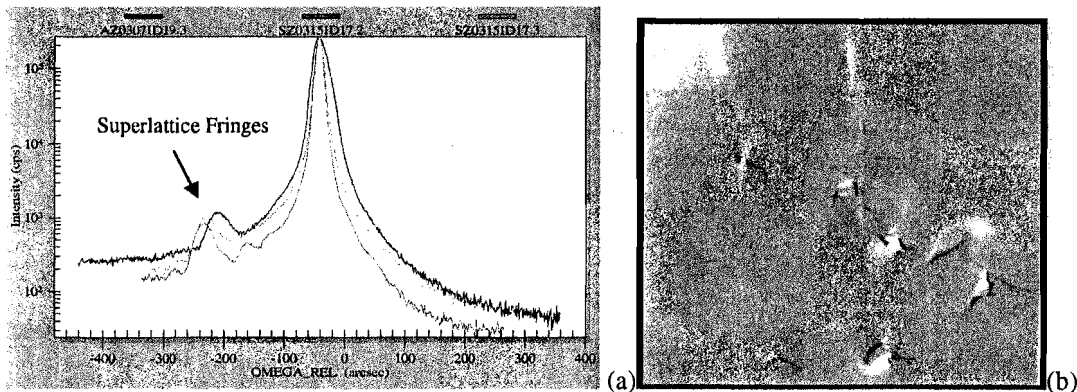


Fig. 18. (a) X-ray 224 reflection Rocking Curves of MBE-grown HgCdTe on CdZnTe substrate with interfacial layers. The fringes from the superlattice can be seen in samples SZ0315ID17.2(red) and SZ0315ID173(green), indicating better growth quality of the interfacial layers. The sample grown on AZ0307ID13.9(blue) with bad crystalline quality shown at (b) can not show clear superlattice fringes. (Measured by Dr. Justin Markunas, Dr. Shannon Lewis and Dr. J. H. Dinan, U.S. Army RDECOM CERDEC Night Vision & Electronic Sensors Directorate)

<sup>45</sup> H.F. Schaake, J. H. Tregilgas, A. J. Lewis, P.M. Everett, J. Vac. Sci. Technol, A1, 1625(1983)

The employment of SL interfacial layers during HgCdTe MBE growth on CdTe/Si, CdZnTe/Si and CdSeTe/Si substrates resulted in the enhancement of reproducibility. We are still exploring the optimum design of SL interfacial layers for Si-based substrates.

*Study of the nucleation and growing surface of HgCdTe using RHEED and spectroscopic ellipsometry*

We have conducted extensive investigations to understand the growth modes and the interaction with steps during the kinetics of HgCdTe growth with the aid of RHEED and SE, which are both very versatile techniques for growth and surface studies. We describe here the RHEED and SE observations of HgCdTe heteroepitaxial growth on CdTe/CdZnTe substrates as a function of growth temperature under constant Hg fluxes. This has led to valuable insights into the kinetics of growth and recovery in HgCdTe MBE. In this study, the variations in the RHEED intensity of a specular spot during the initial growth and later recovery were recorded. The intensity was found first to increase due to initial island formation and later to decrease to an intensity close to the initial value. After HgCdTe growth paused, a recovery was observed under Hg flux. Attention was paid to both the initial increase and the recovery after growth.

The intensity observed during the growth can be described by an empirical fit, which has a negative term which exponentially decays with time constant  $\tau_1$ , and a positive term that decays with a longer time constant  $\tau_2$ .  $I(t) = I_0 + A(1 - \exp(-t/\tau_1)) - B(1 - \exp(-t/\tau_2))$ . A, B,  $\tau_1$ ,  $\tau_2$ , and  $I_0$  are fitting parameters with  $\tau_2 > \tau_1$ .

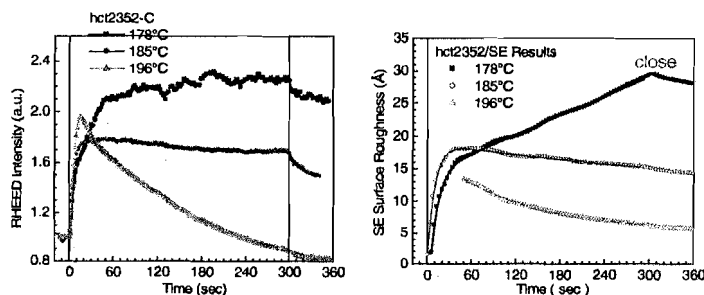


Fig.19. In situ RHEED intensity (left) and SE surface roughness (right) evolution under various growth temperatures (layer hct2352): 192C, 185C and 178C. The solid lines are empirical fits.

As shown in Fig.19, different qualitative behaviors of the intensity evolution are observed in three cases. At 178°C, the intensity reaches a maximum with a long time constant ( $\tau_1=23.5$  sec) and levels off after that. At a higher temperature (185°C and 192°C), the RHEED intensity reaches a peak in a shorter time and then decays slowly to a lower final value with continuous growth. The final RHEED intensity at 192°C is clearly much lower than that at lower temperatures. Upon the cessation of growth, recovery occurs under the Hg flux. A clear exponential decay is observed at 185°C; while at higher temperatures (192°C) or lower temperatures (178°C), the recovery is slower and non-exponential. The SE surface roughness parameter shows a similar behavior.

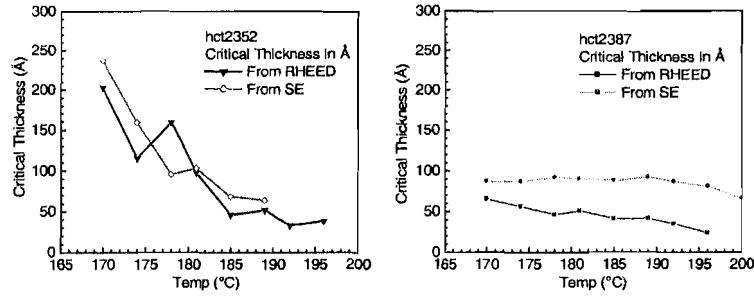


Fig.20. Temperature dependence of the critical thickness during the initial stages of growth. The left figure shows the results from layer hct2352. The right figure gives results from layer hct238, which had a lower growth rate. In the plots, the black dots are from RHEED and the red dots are from SE.

To make the results from different samples comparable, we plot the critical thickness for the initial stages of growth, which is basically a product of growth rate and the time constant  $\tau_1$ . The critical thickness is plotted in Fig.20. The critical thickness of layer hct2387 shows a weaker temperature dependence than layer hct2352. They have similar critical thickness values in a higher temperature range ( $>185^\circ\text{C}$ ), while layer hct2352 has higher critical thickness values in a lower temperature range ( $<185^\circ\text{C}$ ). The difference in the temporal behavior can be described using a dimensionless ratio  $\alpha (=Jh^2/Dn_0)$ . This is the ratio of the input adatom flux  $J$  times the square of the terrace width  $h$  to the diffusion constant  $D$  times  $n_0$ , the concentration of lattice sites for island formation. In terms of the above theoretical predications, the numerical results plotted in Fig.19 and Fig.20 can be explained as follows:

- (a) At a high temperature (small  $\alpha$ ), the rate of clustering is low and growth proceeds predominantly by the incorporation of mobile adatoms into step edges. Because most nucleation occurs at step edges, the activation energies for nucleation and coarsening effects are a mechanical energies rather than free energies. They are temperature insensitive, as shown by the experimental results.
- (b) At a lower temperature (large  $\alpha$ ), the island concentration builds up until at a time equivalent to the deposition of one monolayer the islands are incorporated into the step edge and form a less densely populated fresh terrace (Stranski-Krastanov growth). The build-up of islands is then repeated, but to a lesser extent, until a steady-state island concentration is reached when the nucleation rate is balanced by the capture of islands due to convection.
- (c) At a very low temperature (very large  $\alpha$ ), thermal diffusion is so low and hence the number of islands on the terrace is so large that the surface rapidly reaches a time independent high roughness (3-D growth). Because of the low adatom migration on the surface, no coarsening process was observed at these temperatures.

A remarkable fact regarding the HgCdTe system is that, over a relatively small temperature range, 3-D growth turns into terraced hillock growth (modified S-K-M) and further into a step-flow growth. This may be explained by the above-mentioned assumptions. The model also explains that, as the input flux or the substrate roughness increases, step flow growth would require a higher substrate temperature (lower  $\alpha$ ) due to a higher level of nucleation.

The discrepancies between experiment and theory also are obvious. Especially significant is that the experimental timescales needed for achieving a stable state of nucleation and coarsening are much larger than the theoretical results, which are shorter than the time needed for one monolayer growth. The reason could be associated with the experimental fact that the steps on the CdTe (or CdZnTe) (211) surface are often multi-atomic layer steps. During the initial nucleation stage, this provides a higher possibility for nucleation at the step edges or on the terrace surfaces, thus a higher island density. Hence it will take a longer time to reach a stable state for island formation and growth at a fixed incident flux.

## In situ characterization

### Study of Hg absorbed on CdTe surface

We analyzed the optical spectra of Hg adsorbed on CdTe surfaces over the energy range of 1.6-4.5 eV for a variety of temperatures and Hg fluxes. In our analysis of the change in the pseudo-dielectric function due to Hg deposition, we made two major approximations. First, we treated chemisorbed and physisorbed Hg as separate layers, which is strictly speaking not true, because the various Hg forms are probably mixed. Second, we used the 3D form of the  $\text{Hg}_{1-x}\text{Cd}_x\text{Te}$   $\epsilon(\omega;x)$  dielectric function to mimic the effect of chemisorbed Hg on the surface. Also, we used a Drude function to model the presence of physisorbed Hg, which probably is a good approximation. We fit only the imaginary part of the dielectric function,  $\langle \epsilon_2(\omega) \rangle$ , because it has a more direct physical interpretation and, unlike the real part, does not depend on the presence of out-of-range critical points. In addition, the limited resolution of the M88 ellipsometer prevented us from using a critical point analysis to interpret the data. These limitations notwithstanding, our analysis gives surprisingly good results, in that it reproduces the expected dependence of the thickness of the chemisorbed and physisorbed components correctly as a function of temperature and pressure and gives reasonable values for the composition of the  $\text{Hg}_{1-x}\text{Cd}_x\text{Te}$  (see Fig. 21 and Fig.22).

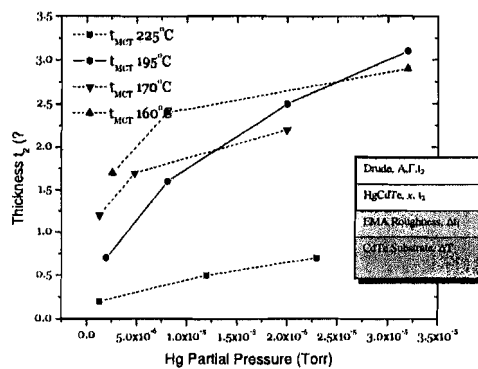


Fig. 21. Calculated thickness  $t_2$  of the chemisorbed Hg layer obtained using  $\epsilon_{1\infty} = 12$ , as a function of the Hg flux for different substrate temperatures. The uncertainty in each thickness obtained from the correlation matrix is approximately  $\pm 0.8 \text{ \AA}$ . The values for the Hg partial pressure are uncorrected  $\text{N}_2$  pressure readings. The data at 195°C (continuous line) were acquired during a separate run from the data taken at 225, 160 and 170°C (dashed lines). In the 195°C run, the sample was exposed to Te flux down to a lower temperature, thus it was likely to have a higher Te coverage. The inset shows a sketch of the model used for the data analysis. For each layer, the adjustable parameters are shown

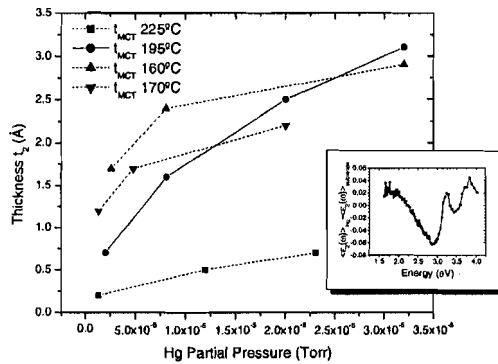


Fig.22. Calculated thickness  $t_2$  of the chemisorbed Hg layer obtained using  $\epsilon_{\infty} = 30$ , as a function of the Hg flux for different substrate temperatures. The inset shows a typical difference spectrum.

Although we do not at present believe the absolute numbers provided by the analysis, we believe that this approach confirms our general ideas regarding the nature of the CdTe(211) surface under a Hg flux, and is valuable at least technologically to obtain a reliable run-to-run characterization of the surface before growth. More detailed discussions can be found in our related publications.<sup>46,47</sup>

*Establish new CdZnTe library with improved precision*

*In situ* SE composition and temperature measurements require libraries of experimentally obtained dielectric functions. In our *in situ* approach, the dielectric function library of CdZnTe is used to determine the temperature, composition and surface roughness of CdZnTe before the growth of HgCdTe. Then, the composition of HgCdTe and surface roughness are determined during growth using a HgCdTe library. We have built dielectric function libraries to determine both the temperature and the composition of CdZnTe and HgCdTe simultaneously using the derivatives of the *in situ* measured dielectric functions. For CdZnTe, the critical points  $E_0$ ,  $E_0+\Delta_0$ ,  $E_1$  and  $E_1+\Delta_1$  lie in the visible and near IR spectrum and hence can be measured accurately with a commercially available ellipsometer. For HgCdTe,  $E_1$  and the existing libraries of the dielectric function will be used to determine the composition and possibly the temperature.

Since all *in situ* SE measurements are based on the experimentally collected dielectric function library, the measuring accuracy and precision largely depends on these libraries. To improve the library and therefore our SE *in situ* monitoring and control, we designed and performed experiments to obtain spectrally extended CdZnTe data sets for  $\epsilon(\omega;x,T)$  to supplement the current CdTe dielectric function library available from the Army Night Vision and Electronic Sensors Directorate (NVESD). The properties of the new data sets are summarized in Table 2.

Table 2. General properties of the new CdZnTe data sets

MPL CdZnTe Library	Range	Increments
Temperature Range	50 – 350°C	25°C
Spectral Range	0.7 – 5.0 eV	15 Å in the range 1.2 to 5 eV and 30 Å from 0.7 to 1.2 eV
Composition Range	0 to 13% Zn	0, 4.15, 12.65%, 100% Zn

<sup>46</sup> G. Badano, Y. Chang, J. W. Garland and S. Sivananthan, J. Electron. Mater., 33, 583(2004)

<sup>47</sup>G. Badano, Y. Chang, J. W. Garland, and S. Sivananthan, Appl. Phys. Lett., 83, 2324(2003)

The newly measured CdZnTe data sets extended the existing CdTe library to a library for the CdZnTe alloy system by providing extra sets of temperature dependent data for 4.5%, 12.65% and 100% Zn compositions. They also have a significantly higher resolution in energy, and extend the spectral range at both the low and high ends to a range from 0.7 to 5.0 eV (compared to the existing library range of 1.8 to 4.3 eV). We also used In as well as Sn to calibrate the actual surface temperature. The new CdZnTe dielectric function library based on these data sets dramatically improved the fitting certainty and measuring precision of composition and temperature, which enable us to achieve better control over the MBE growth of HgCdTe.

To form a high precision library, a critical point (CP) model of the dielectric function has been used to simultaneously obtain the temperature and composition of the CZT substrate. By employing derivatives of the dielectric function, we can dramatically reduce the effects of surfaces overlayers to which ellipsometry is sensitive. Technically, the CP model and the second derivative fits were used as a compromise to simplify the analysis of data in real time while keeping an acceptable high level of accuracy. An example of the fitting is shown in Fig.23. Because  $E_1 + \Delta_1$  lies at the upper end of the spectrum, where reduced levels of light increase the noise level, and where CPs become very broad, we use this CP only as a weak reference. A HgCdTe library was also been established using a similar approach.

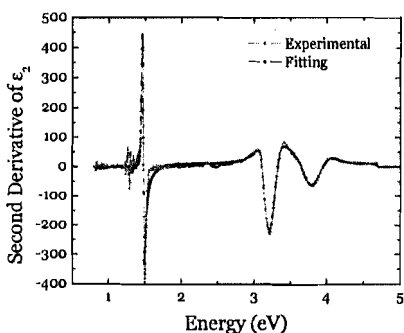


Fig.23. The second derivative fits of a  $y=0.04$   $\text{Cd}_{1-y}\text{Zn}_y\text{Te}$  at  $75^\circ$  incidence. It was used as a compromise to simplify the analysis of data in real time while keeping an acceptable level of accuracy.

The obtained CP  $E_0$  and  $E_1$  energy positions are shown in Fig.24 as a function of actual surface temperature  $T$  as well as Zn composition. The availability of data on the behavior of two or more critical points as a function of temperature and composition allows, in principle<sup>48</sup>, the analytic or numerical inversion of this information to yield the temperature and composition as independent functions of the critical point energies. The procedure followed for CdZnTe consists of determining the critical point energies  $E_0$ , and  $E_1$  for the three (0.0, 4.5, and 12.5%) available Zn compositions and then fitting the results for each critical point to a surface function that depends linearly on composition and temperature. Linear fits proved adequate for the available narrow range of Zn concentrations.<sup>49</sup> In the second step, the fitted function pairs  $E_0 = E_0(x, T)$

<sup>48</sup> The functional dependence of the critical points on  $x$  and  $T$  must be "sufficiently" independent to allow the conversion.

<sup>49</sup> The improvement by using quadratic surface fits for the  $E_0$ ,  $E_1$  sets of data was insignificant.

and  $E_I = E_I(x, T)$  were simply inverted to yield  $T = T(E_0, E_I)$  and  $x = x(E_0, E_I)$ . The inverted T and x equations applicable to the thermal environment of the MPL chamber and normalized using In and Sb dots are as follows:

$$x(E_0, E_I) = 54.0951 + 198.3806 E_0 - 104.63956 E_I$$

$$T(E_0, E_I) = 4015.4701 - 118.9503 E_0 - 1127.5475 E_I$$

Here, the composition x is given in percent, T in degrees Kelvin and the energies in eV.

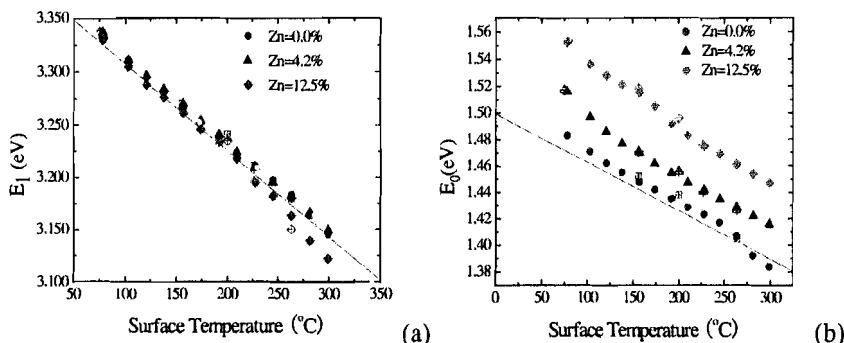


Fig.24. CdZnTe  $E_I$  and  $E_0$  critical points as functions of surface temperature and Zn composition

The differences between the values of x and T predicted by these equations and the actual measured data are shown in Fig. 25. We find that the derived equations for x and T can predict the composition to an rms accuracy of  $\pm 0.5\%$  and the temperature to an accuracy of  $\pm 5^\circ$  near the optimized MBE growth window. These are the first measurements of T with an accuracy sufficient to place T within the accepted window for the growth of HgCdTe

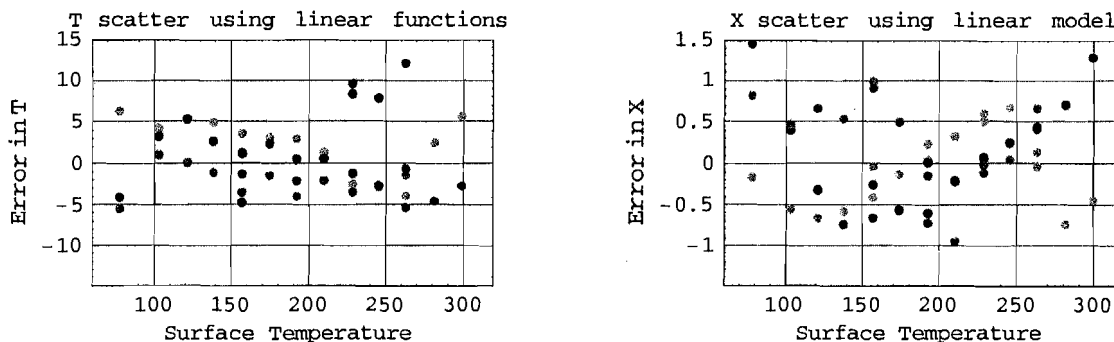


Fig. 25. Scatter in x and T using the inverted equation for temperature as a function of the critical point energies  $E_0$  and  $E_I$ . Green : CdTe, Blue: CZT (4.2%) and Red: CZT 12.5%.

*Characterize the quality of 2-dimensional MBE growth using the surface roughness and depolarization coefficient parameters*

Ideal MBE growth should be 2D. 3D growth is mostly associated with the generation of defects. SE gives us an *in situ* method to monitor any degeneration of growth. The SE surface

roughness (SR) parameter measured using an effective medium approximation (EMA) model has already been used to monitor the growth. We have found that increases in the EMA SR are always associated with the degeneration of material quality, mostly associated with the formation of twins. Due to the nature of the EMA model, it is sensitive to roughness on an atomic-scale, both parallel to and normal to the growth surface, and can give information about how small scale defects form. In addition, we find that the substrate submicroscopic roughness as measured by ellipsometry correlates well with the qualitative roughness from RHEED. The ellipsometry roughness is a good predictor of the final quality of the MCT layers. We have correlated the presence of several HgCdTe defects with the substrate roughness.

We found that Rotating Analyzer Ellipsometry (RAE) is very sensitive to depolarization effects. For rough samples, the measured dielectric function departs significantly from the true dielectric function because the effective medium approximation employed is not suitable for describing larger scale roughness lower in spatial frequency. Based on the analysis of characteristics of RAE, we introduced a model for the interpretation of SE data containing a depolarization coefficient parameter.

The depolarization coefficient parameter ( $u$ ) for RAE is defined by the following equations:

$$\begin{aligned}\cos 2\psi &= (1 + u) \cos 2\psi' \\ \cos \Delta &= \cos \Delta' \left( 1 + \frac{1}{\sin^2 \psi'} u \right)\end{aligned}$$

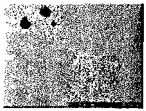
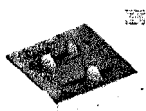
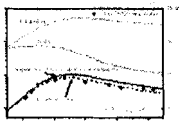
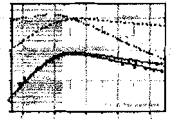
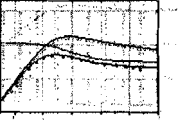
where  $\Psi'$  and  $\Delta'$  are measured by SE, and  $\Psi$  and  $\Delta$  are corrected results taking depolarization effects into account. When the depolarization coefficient parameter  $u=0$ ,  $\Psi' = \Psi$  and  $\Delta' = \Delta$ , which means there is no polarization at all. The depolarization coefficient parameter of RAE measures surface roughness on a larger scale than the EMA SR parameter.

We discovered correlations between *in situ* characterization data and recombination lifetime data. Results show that there indeed are correlations between the minority carrier recombination lifetime and an average depolarization coefficient  $u$  measured by *in situ* spectrometric ellipsometry. The actual depolarization coefficient is strongly wavelength-dependent. As an approximation in the fitting calculations, we treated  $u$  as a constant for all wavelengths. Because this approximation is not very accurate, it is not clear how well the approximate measured depolarization coefficient corresponds to the actual depolarization coefficient  $u(\lambda)$  at any given wavelength. However, the value of the average  $u$  is a measure of the actual depolarization effect caused by surface roughness on a scale of approximately the wavelength, i.e. hundreds nanometers to a few micrometers. It correlates well enough with the lifetime data to be regarded as a useful predictor during growth. Typical results showing the correlation between  $u$  measured *in situ*, the surface morphology, the EPD and the relative importance of SRH processes are shown in Table 3. This knowledge can be developed as a technique capable of acting as an *in situ* early alarm of the degeneration of material quality, so that one will have a chance to optimize the MBE growth conditions to stop the degeneration of layer quality, and hence improve the material growth yield.

For much larger defects, which may make the fitting of SE data impossible, modulated off-axis light scattering will be helpful. We set up mathematical models to study the interaction

between the incident light and the MBE growth surface with different patterns that simulate various kinds of surface defects to develop a portable technique to properly predict carrier recombination lifetimes when a sample is undergoing growth.

Table 3. Correlation between in situ data and recombination lifetimes

Sample#	HCT2036	HCT2140	HCT2138	HCT2139
Surface Morphology				
Depolarization u (x1E4)	-5, -5, ±5	-5.5, ±4	-5.18, ±4	-5, 25, ±4
EMA t (Å)	0, 2	0, 2.5	0, 5	0, 5
Temperature Dependent Lifetime				
$\tau_{SRH}/\tau \sim 100\%$ at 77K	24.1%	36.7%	56.2%	70.1%
EPD (cm <sup>2</sup> ) (Schaake's solution)	$2.0 \times 10^5$	$9.1 \times 10^5$	$2.7 \times 10^6$	$4.9 \times 10^6$

### Ex situ electrical characterization of MBE HgCdTe to improve the MBE growth

#### Verification of equipment calibration

In order to establish portable techniques for the fully controllable and optimized MBE growth of HgCdTe, it is important to calibrate, normalize and optimize characterization measurements since we need to exchange experimental results and obtained knowledge with other industrial and academic institutions (including DoD research laboratories) involved in this effort. Dr. Dinan of NVSED coordinated an exchange of samples with industrial and academic institutions. Samples were received from Rockwell Scientific and DRS Technologies for lifetime measurements and were found to be of excellent quality. We performed the measurements under the suggested conditions. The agreement was reasonably good, as is shown in Table 4. The observed minor discrepancies may be due to the fitting, to temperature offsets and/or to the bias. The EPD measurements were also calibrated with the help of Dr. Almeida of NVSED. We worked with Dr. P.S. Wijewarnasuriya from ARL on lifetime fittings and sent a graduate student to work with him at ARL. We also calibrated our Hall effect measurement system using measured samples from DRS Technologies and from ARL. We now use the same recipe for the etching solution, the same design of tools and the same etching procedure. This is helpful for exchanging experimental data, results and knowledge with collaborators.

Table 4. Comparison of lifetime measurements by Rockwell Scientific and us (UIC)

Composition	78K		202K	
	From Rockwell	From UIC	From Rockwell	From UIC (200K)
0.32	7.1μs	7.3μs	14.5μs	15.0μs
0.32	7.5μs	8.4μs	16.7μs	15.4μs
0.32	8.4μs	7.0μs	14.0μs	12.6μs

### Carrier recombination in HgCdTe

Carrier recombination processes in HgCdTe directly contribute to both photon detection and noise generation mechanisms in photovoltaic infrared devices fabricated from the HgCdTe, and hence are important to the device figures of merit, including detectivities  $D^*$  and zero-bias dynamic-resistance-area-products  $R_0A$ . Auger, radiative and Shockley-Read-Hall (SRH) are three commonly recognized recombination mechanisms. These processes in HgCdTe are characterized by recombination lifetimes that are usually measured by fitting photoconductive decay data. Since the three mechanisms show different temperature dependencies, the measurement of temperature-dependent lifetimes and related fitting calculations are therefore helpful to separate the contributions from each mechanism and offer an approach to study the recombination processes in HgCdTe. Of the three mechanisms, two – Auger and radiative recombination – are intrinsic, and are consequently determined by intrinsic material properties, such as composition and doping levels that can be precisely measured by other techniques e.g. Hall effect and infrared absorption mapping<sup>50</sup>. The calculation of lifetimes determined by intrinsic Auger and radiative recombination mechanisms in this work used sets of semi-empirical formulas developed by Beattie, Landsberg and Blakemore<sup>51,52</sup> (BLB) based on Kane's  $k \cdot p$  model with several key parameters determined experimentally.<sup>53</sup> In addition, we also conducted accurate Auger recombination calculations that test the BLB form. These intrinsic mechanisms establish theoretical upper limits on the lifetime. The differences between the calculated and measured lifetime values are attributed to SRH recombination, which arises from impurities or defects in HgCdTe and can be fit within the theoretical framework given by Shockley, Read and Hall. Thus, to improve the material lifetimes, characterizing SRH centers and trying to increase SRH lifetimes become the ultimate goal for HgCdTe growers.

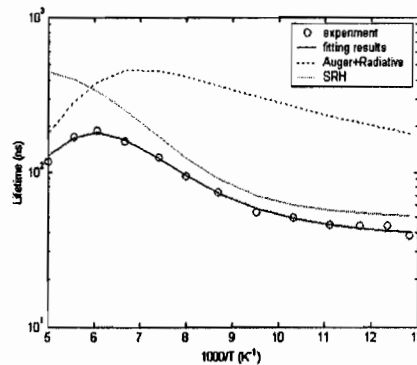


Fig. 26. Temperature-dependent carrier lifetime data and fitting results for a MBE as-grown HgCdTe sample with composition of 0.22 and n-type doping level of  $2.6 \times 10^{15} \text{ cm}^{-3}$

Table 5. Fitting parameters for data in Fig. 26.

	$E_t/E_g$	$\tau_{n0}$ ( $\mu\text{s}$ )	$\tau_{p0}$ ( $\mu\text{s}$ )
Value:	0.6380	0.1611	0.0503
Uncertainty:	0.1779	0.6258	0.0432

<sup>50</sup> Y. Chang, G. Badano, E. Jiang, J.W. Garland, J. Zhao, C. H. Grein and S. Sivanathan, J. Crystal Growth, 277, 78(2005)

<sup>51</sup> A.R. Beattie and P.T.Landsberg, Proc. R. Soc. London A 249,16(1959)

<sup>52</sup> J. S. Blakemore, Semicond. Stat., Pergamon Press, New York, 1962, Chap. 6

<sup>53</sup> See, for example, V.C. Lopes, A.J. Syllaios and M.C. Chen, Semicond. Sci. Technol., 8, 824(1993) and the references cited therein

The lifetime fitting procedure and models were carefully characterized and improved to clearly identify the SRH lifetimes. The Levenberg-Marquardt method, which combines the advantages of the steepest decent method and Newton's method, was employed to automatically fit the temperature dependent lifetime data so as to precisely extract information regarding SRH carrier recombination processes. The Hessian matrices of the model were used to analyze the fitting certainties. Table 5 shows the certainty of the fitting parameters used in the calculation of the lifetime data in Fig. 26. Reasonable certainty can be obtained for those samples that are dominated by the SRH recombination mechanism. However, of course the certainty in the SRH parameters degenerates if the measured lifetime approaches the theoretical limits determined by the Auger ( BLB with  $|F_1F_2|=0.22$  ) and radiative mechanisms, as shown in Fig.27 and Table 6; under such conditions, the obtained SRH lifetimes are totally determined by experimental noise and are not reliable. We found that the fitting parameters can be trapped in local minima that are strongly correlated with starting values. Therefore, the Monte Carlo and simulated annealing methods were employed to help the program converge to the global minimum. Additionally, low temperature points were weighted more heavily in order to obtain more precise SRH energy levels. Constraints were used to ensure that the fitting calculations gave only physically reasonable results.

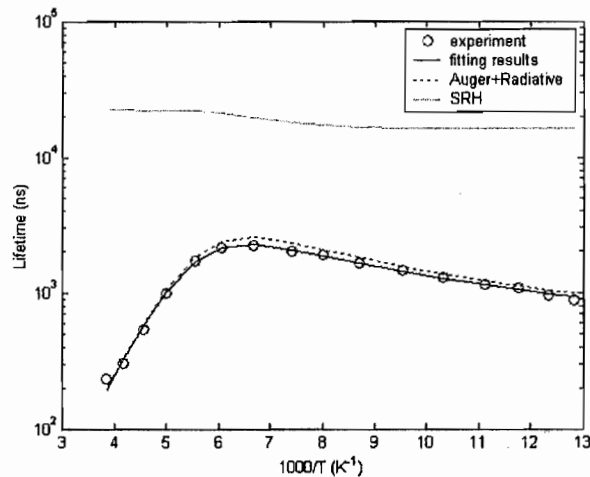


Fig.27 Temperature-dependent carrier lifetime data and fitting results for an annealed (250°C 24 hours) MBE HgCdTe sample with a composition of 0.24 and n-type doping level of  $1.3 \times 10^{15} \text{ cm}^{-3}$

Table 6. Fitting parameters for data in Fig.27.

	$E_v/E_g$	$\tau_{n0}$ ( $\mu\text{s}$ )	$\tau_{p0}$ ( $\mu\text{s}$ )
Value:	0.6297	4.680	16.296
Uncertainty:	24.644	854.357	304.45

Although the p-type Auger-7 lifetime has long been subject to controversy, the n-type band-to-band Auger-1 lifetime was deemed to be well established until recently.<sup>54, 55</sup> We conducted calculations to reevaluate the band-to-band Auger-1 lifetime in n-type LWIR HgCdTe because the Auger-1 lifetime can be measured in long-wavelength-infrared (LWIR) HgCdTe.

Our calculations of the electronic band structure are based on a fourteen-band bulk basis, including spin-orbit splitting. The need to rely on a 14-band basis rather than the more common 8-band basis arises because of the sensitivity of the optical and electronic properties to the electronic structure in regions of the band structure away from the band edge. Errors inherent in the 8-band model become significantly more pronounced as the states one is interested in become farther from the band edge. The optical absorption is then calculated from this highly structured and nonparabolic band structure using the concurrently derived momentum matrix elements. The full band structure and absorption spectrum can be calculated on a common desktop workstation in about 20 minutes. Typical agreement with measured absorption spectra for superlattices with more complicated band structures is within 10–50%.<sup>56</sup>

Auger recombination rate calculations, which are computationally more intensive, require additional approximations and are thus characteristically less accurate than the optical properties. Despite these approximations, we have demonstrated agreement within better than a factor of two between theoretically and experimentally determined Auger rates for a wide variety of MWIR and LWIR superlattices and bulk materials.<sup>57,58</sup> The computational methodology is fully described in ref. <sup>59</sup>. Briefly, the band structures and momentum matrix elements computed employing the 14 band  $\mathbf{k}\cdot\mathbf{p}$  formalism are used directly as input for the computation of Auger lifetimes. They are input into the Auger rate computations in the form of look-up tables with a mesh spacing of  $0.002 \text{ \AA}^{-1}$ . The transition matrix elements are evaluated using a statically screened Coulomb interaction and first order  $\mathbf{k}\cdot\mathbf{p}$  for the wave function overlaps. The Auger recombination process involves two carriers in initial and final states. Thus one starts with twelve nested integrations over momentum variables. Conservation of momentum and energy reduces that to eight; however, such a multiple integral is still intractable to direct integration. We have developed efficient Monte-Carlo routines to integrate the Auger recombination rates, including electron-electron (Auger-1) scattering and hole-hole (Auger-7) scattering. The first dominates in n-type HgCdTe. The calculated result for a  $\text{Hg}_{0.77}\text{Cd}_{0.23}\text{Te}$  sample with an In doping level of  $N_d=1\times 10^{15} \text{ cm}^{-3}$  is shown in Fig. 28. The calculated results show reasonable agreement with BLB's Auger-1 formula<sup>51,52</sup> by adjusting the overlap integral of the Bloch functions  $|F_1F_2|$  to 0.16 from 0.22 (which we typically use). This value is inside the range of 0.1 to 0.3 employed by various authors.<sup>53</sup>

<sup>54</sup> S. Krishnamurthy, M.A. Berding, Z.G. Yu, C.H. Swartz, T.H. Myers, D.D. Edwall and R. DeWames, J. Electron. Mater., 34, 873(2005)

<sup>55</sup> S. Krishnamurthy, A. Sher, A. -B. Chen, J. Appl. Phys., 82, 5540 (1997)

<sup>56</sup> S.W. McCahon, S.A. Anson, D.-J. Jang, Michael E. Flatté, Thomas F. Boggess, D.H. Chow, T.C. Hasenberg, and C.H. Grein, Appl. Phys. Lett. 68, 2135 (1996).

<sup>57</sup> Michael E. Flatté, C.H. Grein, T.C. Hasenberg, S.A. Anson, D.-J. Jang, J.T. Olesberg, and Thomas F. Boggess, Phys. Rev. B 59, 5745 (1999).

<sup>58</sup> D.-J. Jang, J.T. Olesberg, Michael E. Flatté, C.H. Grein, T.C. Hasenberg, and Thomas F. Boggess, Phys. Rev. B. 58,13047 (1998).

<sup>59</sup> C.H. Grein, P.M. Young, M.E. Flatté, and H. Ehrenreich, J. Appl. Phys. 78, 7143 (1995).

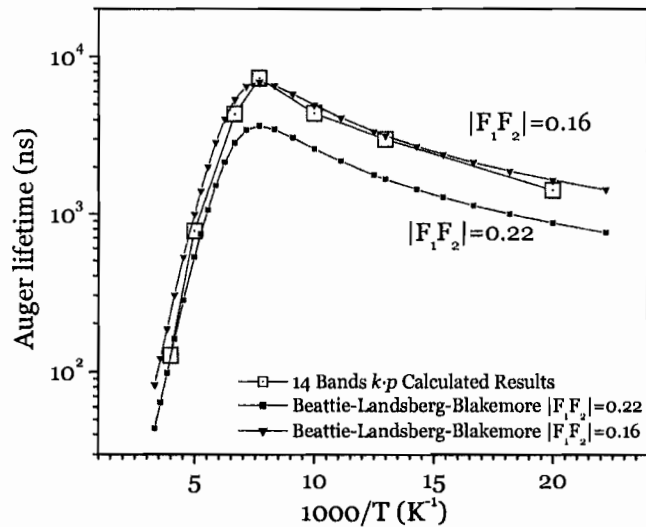


Fig. 28. Computed minority carrier Auger-1 recombination lifetimes of  $\text{Hg}_{0.77}\text{Cd}_{0.23}\text{Te}$  doped to  $N_d=1 \times 10^{15} \text{ cm}^{-3}$  as a function of inverse temperature using the 14-band calculation method and compared with Beattie-Landsberg-Blakemore's formulas with two choices for the value of the overlap integral ( $|F_1F_2|$ ).

The statistics of the lifetimes measured at 200K and 77K for all of our samples over the past two years is shown in Fig. 29. The lifetimes measured on the annealed samples were higher than those measured on the as-grown samples. This is much more obvious for the 77K lifetimes than for the 200K lifetimes because the SRH processes are relatively more important at 77K than at 200K. The lifetimes were obviously enhanced by annealing. Fig. 30 shows the statistics of the energy levels of the dominant SRH centers in MBE  $\text{HgCdTe}$  measured by temperature dependent carrier lifetime. From these results, we deduced the following conclusions:

- 1) The SRH centers in as-grown samples mostly lie between  $0.75 E_g$  (Hg vacancy or  $V_{\text{Hg}}$ ) and  $0.5 E_g$ , with only a small fraction at  $0.25 E_g$ . The  $0.75 E_g$  SRH center, due to  $V_{\text{Hg}}$  defects, is dominant in as-grown samples even if the dislocation density is very high.
- 2) After  $250^\circ\text{C}$  annealing for 24 hours, the fit values for the dominant SRH centers were scattered in energy; in some samples there were shallow centers above  $0.8 E_g$  or below  $0.1 E_g$ .
- 3) A probable reason for the scattered distribution in energy is that the uncertainty in its determination becomes very large as the lifetime approaches the theoretical limit after annealing.
- 4) The carrier recombination processes in many of the annealed samples are statistically dominated by mid-band-gap centers, especially for those samples with high dislocation densities, which is in good agreement with the results<sup>60</sup> obtained by deep level transient spectroscopy (DLTS) at the former Texas Instruments.

<sup>60</sup> M. C. Chen and R. A. Schiebel, J. Appl. Phys., 71(10), 5269(1992)

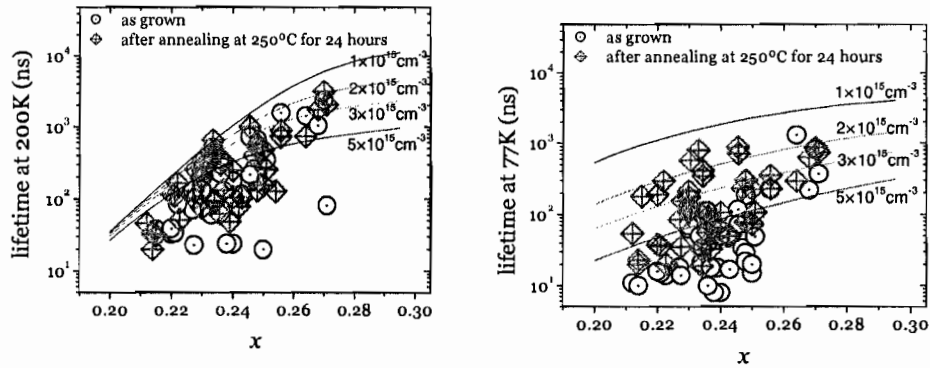


Fig. 29. 200K (left) and 77K (right) lifetimes of MBE HgCdTe samples before and after annealing in a Hg saturated atmosphere. The solid lines show the theoretical limitations on the lifetime at corresponding doping levels and temperatures.

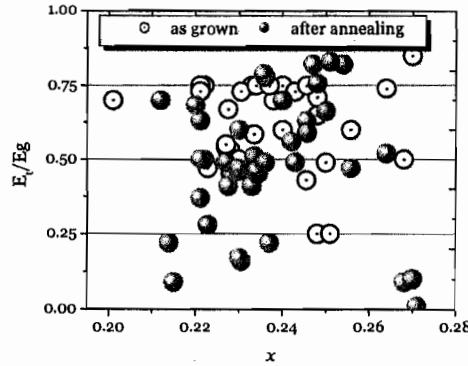


Fig. 30 The statistics of the energy position of SRH centers in as grown and annealed MBE HgCdTe measured by the temperature dependent carrier lifetimes vs. composition.

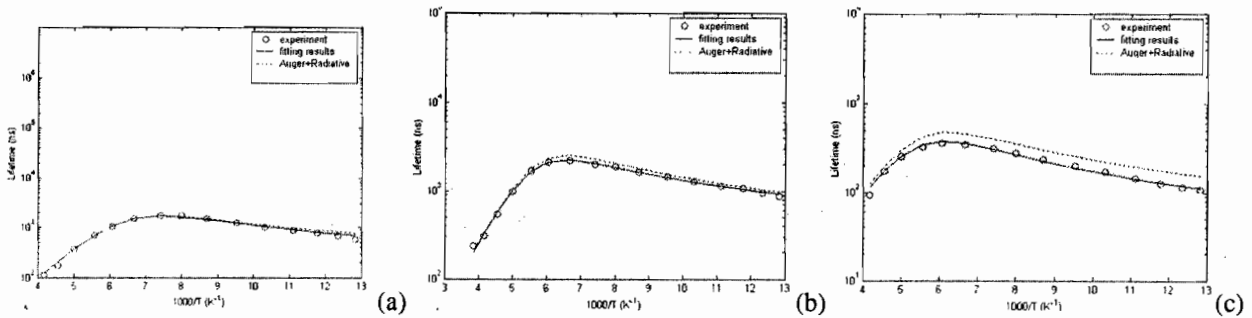


Fig.31. Photoconductive decay lifetime measurement and fitting results of high quality MBE-grown HgCdTe samples (for composition and doping level details see Table 7) whose lifetimes approached theoretical limits.

Based on the above reevaluated lifetime formulas and algorithms, carrier recombination lifetime measurements and fittings are being used as a routine characterization technique at MPL/UIC. They were employed to help improve the material quality by optimizing growth conditions<sup>61</sup>, substrate preparation and post-growth thermal processing procedures. High quality

<sup>61</sup> Y. Chang, G. Badano, J. Zhao, C. H. Grein, S. Sivananthan, T. Aoki, and David. J. Smith. Appl. Phys. Lett.. 83, 4785(2003)

HgCdTe materials with lifetimes approaching the theoretical limits have been obtained<sup>62</sup> with the aid of this effort, as shown in Fig.31.

Table 7. Compositions, n-type doping levels and etch pit densities of long-wavelength infrared HgCdTe samples grown by MBE on CdZnTe substrates shown in Fig.31.

Sample#	Cd Composition	Doping level ( $10^{15}\text{cm}^{-3}$ )	Etch pit density ( $\text{cm}^{-2}$ )
(a)	0.23	1.3	$3.7 \times 10^4$
(b)	0.24	1.3	$1.0 \times 10^5$
(c)	0.23	3.2	$1.6 \times 10^5$

### Ex situ optical characterization of MBE grown HgCdTe

The goal of our MURI research work is to perform fundamental studies to establish portable MBE growth techniques for controlling carrier lifetimes. Because most optical characterization techniques just use light as a probe, they are non-destructive and therefore quite valuable. Through our optical studies, we established certain nondestructive portable characterization techniques to reduce the average cost by improving yield.

#### *Infrared microscope mapping measurements of HgCdTe*

Mapping measurements were performed on a Thermo Nicolet Centaurus infrared microscope connected to a Thermo Nicolet 870 Fourier transform infrared spectrometer. Each wafer was scanned using a computerized x-y translation stage with a position precision of  $\pm 1\mu\text{m}$ . The infrared beam size can be varied with an adjustable aperture down to  $25\mu\text{m}$  at a  $10\mu\text{m}$  wavelength. The aperture was set to  $100\mu\text{m}$  to get strong signals and shorten the measurement time for the large area mapping measurements. A liquid-nitrogen-cooled long wavelength infrared HgCdTe detector, KBr beam splitter and Ever-Glo<sup>TM</sup> infrared source were used in the experiment. The data was processed after the transmission mapping measurements were finished.

The interference matrix method was used for calculations<sup>63</sup>. The contributions from both *s* and *p* polarizations should be considered in evaluating the total transmissivity and reflectivity. The influence of the substrate should also be considered and can be calculated by Monte Carlo analysis, i.e. by averaging 100 transmissivity values calculated from the 100 randomly generated phase values. HgCdTe layers grown on CdZnTe, CdTe, CdSeTe, GaAs and Si substrates all can be calculated using this method as long as the corresponding optical constants are correctly input, which offers much flexibility. A fit to the Fourier transformed spectral data was initially performed to obtain first guess values of the HgCdTe and CdTe thicknesses. These values were then introduced into the calculation for fitting the untransformed data. The Levenberg-Marquardt<sup>64</sup> algorithm was used for automatic fitting and a simulated annealing method<sup>65</sup> was introduced to ensure that the fitting calculation reached the global mean square error (MSE) minimum rather than being trapped by other local minima. The band gap of a layer typically is

<sup>62</sup> Y. Chang, J. Zhao, H. Abad, C. H. Grein, S. Sivananthan, T. Aoki and D.J. Smith, Appl. Phys. Lett., 86, 31924(2005)

<sup>63</sup>See, for example, H. A. Macleod, Thin-film Optical Filters, American Elsevier Publishing Company, Inc., New York, 1969, Chapter 2

<sup>64</sup>W. H. Press, S. A. Teukolsky, W. T. Vetterling and B. P. Flannery, Numerical Recipes in C, Cambridge University Press (1995) Page 683

<sup>65</sup>W. H. Press, S. A. Teukolsky, W. T. Vetterling and B. P. Flannery, Numerical Recipes in C, Cambridge University Press (1995), Page 444

defined to be the energy at which the transmission  $T_r$  corresponds to an absorption coefficient of  $\alpha=1000\text{cm}^{-1}$  or  $500\text{cm}^{-1}$ , although other definitions also can be employed<sup>66,67,68</sup>. The absorption coefficient of  $\alpha=1000\text{cm}^{-1}$  was chosen to determine the energy gap for all data reported in this work. The point was calculated using the expression  $T_r=T_{rmax}\cdot\exp(-\alpha d)$ , where  $T_{rmax}$  is the average maximum transmission and  $d$  is the layer thickness. The composition of the layer was determined at each point from the relationship between  $x$  and the band gap  $E_g$  given by Hansen *et al*<sup>69</sup>.

Since the fit values of the composition  $x$  and HgCdTe layer thickness  $d$  depend upon one another self-consistent fitting calculations were used to determine  $x$  and  $d$  simultaneously. After  $x$  and  $d$  converged to a given precision, e.g. a change in  $x<0.0001$  and a change in  $d<0.01\text{ }\mu\text{m}$  in one iteration, the self-consistent fitting calculation was stopped, giving reasonably precise values for the composition and thickness. Typical results obtained are shown in Fig. 32 for MBE-grown HgCdTe on 20mm $\times$ 20mm CdZnTe substrates and Fig. 33 for MBE-grown HgCdTe on 3-inch Si based substrates with CdTe buffer layers. Experimental details are discussed in our related publication.<sup>70</sup> We also performed mapping measurements on CdZnTe substrates, for which we can measure the Zn composition distribution using the recipes given by Johnson *et al*.<sup>71</sup> Typical CdZnTe substrate mapping results are shown in Fig. 34, for which the average Zn composition is 0.0344 with the standard deviation of 0.0018.

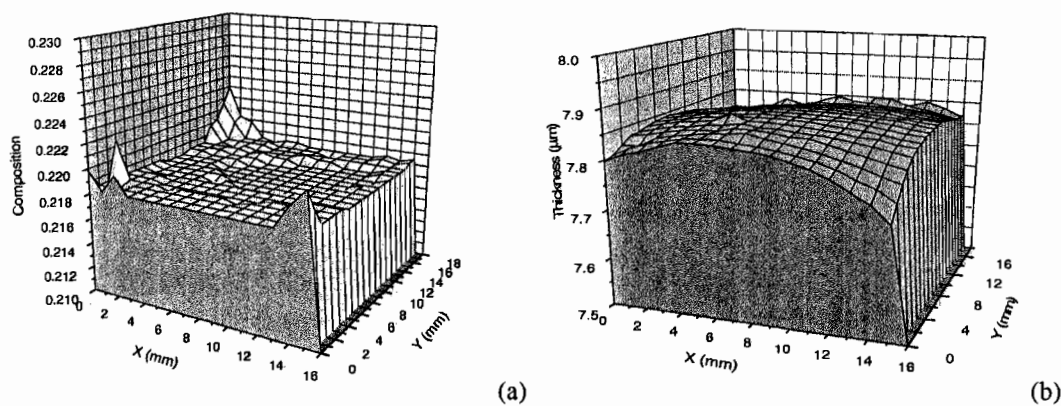


Fig. 32. Mapping results for a HgCdTe sample grown by MBE on a CdZnTe substrate. (a) composition, and (b) HgCdTe thickness.

<sup>66</sup>V. Ariel, V. Garber, G. Bahir, A. Raizman, and A. Sher, Appl. Phys. Lett., 70, 1849 (1997)

<sup>67</sup>J. H. Chu, B. Li, K. Liu, and D. Y. Tang, J. Appl. Phys. 75, 1234 (1994)

<sup>68</sup>K. Liu, J. H. Chu, B. Li, and D. Y. Tang, Appl. Phys. Lett., 64, 2818(1994)

<sup>69</sup>G. L. Hansen, J. L. Schmit and T. N. Casselman, J. Appl. Phys., 53, 7099(1982)

<sup>70</sup>Y. Chang, G. Badano, E. Jiang, J. W. Garland, J. Zhao, C. H. Grein and, S. Sivananthan, J. Cryst Growth, 277, 78(2005)

<sup>71</sup>S. M. Johnson, S. Sen, W. H. Konkel and M. H. Kalisher, J. Vac Sci. Tech. B9, 1897(1991)

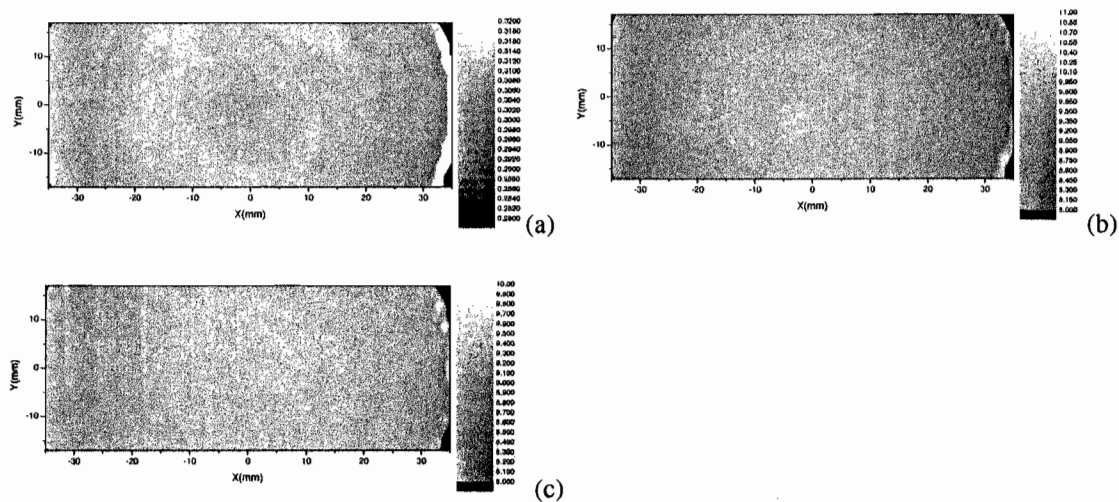


Fig. 33. Mapping results for a HgCdTe sample grown on a CdTe/Si substrate by MBE. (a) composition, (b) HgCdTe thickness, and (c) CdTe thickness.

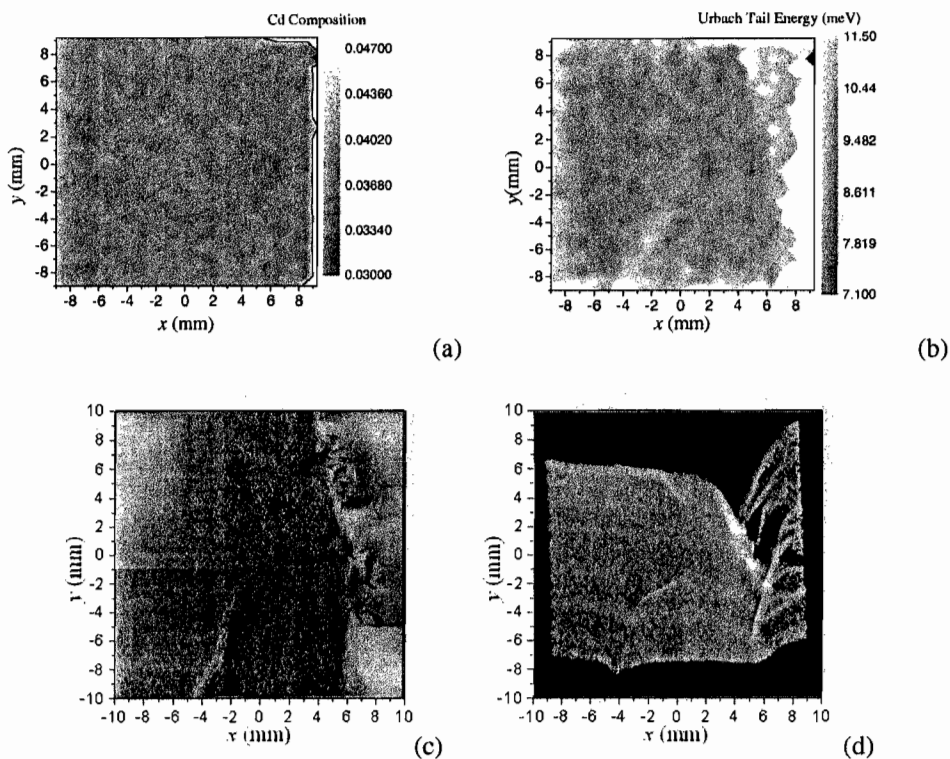


Fig. 34. Composition (a), Urbach tail energy (b) mapping of a CdZnTe substrate. (c) and (d) are x-ray topograph measurement results. (c) reflection topograph and (d) transmission topograph

The Urbach tail energy, which is dominated by contributions from electron-phonon interactions, alloy disorder and structural disorder, was found to be capable of characterizing material quality.<sup>72</sup> We also performed Urbach tail energy mapping measurements for HgCdTe. Fig. 35(a)-(e) shows HgCdTe Urbach tail mapping results (c) together with thickness (a), Cd composition (b), x-ray reflection topograph (d) and transmission topograph results (e). Correlations were found between the Urbach tail energy distributions and the topograph maps.

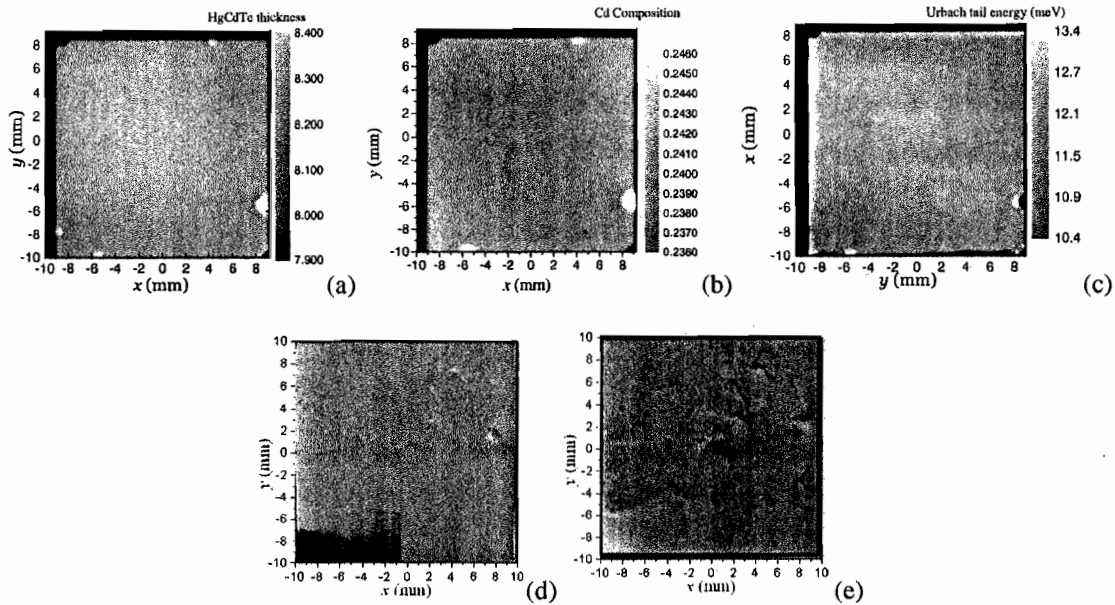


Fig. 35 Infrared microscopic mapping measurement results of an MBE-grown LWIR HgCdTe epilayer. (a) thickness, (b) composition, (c) Urbach tail energy. For comparison, we also show x-ray reflection (d) and transmission (e) results here.

### Macroscopic and microscopic uniformity of HgCdTe

MBE grown HgCdTe has become more uniform in terms of both composition and thicknesses. To obtain both spatial composition and thickness uniformities with reasonably good resolution, as we discussed at the last section, a computerized automatic uniformity mapping method was set up at MPL/UIC. The experimental and modeling methods were discussed in detail in the last section.<sup>70</sup>

Typical mapping results for a 3-inch HgCdTe sample grown on a CdTe/Si substrate are given in Ref. 70. Typical uniformity data for such samples are given in Table 8. Note that excellent composition and thickness uniformities were found in the central 20×20 mm<sup>2</sup> area.

Table 8. Typical composition and thickness uniformity data of 3-inch MBE-grown HgCdTe

	Composition	Standard deviation	Thickness (μm)	Standard deviation (μm)
Total 3-inch area:	0.2340	±0.0042	7.15	±0.07
Central 20×20mm area:	0.2299	±0.0008	7.21	±0.01

<sup>72</sup> Y. Chang, G. Badano, J. Zhao, Y. D. Zhou, R. Ashokan, C. H. Grein and V. Nathan, J. Electron. Mater., 33, 709(2004)

Considering the high thermal conductivity of Si and the relatively large area of the epilayer grown, the non-uniformity can be attributed to a non-uniformly distributed flux. Mapping measurement results for a HgCdTe sample grown on a (211)B CdZnTe substrate, however, show differences from epilayers grown on Si substrates. The average composition  $x$  is 0.2182 with a standard deviation  $\Delta x$  of 0.0006. Higher composition material is found in about  $2 \times 2 \text{ mm}^2$  areas near the corners. The HgCdTe layer was also found to be thicker in the center, being especially thin in the corners (where the composition is higher). The growth temperature in the corners is expected to be a bit high due to the relatively low thermal conductivity of CdZnTe. As a result, the radiative thermal energy absorbed by HgCdTe on the CdZnTe near a corner cannot be easily transferred out, as confirmed by finite element analyses. The slightly higher temperature leads to a decrease in the Hg sticking coefficient,<sup>73</sup> which induces a higher Cd composition and thinner material in the corners than that in the center, according to MBE growth thermodynamic kinetic analysis<sup>74,75</sup>. Under certain conditions, a non-uniformly distributed flux could in principle also result in such patterns; however, according to the mapping results obtained from large area HgCdTe samples grown on Si wafers up to 3 inches in diameter in the same MBE chamber, as shown in Table 8, the very good composition and thickness uniformities in the  $20 \times 20 \text{ mm}^2$  area of the wafer center clearly excludes that possibility. Hence the nonuniformity in the substrate temperature distribution must have stemmed almost solely from the substrate geometry. The conclusion that higher growth temperatures are present in the corners can also be deduced from the differences observed between surface defects in the center and those in the corners of some of our samples, e.g. the size and density of crater defects, which are closely related to the growth temperature.<sup>76</sup> The average thickness of the sample is  $7.84 \text{ }\mu\text{m}$  with a standard deviation  $\Delta d$  of  $0.03 \text{ }\mu\text{m}$ . The nonuniformity in composition and thickness exists primarily only in small areas near the sample corners.

In addition to the macroscopic uniformity of MBE-grown HgCdTe wafers, microscopic uniformity has also attracted attention since it is suspected of causing nonuniformities in the performance figures of merit (e.g. quantum efficiencies, dark currents, detectivities) of infrared focal plane detector arrays.<sup>77</sup> MBE-grown long-wavelength-infrared HgCdTe materials were also investigated using infrared microscope mapping. A  $20 \text{ }\mu\text{m} \times 20 \text{ }\mu\text{m}$  focused infrared beam was employed to study the microscopic uniformity of MBE-grown HgCdTe over  $200 \text{ }\mu\text{m} \times 200 \text{ }\mu\text{m}$  areas, in comparison with the  $100 \text{ }\mu\text{m}$  diameter beam used for macroscopic uniformity measurements. The integration times or scanning times were found to be of great importance to obtaining reliable measurements because the beam signal is relatively weak in comparison with that in typical spectroscopic measurements. The measured standard deviation becomes stable when the scan number increases above 32, at which point the standard deviation is only determined by the material itself. As shown in Fig.36, a best relative compositional uniformity of  $< 0.0001$  over a  $200 \text{ }\mu\text{m} \times 200 \text{ }\mu\text{m}$  area was obtained. The standard deviation of the relative thickness of the MBE layer is less than  $0.002 \text{ }\mu\text{m}$  over the corresponding area. Again, a larger microscopic deviation in both composition and thickness can only be found near the edges or corners of the MBE-grown HgCdTe wafers, corresponding to the macroscopic non-uniformities

<sup>73</sup> S. Sivananthan, X. Chu, J. Reno, and J. P. Faurie, *J. Appl. Phys.* 60, 1359 (1986)

<sup>74</sup> J. P. Gailliard, *Revue. Phys. Appl.*, 22, 457(1987)

<sup>75</sup> T. Colin and T. Skauli, *J. Electron. Mater.*, 26, 688(1997)

<sup>76</sup> Y. Chang, G. Badano, J. Zhao, C.H. Grein, S. Sivananthan, T. Aoki, and D.J. Smith, *Appl. Phys. Lett.*, 83, 4785(2003)

<sup>77</sup> J. D. Phillips, et al., *Appl. Phys. Lett.*, 83, 3701(2003)

caused by the edge effects of the MBE heating plate. In contrast, the standard deviation of the Urbach tail energy over this area is as high as 0.36meV, which is non-uniformly distributed, as shown in Fig.36(c).

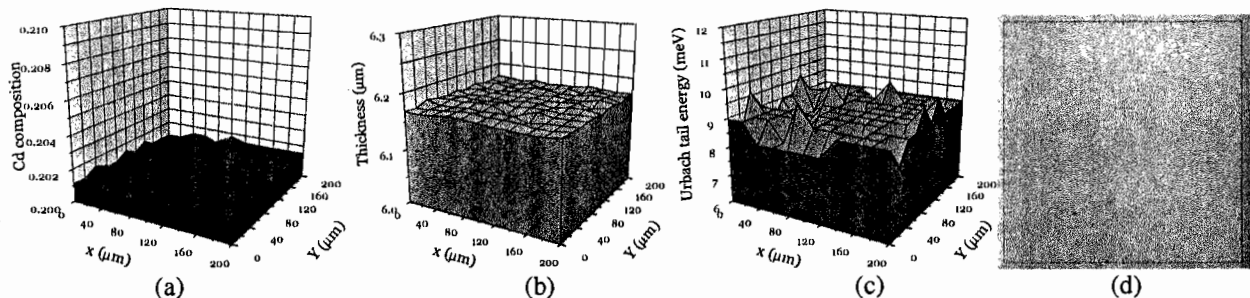


Fig.36. Composition, thickness and Urbach tail mapping results as well as a surface morphology photograph of a  $200\mu\text{m}\times 200\mu\text{m}$  area of a LWIR MBE HgCdTe sample. (a) composition; (b) thickness; (c) Urbach tail energy and (d) the surface morphology picture of the same scanned area.

The Urbach tail energy, which is dominated by contributions from electron-phonon interactions, alloy disorder and structural disorder, again was found to be capable of characterizing material quality.<sup>78</sup> Those samples with surface microtwin defects that correlate with low growth temperatures and with high dislocation densities always showed relatively high Urbach tail energies. We find that the Urbach tail energy has large values as well as large standard deviations over small areas, which suggests that non-uniformly distributed structural disorder dominates the nonuniformity of the device performance figures of merit in HgCdTe infrared focal plane detector arrays.

#### *Investigation of temperature dependent HgCdTe absorption behavior near the band edge*

We collected a library of values for the absorption coefficient  $\alpha$  as a function of energy, composition and temperature. We found the maximum measurable absorption coefficient to be determined by (1) the sample thickness, (2) the spectrometer analog-to-digital converter bit and (3) the noise level of the spectrometer, which is primarily determined by the dark current of the detector. The small thicknesses of MBE samples ( $<10\mu\text{m}$ ) allows one to make reliable measurements of the absorption coefficients up to  $5\times 10^3\text{cm}^{-1}$  in our Thermo Nicolet 870 research class FTIR spectrometer. However, from some thicker samples ( $>8\mu\text{m}$ ), the limitation due to analog to digital conversion in the spectrometer still can be observed. The thinner samples ( $<7\mu\text{m}$ ) give reliable measurements of  $\alpha$  down to  $10^4\text{cm}^{-1}$ . The thinner the sample thickness, the smaller is the value of the absorption coefficient that can be measured accurately. We are working on fitting the collected absorption coefficient library to an empirical formula. The absorption coefficient curve for HgCdTe always includes both the Urbach region, also called the Urbach tail, which follows the Urbach rule, and the intrinsic Kane region. A good model for fitting  $\alpha$  should be continuous and have a continuous first derivative at the point at which the absorption coefficient changes from following the Urbach rule to following the Kane rule, and simultaneously should have as few parameters as possible and have as small as possible a

<sup>78</sup> Y. Chang, G. Badano, J. Zhao, Y. D. Zhou, R. Ashokan, C. H. Grein and V. Nathan, J. Electron. Mater., 33, 709(2004)

correlation between the values of the parameters. This work will be discussed in detail in the followed section.

The Urbach region determines the response cut-off of a thick layer. In the Urbach region, the behavior of the optical absorption spectra is largely determined by the shape of the subband density of states for a disordered material. Specifically, a linear exponential dependence of the density of states on energy would give rise to Urbach's rule in the absorption spectrum. We have computed the band-tail density of states of HgCdTe to incorporate the influence of alloy disorder. A general formula was developed for electrons and holes in a correlated Gaussian random potential. A linear exponential density of states is found over more than an order of magnitude energy change in a crossover regime between a deep-tail Gaussian density of states and a Halperin-Lax form in the shallow-tail region. The theory suggests the following formula

for the Urbach slope  $A_{Alloy}$  due to alloy disorder alone:  $A_{Alloy} = \frac{x(1-x)|VBO|^2 m_{HH}^* L^2}{7.2\hbar^2}$ . Here, VBO is

the valence band offset,  $m_{HH}^*$  is the heavy hole mass,  $x$  is the alloy composition, and  $L$  is the disorder correlation length (estimated to be of the order of one interatomic spacing). This formula excludes disorder due to phonons and defects, and hence represents a lower bound for the low-temperature Urbach slope. Its utility lies in enabling a nondestructive optical assessment of material quality through comparison with the observed Urbach slopes. Within the adiabatic approximation, the Urbach tail energy  $W(T)$  can be expressed by the following formula:

$W(T) = A_{Alloy} + A_{Str} + B \coth\left(\frac{\hbar\omega_{LO}}{2kT}\right)$ . Here,  $A_{Str}$  gives the contribution of structural disorder, such as

the disorder introduced by defects or impurities,  $B$  is a constant which measures the electron-phonon coupling strength, and  $\hbar\omega_{LO}$  is the longitudinal optical phonon energy, which is a function of the cadmium composition  $x$  in HgCdTe<sup>79</sup>.

We fitted the temperature dependent absorption coefficients to obtain the above-mentioned parameters. Typical results for SWIR, MWIR and LWIR HgCdTe samples are shown in Table 9.

Table 9. Fitting results of temperature dependent Urbach tail energy (eV)

$x$	0.40	0.30	0.21
$A_{Alloy}$	0.0091	0.0080	0.0063
$A_{Str}$	0.0099	0.0032	0.0061
$B$	0.0012	0.0008	0.00067

The smallest structural disorder was found for the MWIR HgCdTe sample, which may be due to the fact that our CdZnTe substrates have a Zn composition of 0.035, which best matches the lattice constant of MWIR HgCdTe.

Using the equation for  $W(T)$ , we can map the alloy and structural disorder across a HgCdTe wafer, as shown in Fig.37, giving a way to explore the variations in sample quality across a HgCdTe MBE wafer.

<sup>79</sup> J. Baars, F. Sorger, Solid State Commun., 10, 875(1972)

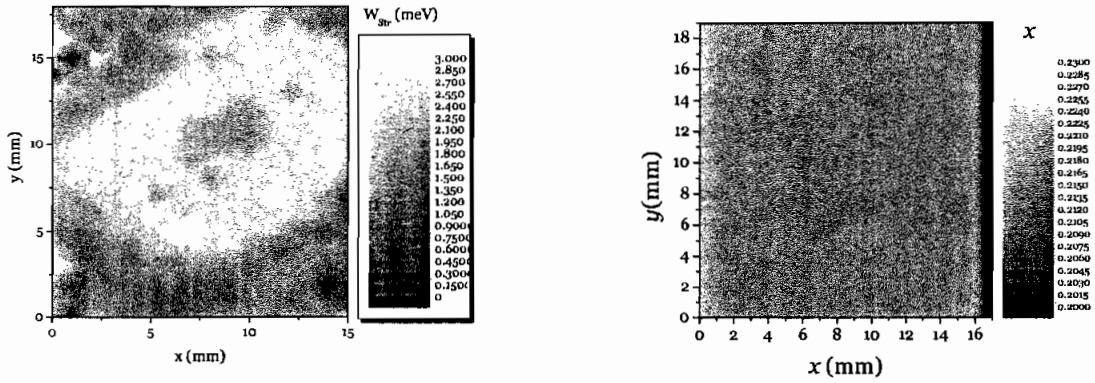


Fig.37. FTIR mapping results for the variations in structural disorder (left) and composition (right) that determine the total variation in alloy disorder

### Modeling HgCdTe absorption behavior near the bad edge including nonparabolicity and Urbach tail

According to energy band calculations, the conduction band energy  $E_c$  of HgCdTe can be written in the hyperbolic form:  $E_c = \sqrt{s^2 k^2 + b^2} - b + E_g$ , where  $s$  and  $b$  are parameters fit to describe the band structure of HgCdTe. Kane's 8-band  $k \cdot p$  model gives the values  $b = E_g/2$  and  $s = \pm \sqrt{2P^2/3}$ , which are the slopes of two asymptotes. Here,  $P$  is the momentum matrix element. A similar result can also be obtained for the light hole band, which is a hyperbola mirroring  $E_c - k$  in the energy range of 400 meV below the top of valance band. More precise 14-band  $k \cdot p$  calculations using a  $14 \times 14$  matrix<sup>80</sup> give similar hyperbolas describing the  $E_c$  or  $E_{lh}$  dispersion relations. However, the fits of 14-band results give values for both  $s$  and  $b$  different from those obtained from 8-band calculations. Specifically,  $E_c$  fits give  $s = 8850.01 \pm 10.20$  ( $\times 10^{-11} \text{ eV} \cdot \text{cm}$ ) and  $b = 103.354 \pm 2.035$  (meV) for 77K Hg<sub>0.23</sub>Cd<sub>0.77</sub>Te. Similar results for HgCdTe with a similar composition at 0 K were also obtained by Krishnamurthy *et al.* using a hybrid pseudopotential tight-binding method<sup>81</sup> for calculating the electronic band structure. The asymptotes of the hyperbola can be used to approximate the  $E_c$  dispersion relationship when  $E$  or  $k$  is large. Near 150 meV above the bottom of the conduction band, the dispersion relationship becomes linear. On the other hand, when  $k$  is small, the lowest order term of a Taylor series will give a reasonable approximation:

$$E_c = \frac{s^2}{2b} k^2 + E_g \quad (1)$$

which describes a parabolic  $E_c$  dispersion relationship near the  $\Gamma$  point. The electron effective mass is obtained from  $m_e^*/m_0 = \frac{\hbar^2 b}{s^2 m_0}$ . Noting that the optical matrix elements vary only slowly with  $k$ , and restricting our attention to energies near the band gap ( $-20 \text{ meV} \leq \hbar\omega - E_g \leq 400 \text{ meV}$ ), we discuss the absorption behavior assuming that the optical matrix elements can be treated as constant. The absorption coefficient of HgCdTe  $\alpha$  is given by the sum of absorption coefficient

<sup>80</sup> M. E. Flatte, P. M. Young, L.-H. Peng and H. Ehrenreich, Phys. Rev. B 53, 1963(1996)

<sup>81</sup> S. Krishnamurthy, A.-B. Chen and A. Sher, J. Appl. Phys., 80, 4045(1996)

involving light hole ( $\alpha_{lh}$ ) and heavy hole ( $\alpha_{hh}$ ) bands, and can be given as a function of  $\hbar\omega$  or  $\varepsilon = \hbar\omega - E_g$ :

$$\alpha = \alpha_{lh} + \alpha_{hh} = \frac{A}{\pi^2 s^3 (\varepsilon + E_g)} \left[ (\varepsilon + b) \sqrt{(\varepsilon + b)^2 - b^2} + \frac{1}{8} (\varepsilon + 2b) \sqrt{(\varepsilon + 2b)^2 - (2b)^2} \right]$$

$$= \frac{B}{\hbar\omega} \left[ (\hbar\omega - E_g + b) \sqrt{(\hbar\omega - E_g + b)^2 - b^2} + \frac{1}{8} (\hbar\omega - E_g + 2b) \sqrt{(\hbar\omega - E_g + 2b)^2 - (2b)^2} \right] \quad (2)$$

Note that  $A$  or  $B = A\pi^{-2}s^{-3}$  is a constant to be determined by fitting the experimental data; and recall that  $b$  is a parameter associated with the band structure and is also determined by fitting experimental data.

Eq. 2 was used to fit the experimentally measured absorption coefficient for a  $\text{Hg}_{0.79}\text{Cd}_{0.21}\text{Te}$  sample at 80K. The results are shown in Fig. 38.

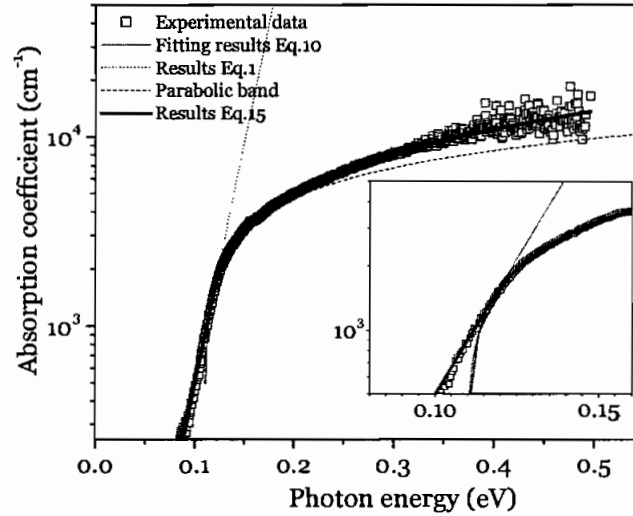


Fig. 38 Open squares: experimentally measured absorption coefficient of a  $\text{Hg}_{0.79}\text{Cd}_{0.21}\text{Te}$  sample at 80K; thin solid line: fitted Eq. 2 by assuming hyperbolic bands; dotted line: fitted Urbach tail (Eq.4) with  $E_0 = E_g + W/2$ ; dashed line: fitted assuming parabolic bands, which shows reasonably good agreement only very near the band gap; and thick solid line: fitted using Eq.2. The inset is a close-up of the main figure and shows that Eq.2 remains smooth at  $E_0$ .

When the photon energy is much larger than the absorption edge, i.e.  $\hbar\omega/E_g \gg 1$ , the conditions  $\varepsilon + 2b \gg 2b$  and  $\varepsilon + b \gg b$  will be met, and Eq. 2 can be rewritten as:

$$\alpha = \frac{A}{\pi^2 (\varepsilon + E_g)} \cdot \frac{1}{s^3} \cdot \frac{1}{8} [8(\varepsilon + b)^2 + (\varepsilon + 2b)^2] = \frac{C(\hbar\omega - E_g + D)^2 + F}{\hbar\omega} \quad (3)$$

where  $C = \frac{9A}{8s^3\pi^2}$ ,  $D = \frac{10}{9}b$  and  $F = \frac{A}{9s^3\pi^2}b^2$ . Note that the product of the absorption coefficient and the energy ( $\alpha\hbar\omega$ ) is proportional to the square of the energy when the energy is greater than  $E_g$  by hundreds of meV. Equation 3 can also be obtained if one substitutes the  $E_C(k)$  and  $E_{lh}(k)$  relations by the asymptotes of the hyperbola.

Within about 20 meV of the energy gap,  $\varepsilon = \hbar\omega - E_g \ll b$ , Eq. 2 can then be rewritten as  $\alpha = \frac{Ab^{\frac{3}{2}}}{\pi^2 s^3 (\hbar\omega)} \left[ \sqrt{2} + \frac{1}{2} \right] \cdot \sqrt{\hbar\omega - E_g}$ . An example is shown in Fig. 38. An empirical formula with a similar form has been suggested by Schacham et al.<sup>82</sup> from absorption very near the band gap in samples with thicknesses of 25  $\mu\text{m}$  to 300  $\mu\text{m}$ .

The aforementioned equations give a clear picture of the changing tendency of  $\alpha \cdot \hbar\omega$  with  $\hbar\omega$ , which can be combined into the formula  $\alpha \cdot \hbar\omega \propto \varepsilon^{f(\varepsilon)}$ , where  $f(\varepsilon)$  is a function of  $\varepsilon$  taking the values from 0.5 to 2.  $f(\varepsilon) = 0.5$  when  $\varepsilon$  is very small. With increasing  $\varepsilon$ ,  $f(\varepsilon)$  gradually increases. When  $\varepsilon$  is very large,  $f(\varepsilon)$  takes on the value 2. Therefore, depending on the range of energy above the band gap, an empirical formula of  $\alpha \cdot \hbar\omega \propto \varepsilon^\gamma$  ( $0.5 \leq \gamma \leq 2$ ) can be used to describe the energy dependence of the absorption coefficient near the band gap, where  $\gamma = \frac{1}{n} \sum_n f(\varepsilon_i)$ , i.e. an average over  $n$  energy points taken into account during the fitting calculations above  $E_g$ . Moazzami et al. has empirically determined a  $\gamma$  value of about 0.7 for a  $\text{Hg}_{0.69}\text{Cd}_{0.31}\text{Te}$  sample in the energy range of about 100meV.<sup>83</sup> Chu and coworkers found that a logarithmic approximation works best for energies  $\sim 100\text{meV}$  above the energy gap.<sup>84</sup>

The absorption coefficient below the energy gap is expected to follow the Urbach rule and can be written as:

$$\alpha = \exp[(\hbar\omega - E_0)/W] = \alpha_0 \exp(\hbar\omega/W) \quad (\hbar\omega < E_0) \quad (4)$$

where  $\alpha_0$  is the absorption coefficient at the energy of  $E_0$ , and  $W$  is the Urbach energy in the same units as  $\hbar\omega$ , describing the steepness of the Urbach absorption tail. To guarantee a smooth connection between the Urbach region  $\alpha_U$  (as given by Eq. 4) and the intrinsic region  $\alpha_I$  (as given by Eq.2), we require:

$$\left\{ \begin{array}{l} \alpha_U|_{\hbar\omega=E_0} = \alpha_I|_{\hbar\omega=E_0} \\ \frac{d(\alpha_U)}{d(\hbar\omega)}|_{\hbar\omega=E_0} = \frac{d(\alpha_I)}{d(\hbar\omega)}|_{\hbar\omega=E_0} \end{array} \right. \quad (5)$$

Because the Urbach tail energy spans only a few meV, the corresponding  $k$  is very small. Using Eq.4 to approximate  $E_c(k)$  and  $E_{th}(k)$ , we obtain from (5) the condition:

$$E_0 \cong E_g + \frac{W}{2} \quad (6)$$

Recall that  $W$  is the Urbach tail energy.  $E_0$  is the point at which the absorption coefficient transitions from Urbach's rule to the intrinsic band-to-band behavior.  $E_0$  was defined as the optical energy band gap of  $\text{HgCdTe}$  by Chu et al.<sup>85</sup> The first derivative of the absorption coefficient peaks at  $E_0$  because the rapid rise of the absorption coefficient following the exponential Urbach rule stops at this point<sup>86</sup>. Similar suggestions were made by Ariel et al.<sup>87</sup>

<sup>82</sup> S.E. Schacham and E. Finkman, J. Appl. Phys., 57, 2001(1985)

<sup>83</sup> K. Moazzami, J. Phillips, D. Lee, S. Krishnamurthy, B. Benoit, F. Fink and T. Tiwald, J. Electron. Mater. 34, 773(2005)

<sup>84</sup> B. Li, Y.S. Gui, H. J. Ye, J.H.Chu and S. Krishnamurthy, J. Appl. Phys., 83, 7668(1998)

<sup>85</sup> J. H. Chu, S. Q. Xu and D. Y. Tang, Appl. Phys. Lett., 43, 1064(1983)

<sup>86</sup> B. Li, Y. Wu, Y. S. Gui, H. J. Ye, Y. Chang, L. He and J. H. Chu, Appl. Phys. Lett., 73, 1376(1998)

The combination of Eqs. 2, 4 and 6 gives the absorption coefficient near the band gap  $E_g$  as:

$$\alpha(\hbar\omega) = \begin{cases} \frac{B}{E_g + W/2} \left[ (W/2 + b) \sqrt{(W/2 + b)^2 - b^2} + \frac{1}{8} (W/2 + 2b) \sqrt{(W/2 + 2b)^2 - (2b)^2} \right] \exp\left(\frac{\hbar\omega}{W}\right) & (\hbar\omega \leq E_g + W/2) \\ \frac{B}{\hbar\omega} \left[ (\hbar\omega - E_g + b) \sqrt{(\hbar\omega - E_g + b)^2 - b^2} + \frac{1}{8} (\hbar\omega - E_g + 2b) \sqrt{(\hbar\omega - E_g + 2b)^2 - (2b)^2} \right] & (\hbar\omega \geq E_g + W/2) \end{cases} \quad (7)$$

This formula was plotted in Fig. 38 and gives good agreement with experiment both below and above  $E_0$ . If under certain circumstances  $W$  is so large as to be beyond the energy region in which the absorption coefficient is proportional to  $\epsilon^\gamma$  ( $0.5 < \gamma \leq 2$ ), then the following relationship can be obtained from Eq.5:  $E_0 \cong E_g + \gamma \cdot W$ .

In conclusion, an analytical model describing the absorption behavior of HgCdTe as a function of absorbed photon energy was established based on k.p band structure calculations. The model is capable of describing both the Urbach tail region and the intrinsic region up to tenths of an eV above the band gap. The intrinsic band-to-band absorption coefficient is proportional to  $(\hbar\omega - E_g)^\gamma$  with  $\gamma$  increasing from 0.5 to 2 with increasing photon energy, a consequence of the nonparabolic conduction and light hole band dispersion relationships. Good agreement was found between the experimental and theoretical results. These formulas establish a theoretical framework with which to precisely describe the absorption coefficient as a function of composition and temperature by fitting our experimental database.

### Summary of achievements

Achievements in MBE growth:

- Worked with MBE equipment vendor (Applied EPI) to develop a continuous-feed valved Hg cell.
- Experimentally measured the dependence of the nucleation/growth mode on temperature at certain Hg fluxes to achieve optimized growth.
- Developed an improved model for thermodynamic equivalent growth conditions.
- Used optimized interfacial layers in our MBE growth and discovered defect suppression mechanisms.
- Obtained better growth control: HgCdTe epilayers with recombination lifetimes close to the theoretical limits were consistently grown.
- Employed RHEED intensity as an *in situ* quantifiable characterization tool for the MBE growth of HgCdTe.
- Demonstrated that *in situ* SE can be used to accurately control both temperature and composition.

Achievements in *in situ* characterization,

- Collected data and formed a new optical constant library to improve the precision of the *in situ* SE parameters.
- Performed SE characterization of substrate surfaces before growth. We can measure the temperature using a critical point model of the dielectric function. We found the correlation between surface roughness and the quality of the layers.

---

<sup>87</sup> V. Ariel, V. Garber, G. Bahir, A. Raizman and A. Sher, Appl. Phys. Lett., 70, 1849(1997)

- Elucidated the interaction of Hg with the substrate surface, which is of great practical and theoretical interest to understand HgCdTe MBE nucleation.
- Investigated the effects of Hg on the dielectric function, and measured the relative abundance of chemisorbed and physisorbed Hg. This result is helpful for us to improve run-to-run reproducibility.
- Found a correlation between the average *in situ* depolarization coefficient  $u$  and the recombination lifetimes. This indicates that  $u$  may offer an early warning of the degeneration of material quality during growth.
- Simultaneously found CdZnTe values of  $y$  and  $T$  from the SE data and tested against known compositions and temperatures. The SE values were found to be sufficiently precise to be useful.

Achievements in *ex situ* characterization and theoretical modeling,

- Validated the conventional recombination lifetime model using 14-band k.p bandstructure and lifetime calculations. Also, the computed band structures were validated by our optical data.
- Established an analytical model for the HgCdTe absorption behavior near the optical band gap (including Kane region and Urbach tails). It supersedes all other theoretical and empirical published models.
- Formed database of  $\alpha(\omega;x,T)$  for MBE HgCdTe (including Kane region and Urbach tails).
- Employed our newly developed model for alloy disorder contributions to analyze the Urbach tail and map structural disorder.
- Developed an infrared transmission mapping technique to map both CdZnTe substrates and HgCdTe epilayers to obtain the composition, Urbach tail energy and epilayer thickness.
- Studied the macroscopic and microscopic uniformity of HgCdTe.
- Performed enhanced recombination lifetime measurements and fittings to obtain better accuracy and reduced parameter correlations. Free software was developed and made available to the US infrared community.

In summary, we have established a reproducible and portable method to grow high quality multi-layer device structures. We fabricated 2-color detectors and IRFPAs based on these methods. The associated technology, including established techniques and software, has been transferred to the US infrared industry. Graduate student training also provides skilled manpower to the US infrared community.

### ***C. Microstructure of MBE-Grown HgCdTe/CdZnTe(211)B Heterostructures***

In this part of the project, a range of advanced electron microscopy methods were used to investigate the film morphology and various defects associated with the growth of HgCdTe heterostructures. The following summarizes the important outcomes of this work.

#### **Surface defects**

i) Surface crater defects in HgCdTe were associated with finely-spaced HgCdTe/Te intergrowths with either semi-coherent or incoherent grain boundaries, and small HgCdTe inclusions embedded within Te grains.

ii) Surface ridges were caused by faceted HgCdTe surfaces, and were found to be associated with substantial twinning within the CdTe capping layer.

iii) Surface needles with “volcano”-shape originated from lower part of HgCdTe film, but NOT usually from substrate. Columnar twins from the lower part of the HgCdTe films were present underneath defects.

### Interfacial layers

i) alleviated misfit with substrate, leading to higher quality material.

### Effects of annealing

- i) loss of interface abruptness between epilayers.
- ii) defect reduction

### TEM sample preparation/ effect of ion-milling

i) The sample must be maintained at liquid nitrogen temperature to avoid ion-milling-induced damage effects associated primarily with creation and diffusion of Hg interstitials.

## II. SiGe/Si Quantum Dot Infrared Photodetectors (Wang)

The UCLA group has made considerable progress on the MURI Centroid program sponsored by the Army Research Office in the development of Ge quantum dot infrared photodetectors (QDIPs) for five years of 2001-2006. The effort was focused on i) fabrication and investigation of Ge quantum dot superlattice p-i-p structure, ii) tuning the response wavelength by strain, Ge content, Ge dot height and annealing, iii) photocurrent and dark current measurement of Ge QDIP structures, iv) current blocking layer study, v) investigating the growth of small Ge dots on diblock copolymer nano-patterned substrates to obtain high (height-to-size) aspect ratio diblock copolymer nano-patterned substrates, and vi) FTIR spectroscopy for different numbers of stacked layers with different doping levels. We summarized some of our results below. Details of the results can be found in the published papers listed in the end of this report.

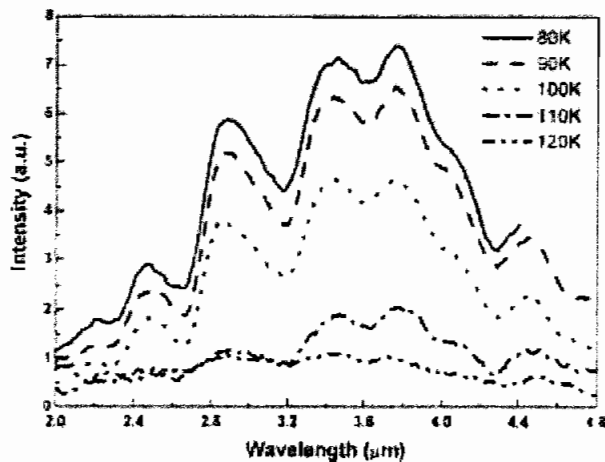


Fig. 1. Photoresponse of the 900 °C and 10 min annealed sample at different temperatures.

Molecular beam epitaxy grown Ge dots photodetectors were fabricated. The structure was a *p-i-p* with *p*-type doped Ge dots embedded in the intrinsic layer sandwiched in between the two heavily *p*-doped regions. As-grown samples had a response range from 2.2  $\mu\text{m}$  to 3.2  $\mu\text{m}$ . Thermal annealing at 900  $^{\circ}\text{C}$  for 10 min shifted the peak response to 3.6  $\mu\text{m}$  (Fig. 1). The effect of annealing was simulated by modeling the inter-diffusion behavior of Ge and Si atoms to explain the shift of the response wavelength (Fig. 2). The normal incident response from boron-doped Ge QDs was ascribed to transitions from heavy hole ground states to continuum states in the valence band. The response wavelength calculations agreed with the experimental results. It was also pointed out that lower Ge content and smaller dots were more favorable for longer wavelength range responses. To achieve this, smaller nominal Ge growth thickness and relatively higher growth temperatures were used (J. Appl. Phys., Vol. 96, No. 1, 1 July 2004).

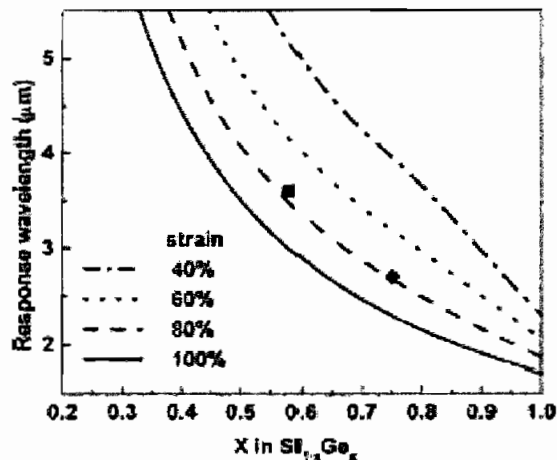


Fig. 2. Calculated results of the peak response wavelength dependent of the Ge content and Ge QDs strain ratio for QDs of 9 nm in height and 100 nm in the base. The diamond and square signs indicate the points for the as-grown sample and the annealed sample, respectively.

The *p*-type Ge QDIP was based on a *P-I-P* structure, where the dots were doped with Boron. Fig. 3 shows the normal incidence photoresponse spectra recorded at different temperatures for a sample grown at 700 $^{\circ}\text{C}$ . The device had a response in the range of 2.8-4.8 $\mu\text{m}$ , with a main peak at around 3.5 $\mu\text{m}$ . This response is due to the hole absorption of photons in the valence band in Ge dots. Once the holes in Ge dots absorbed photons, they were excited to the band edge and swept by the electrical field. This is schematically shown in Fig. 4. For more details about this project, please see our recent paper (in Optical Materials 27, 1097-1100, 2005).

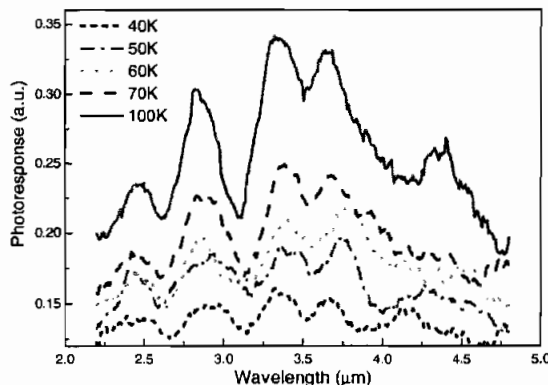


Fig. 3. Photoresponse spectra taken at different measurement temperatures. The growth temperature for the sample was 700  $^{\circ}\text{C}$ , and the doping level during Ge dots growth was  $6 \times 10^{18} \text{ cm}^{-3}$ .

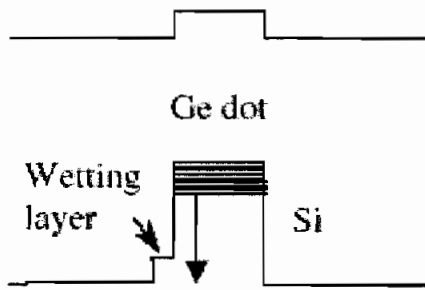


Fig. 4. Band diagram

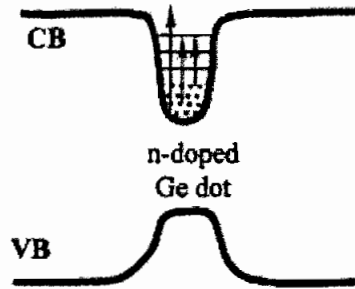


Fig. 5. The bandgrams of Ge quantum dot in the Si matrix with phosphorus  $\delta$ -doping.

Our successful development of an N-I-N Ge QDIP was based on delta-doping the Ge dots with phosphorus. The photoresponse was ascribed to the transitions of electrons in the Ge dots as illustrated in Fig. 5. Without doping, it is well established that the Ge dot in a Si matrix has type-II band alignment with the main offset in the valence band, as shown above. However, with phosphorus-doping in the Ge regions, self-consistent Hartree-Fock potential wells are induced in the conduction band as shown here. Quantized energy levels are formed due to the reduced dimensionality for a few nanometers height of the Ge dots in the growth direction. Electrons occupy the low-energy levels. Excitation of electrons from the ground states to higher-energy levels and the conduction-band edge by absorbing photons generates photocurrent under applied electric field. The broad response spectra might come from different sizes of the dots, as well as from the fact that more than one quantum levels were involved in the absorption. As shown in Fig. 6, our n-type detectors show a response in the mid-infrared and long-infrared wavelength ranges (Appl. Phys. Lett. 87, 081104, 2005).

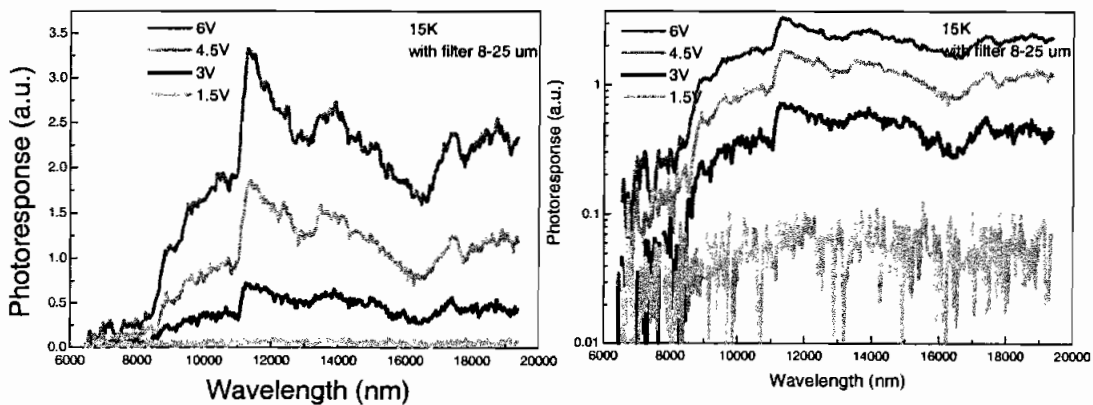


Fig. 6. (a) Photoresponse spectrum in the mid-IR range at 1.5 V bias taken with a 2–5  $\mu\text{m}$  band pass filter. (b) Spectra in the far-IR range at various biases taken with an 8–25  $\mu\text{m}$  band pass filter. Note that in this plot, the y axis is in logarithmic scale. Light is incident normally for both (a) and (b).

We have calibrated the responsivity of our N-I-N device using a commercially available MCT detector (Fig. 7). Upon calibration, we found our device to have a peak responsivity of 1.2 mA/W at a bias of 6V. Detectivity was calculated using the calibrated responsivity and assuming shot noise as the dominant dark current noise mechanism. Due to large dark currents at high bias and low responsivity at low bias, the detectivity was calculated at a bias of 3V. At the peak wavelength of 11.25  $\mu\text{m}$ , the device detectivity was calculated to be  $1.17 \times 10^9 \text{ cm}\cdot\text{Hz}^{1/2}/\text{W}$ .

We have demonstrated infrared absorption in Ge dots grown on nano-patterned substrates of 20 nm. The pattern was created using a PS-PMMA diblock copolymer and was subsequently transferred to an underlying  $\text{SiO}_2$  layer. Using selective epitaxial growth, layers of Ge dots (15 nm base, 7 nm height) were grown on the Si substrate (Fig. 8). In order to achieve infrared absorption between valence band states, the dots were doped with boron at a concentration to  $10^{20} \text{ cm}^{-3}$ . The FTIR absorbance spectra of these dots showed different polarization dependences from that of previously reported pancake-like Ge dots ( $\sim 100 \text{ nm}$  in base and 7 nm in height). It is suggested that the 3.3  $\mu\text{m}$  and 8  $\mu\text{m}$  peaks in dots grown by nano-patterning arises from a transition other than the HH-LH or HH-SO transition at 3.1  $\mu\text{m}$  in pancake-like dots (Fig. 9). Additionally, the 3.3  $\mu\text{m}$ , 5.7  $\mu\text{m}$ , and 8  $\mu\text{m}$  absorption peaks in the nano-patterned sample yielded a non-zero absorbance at  $90^\circ$  polarization, showing that these small dots exhibit normal-incidence absorption. We expect that reducing the dot base dimension would improve normal-incidence absorption with additional lateral confinement of the smaller dots. Further study in simulation should be performed to calculate expected transition energies between the valence band states in these dots.

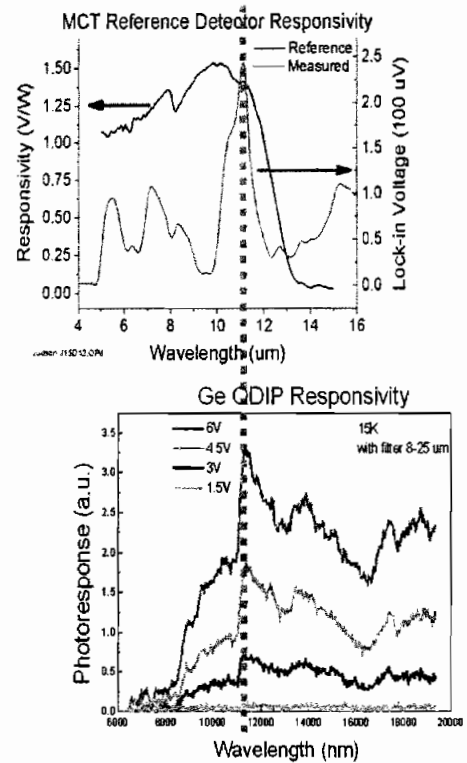


Fig. 7. Responsi calibration.

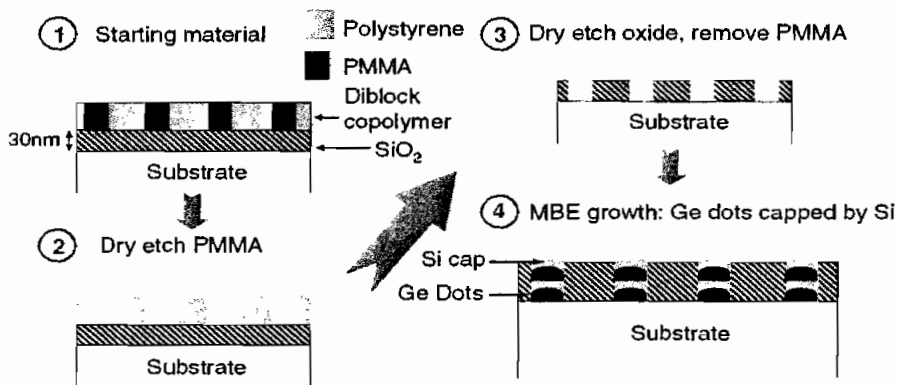


Fig. 8. Creating the nano-pattern. (1) PS separated from PMMA in regularly-spaced hexagonal-close-packed arrangement. Underlying substrate is  $\text{SiO}_2$  on Si. (2) Dry etch of PMMA in  $\text{C}_2\text{F}_6$  plasma. (3) Dry etch of oxide ( $\text{C}_2\text{F}_6$  plasma), followed by removal of PMMA. (4) MBE growth of Ge dots capped by Si. Dots were selectively grown on Si substrate.

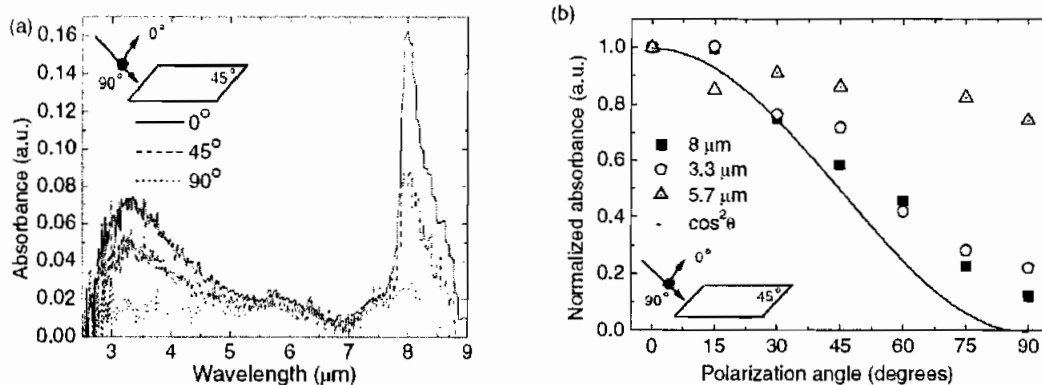


Fig. 9. (a) FTIR spectra for sample C (dot size: 15 nm base, 7 nm height), after baseline subtraction and smoothing. Polarization is indicated in inset. A  $90^\circ$  polarized background spectrum was used for all 3 curves. (b) Normalized peak absorbances versus polarization angle (compared to  $\cos^2\theta$  dependence of quantum wells). Peaks at 8  $\mu\text{m}$  and 3.3  $\mu\text{m}$  show strong polarization dependence. All peaks show a stronger absorbance at  $90^\circ$  than that predicted by quantum theory.

### III. III-V Based Quantum Dot Infrared Photodetectors (Bhattacharya, Goldman, Norris, Singh)

#### A. Theoretical Studies on Quantum Dot Intersublevel Detectors (Singh)

##### Introduction

Self assembled quantum dots based on strained epitaxy have been shown to have useful properties for applications in optoelectronics. Both band to band and inter-subband devices have been demonstrated. In this MURI program our goal is to exploit these devices for long wavelength detectors. Since the start of the program we have made contributions on the following fronts: 1) Developed an atomistic computer simulation program to calculate the configuration-energy diagram for self assembled dots. This has allowed us to evaluate the strain tensor and to understand why certain sizes and shapes are chosen during epitaxy. These are the first calculations for configuration energy diagrams for self-assembled dots; 2) Develop a 8 band k.p model to study the electronic structure of the self assembled dots. The strain tensor is included in this model via deformation potential theory. The work has been done for zinc-blende, diamond and wurtzite structures; 3) Calculate the oscillator strength of the inter-subband transitions; 4) Calculate transport properties of electrons in self-assembled dots; 5) Provide a theoretical framework on how quantum dots can help performance of severely lattice mismatched devices with high dislocation densities.

We will briefly outline our findings in the next section.

##### Results

In this section we will discuss the results obtained on the five topics mentioned above.

##### Configuration energy studies:

When we examine the configuration energy diagrams calculate by us we see that the Energy difference between various possible configurations (i.e sizes and shapes) is only a few meV per unit cell. Since the growth occurs at temperatures where  $kT$  is of the order of 50 meV it is important to understand why there is good uniformity in the dot sizes and shapes. We have calculated the entropy term  $TS=k \ln W$  where  $W$  is the degeneracy of the dot configurations. Our findings show that the  $TS$  term only causes changes of 0.1 meV i.e a value much smaller than  $kT$ . This explains why even a meV difference per unit cell causes strong size/shape selection. In Figure 1 we show our calculated results on how buried stressors influence the configuration energy diagram. Results are shown for the strain energy (in eV) per unit cell for no stressor, pyramidal stressors (e.g self assembled dots) and cubic dots. We see that there is considerable selection when stressors are used. We also find that if cubic stressors can be used the uniformity of dots will be greatly improved.

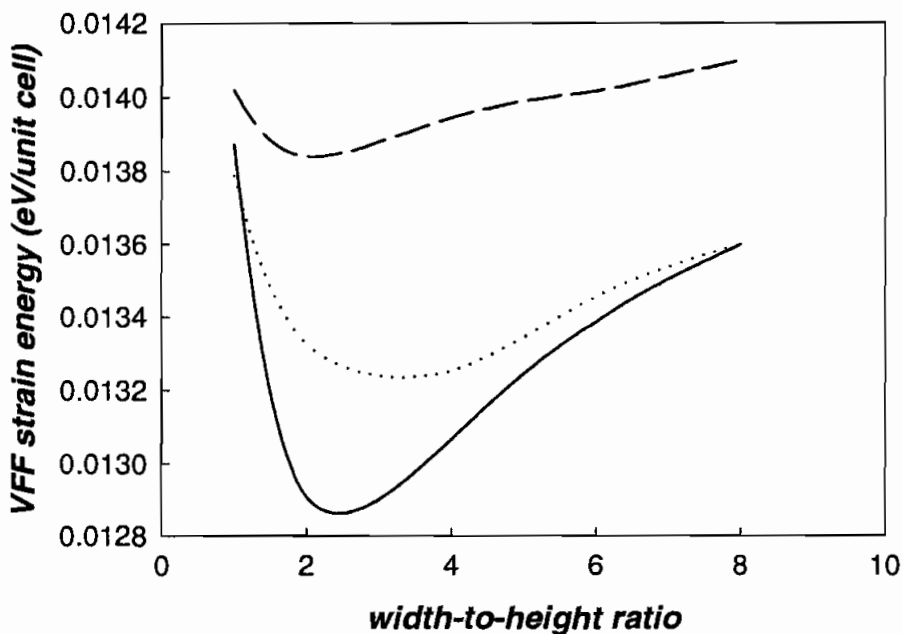


Figure 1 Calculated results on how buried stressors influence the configuration energy diagram. Results are shown for the strain energy (in eV) per unit cell for no stressor (top curve), pyramidal stressors (middle curve) and cubic dots (lowest curve).

*a) Self assembled nitride dots*

We have extended our formalism for configuration energy and bandstructure to the wurtzite structure. In Figure 2 we show results for strain tensor components in 20% InGa<sub>N</sub>/ Ga<sub>N</sub> self assembled dots. Notice the large values of strain in this system. The InGa<sub>N</sub>/Ga<sub>N</sub> system has a large piezoelectric effect which influences the confinement potential. In Figure 2 we show results the strain tensor in a InGa<sub>N</sub>/Ga<sub>N</sub> dot. These values are incorporated to calculate the electronic and optical response of the dots.

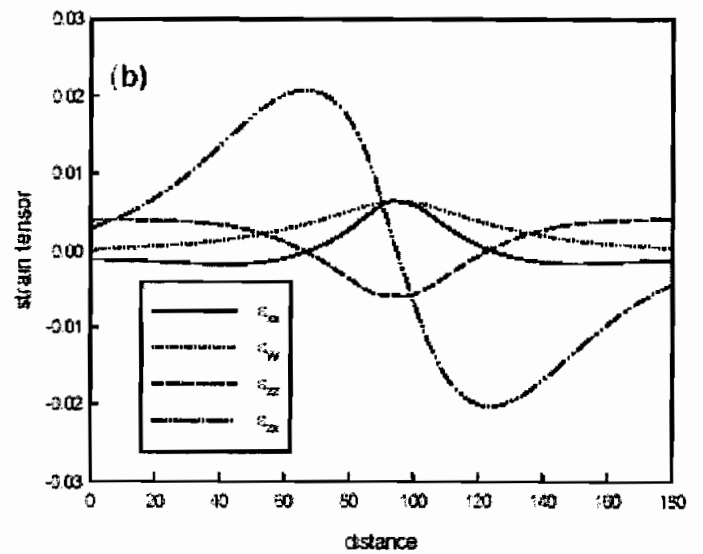
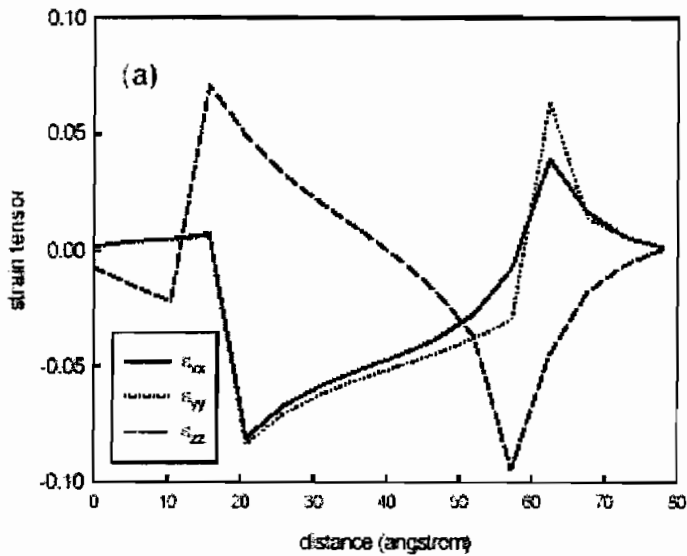
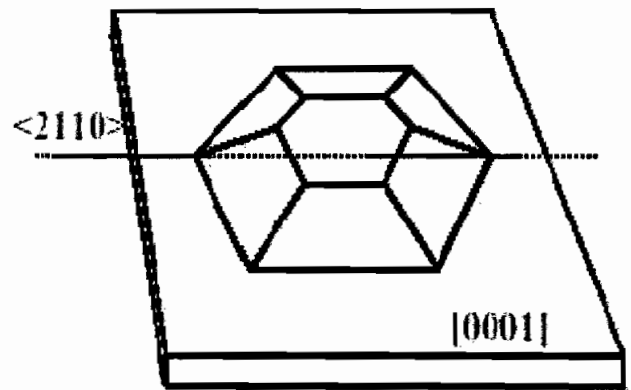
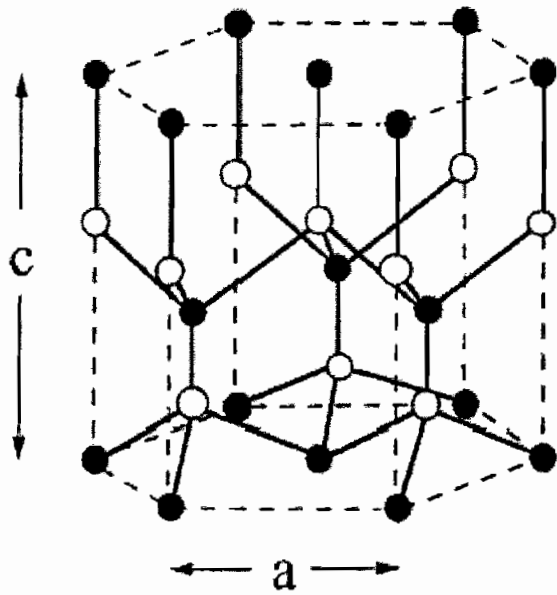


Figure 2 Results for strain tensor components in 20% InGaN/ GaN self assembled dots.

### 8 Band k.p studies:

We have developed an 8 band k.p method to examine the electronic levels for a variety of quantum dots. These include InGaAs/GaAs (i.e. zinc blende); Si/Ge (i.e diamond) and

InGaN/GaN (i.e wurtzite). We can find the electronic structure of an arbitrary shaped dot with variable strain distributions. In Fig. 3 we show some typical results.

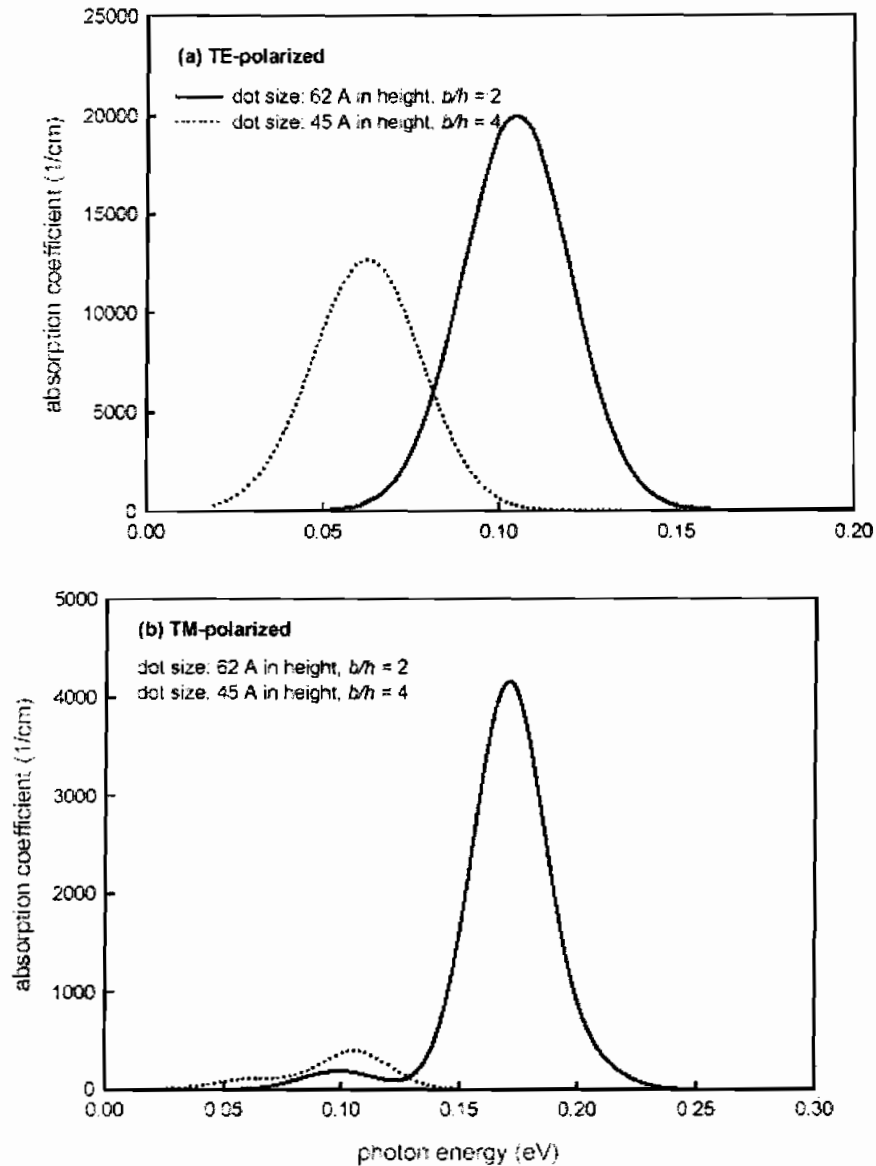


Figure 3 Results for inter-subband absorption energy in the InGaAs/GaAs dot. Shown are the optical absorption for two polarizations.

We have also applied the k.p method to examine dot in well (DWELL) structures as shown in Fig. 4.

The DWELL structure can have a high multiplication factor due to electron-electron scattering induced carrier multiplication as discussed below.

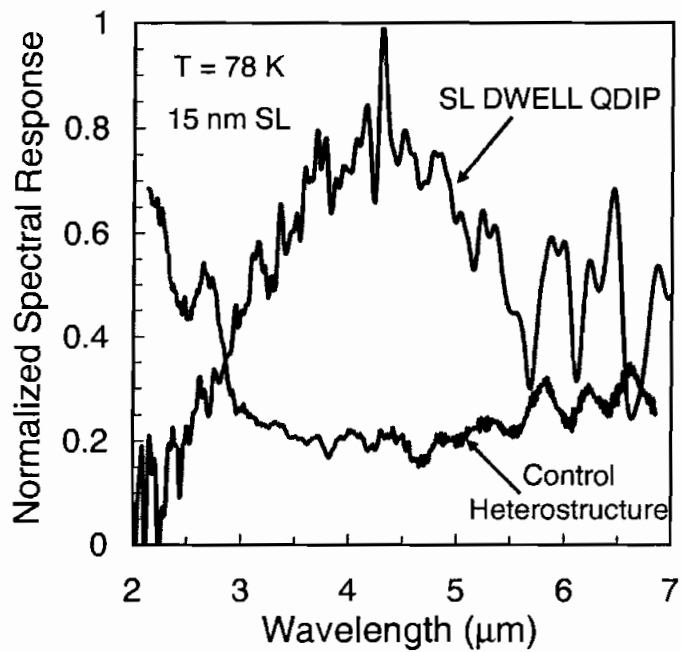
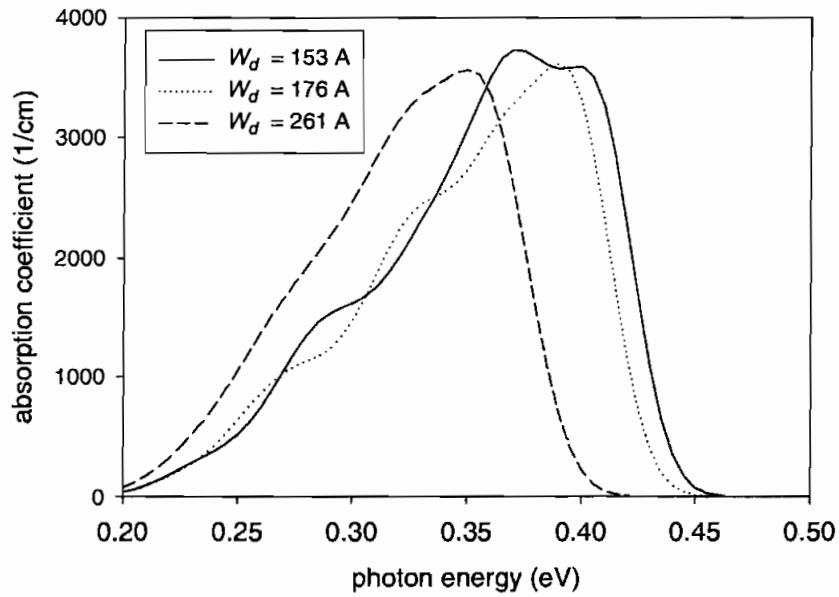
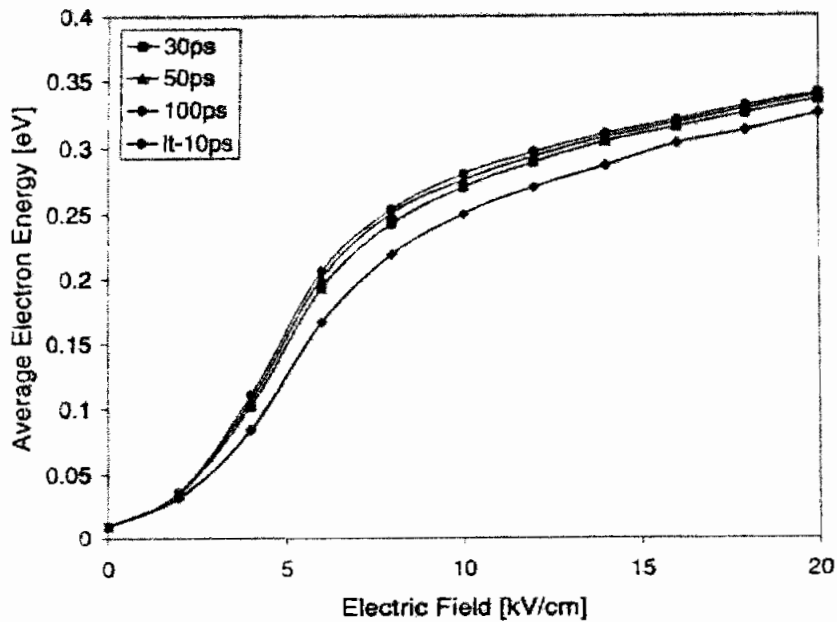


Figure 4. Theoretical and experimental absorption in dot in well structures.

### Transport studies

We have carried out transport studies in self assembled dots using Monte Carlo techniques. In particular we have applied these studies to understand the source of high responsivity in dot in well or DWELL structure. Our previous work has shown that there is little

difference in the absorption strength between normal dots and the DWELL structure. Yet the responsivity values are much higher in the DWELL. We find that this is related to a higher electron-electron scattering in the DWELL structure which leads to impact ionization related gain. Here a photoexcited carrier gains energy from the field and excites an electron in a dot to higher energy to make it mobile. In Figure 5 we show the energy gained by an electron under an applied field. This energy leads to impact ionization process. We see that the electron energies are of the order of 0.2-0.3 eV when the applied field is 10-20 kV/cm. At these energies the electrons can transfer their energy to an electron trapped in a dot. In the DWELL structure this possibility is high since there is a greater overlap between the hot electron and the localized electron. We estimate that the impact ionization is an order of magnitude higher.



Average carrier energy in a bound-to-continuum detector for various values of low-field capture time.

Figure 5. Results of Monte Carlo studies on electron transport in quantum dot structures.

### *Role of quantum dots in high dislocation devices*

We have examined how self-assembled dots can help radiative recombination by suppressing non-radiative recombination in structures with high dislocation densities. Such structures arise from lattice mismatched growth. Normally dislocations are a source of carrier capture and loss. However, our transport studies show that dots can suppress lateral carrier diffusion and thus suppress non-radiative processes.

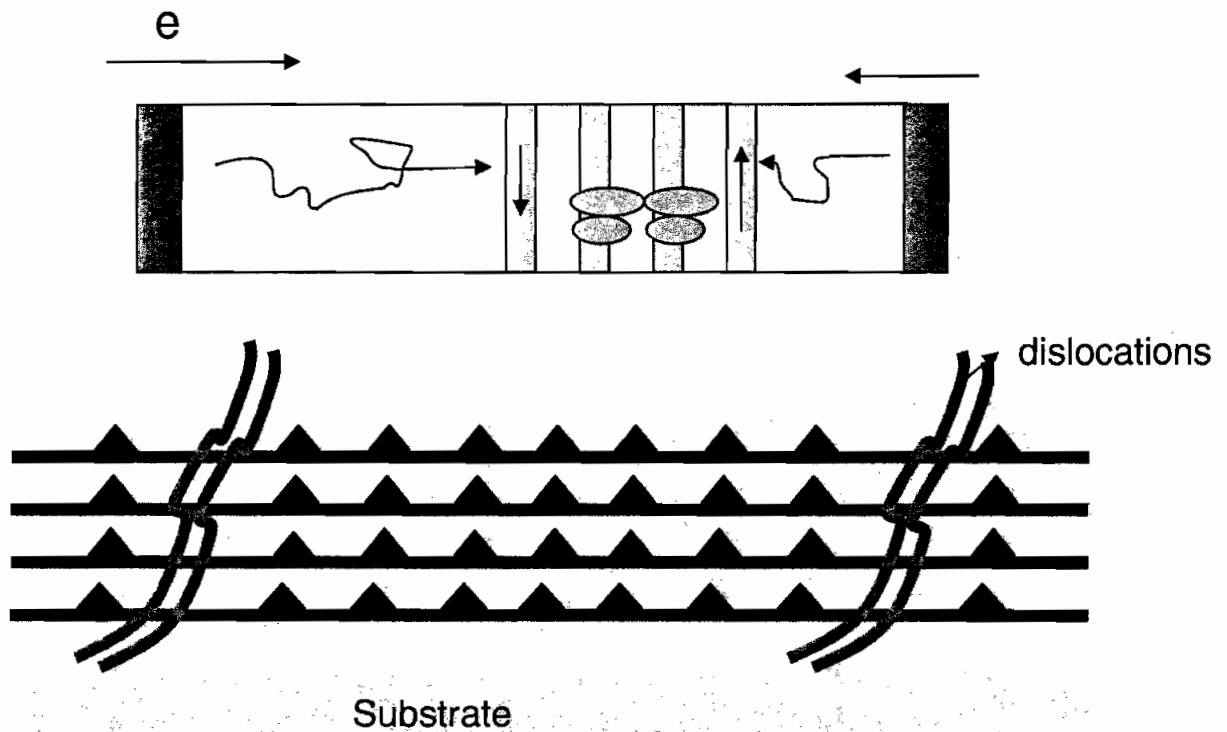


Fig.6 In presence of dislocations quantum dots can enhance radiative processes by keeping the carriers from the dislocations.

## Conclusions

In this 5 year MURI program we have examined structural, electronic, optical and transport issues in self-assembled quantum dots. A range of material systems (InGaAs/GaAs, Si/Ge and InGaN/GaN) have been studied. We have worked closely with our experimental team members to validate our models and guide and interpret the experiments.

### *B. Material Studies on InAs/GaAs QDIPs (Goldman)*

In the past decade, strain-induced self-assembled quantum dots (QDs) have enabled enormous advances in optoelectronics, including high performance infrared light-emitters and detectors. Further advances in light-emitters and detectors will require a narrowing of the density of states, which may be achieved through an improved understanding and control of the electronic effects of QD composition, size, and shape. A number of reports have suggested that QDs often have non-uniform compositions across their width and height. For example, both cross-sectional scanning tunneling microscopy (XSTM) [1] and diffraction-contrast transmission electron microscopy [2] have suggested the presence of In enrichment towards the center of the InAs/GaAs QDs, with alloy formation occurring towards the QD edge. To date, most scanning tunneling spectroscopy (STS) measurements of QDs have focused on plan-view measurements

of uncapped epitaxial QDs or colloidal QDs, with one report of cross-section STS on an individual QD within a coupled-QD multilayer [3]. Thus, the effect of composition gradients on the confined states in QDs remains unknown. Therefore, we have explored these effects in individual (uncoupled) QDs using a combination of XSTM and STS.

The QD heterostructures containing a series of 1-, 3-, and 8-period superlattices (SLs) consisting of 3 ML InAs and 50 nm GaAs were grown by atomic-layer epitaxy. In order to prevent the interaction of strain fields from different SLs, as well as to provide a marker, each layer of SLs was separated by 20 or 40 nm of AlAs/GaAs short-period SLs sandwiched between two 70 nm GaAs layer. XSTM images reveal uncoupled QDs, with typically ~50 nm diameters and ~20 nm heights. STS spectra were acquired from different locations within the QDs, in comparison with regions of clean GaAs within the spacer layers. The STS data reveal a very small (~0.2 eV) effective bandgap of the QD core, suggesting the presence of a bulk-like InAs. Near the edge of the QD, STS data reveal a more substantive effective bandgap (~1.0eV), suggesting significant quantization near the QD edge.

I

In Fig. 1 (left), an XSTM image reveals a fairly large InAs/GaAs QD. Figure 1 (right) presents STS spectra acquired from different locations in the QD shown in Fig. 1 (left), in comparison with a region of clean GaAs (in the spacer). The STS data reveal a very small effective bandgap of the QD core, suggesting the presence of bulk-like InAs. Near the edge of the QD, STS data reveal a more substantial effective bandgap, suggesting significant quantization near the QD edge.

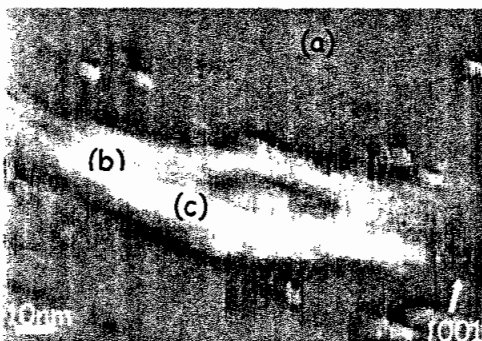
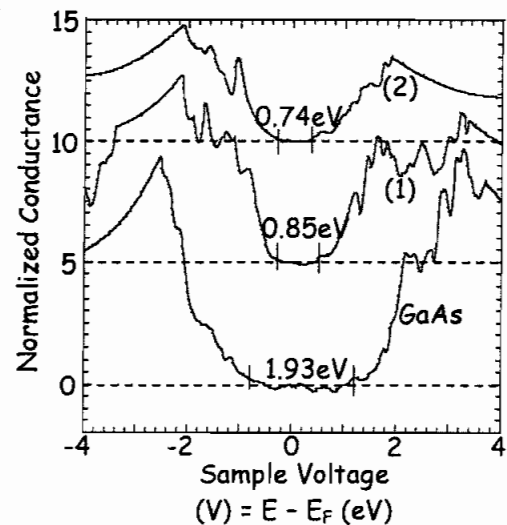


Fig. 1: Spatially resolved STS spectra (right) acquired within a “large” QD (left: b, c) and GaAs spacer (left: a). The sample voltage corresponds to the energy of the state relative to the Fermi level. The valence and conduction band edges are indicated by vertical lines at negative and positive sample voltages, respectively.



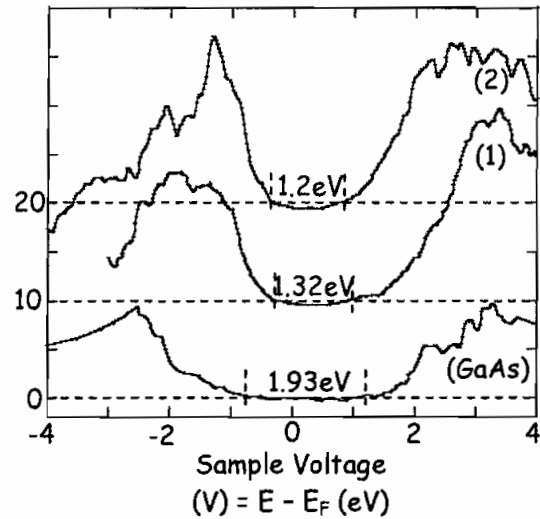
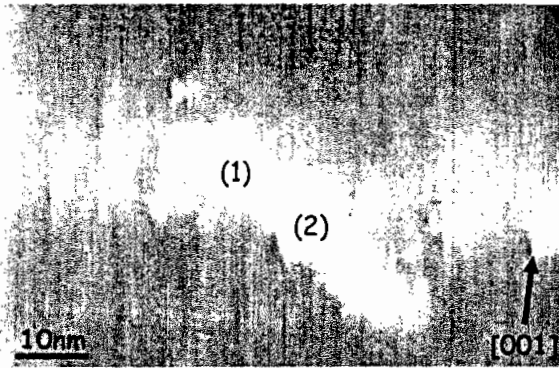


Fig. 2: Spatially resolved STS spectra (right) acquired within a “small” QD [left: (1), (2)] and GaAs region. The sample voltage corresponds to the energy of the state relative to the Fermi level. The valence and conduction band edges are indicated by vertical lines at negative and positive sample voltages, respectively.

Early attempts of (100)-oriented wafers, including CZT1 and CZT2, resulted in the samples breaking in the jaws of the sample holder, resulting in a surface with significant surface topography, unsuitable for XSTM measurements. However, flat cleaves were obtained for (111) oriented wafers cleaved along (110), as in sample CZT3, shown in Fig. 3(b). We note that the flat cleave shown in Fig. 3(b) was obtained *without* the substrate thinning usually required for III-Vs, presumably due to the softness of the II-VI crystals. This is very promising for timely XSTM, with a high fraction of atomically flat cleaves.

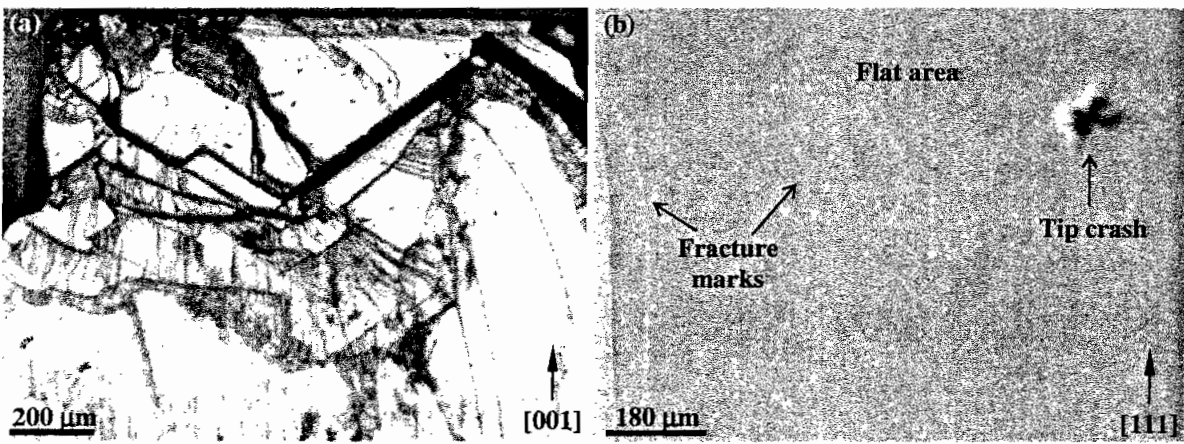


Fig. 3: Optical microscopy images of cleaved CZT (110) surfaces: (a) (001)-oriented undoped CZT, showing significant cleaved surface topography, and (b) (111)-oriented CZT, with  $n \sim 8 \times 10^{16}$  and resistivity  $\sim 0.5$  ohm-cm, showing a flat surface and evidence of a tip crash due to insufficient sample conductivity.

Our next step was to achieve #2. In general, successful STM requires the presence of a sufficiently conducting surface to enable tunneling of electrons from the tip to the surface (or vice versa). STM of GaAs typically involves material with doping concentration  $> 5 \times 10^{18}/\text{cm}^3$  and resistivity  $< 0.0002$  ohm-cm. However, studies of CdTe have revealed successful STM using material with n-type doping  $\sim 10^{18}/\text{cm}^3$ , corresponding to a resistivity  $< 0.1$  ohm-cm [4].

Recently, M. Chu of Fermionics has been experimenting with lowering the resistivity of his CZT crystals via the indiffusion of In [5]. His latest attempts involved the use of In-doped CdTe substrates, with resistivities  $<0.1$  ohm-cm, which M. Chu fabricated using a recently reported recipe [6]. With these lower resistivity substrates, we expect to easily image MCT-based junctions. For example, the typical doping concentrations of the MCT junctions are  $2-3 \times 10^{18}/\text{cm}^3$ , corresponding to resistivities of 0.0001 and 0.0114 ohm-cm for n- and p-type layers, respectively [7]. These resistivities are expected to be low enough for straightforward STM measurements. This assertion is supported by recent reports of successful STS studies of bulk MCT crystals [8-9].

In order to achieve #3, extreme chamber cleanliness and lack of sample oxidation made possible by UHV integrity, the properties of MCT need to be considered. Since MCT has a very high Hg vapor pressure at  $\sim 70^\circ\text{C}$ , Hg will vaporize from the MCT surface, in appreciable quantities, at  $\sim 70^\circ\text{C}$  [10-12]. This is problematic in systems where the sample cleaving and imaging occur in the same UHV chamber, because any cleaved pieces of MCT on the chamber bottom would release appreciable quantities of Hg during a chamber bakeout (typically  $\sim 150^\circ\text{C}$ ), detrimentally contaminating the STM and chamber. Thus, in order to pursue XSTM studies of MCT, a dedicated system with cleaving capabilities in a separate but interconnected chamber is needed. Therefore, we submitted a proposal to the 2005 DURIP program, in order to obtain this instrumentation. Had the DURIP proposal been awarded, we would have purchased an XSTM system, dedicated to studies of MCT-heterostructures, which has the wide positioning capabilities necessary for timely and successful XSTM measurements (factor #4).

## References

- [1] N. Liu, J. Tersoff, O. Baklenov, A.L. Holmes, and C.K. Shih, *Phys. Rev. Lett.* **84**, 334 (2000).
- [2] A. Lemaitre, G. Patriarche, and F. Glas, *Appl. Phys. Lett.* **85**, 3717 (2004).
- [3] B. Legrand, B. Grandidier, J.P. Nys, D. Stievenard, J.M. Gerard, and V. Thierry-Mieg, *Appl. Phys. Lett.* **73**, 96 (1998).
- [4] L. Seehofer, V. H. Etgens, G. Falkenberg, M. B. Veron, D. Brun, B. Daudin, S. Tatarenko, and R. L. Johnson, *Surface Science* **347**, L55 (1996).
- [5] M. Chu, S. Terterian, D. Ting, C. C. Wang, J. D. Benson, J. H. Dinan, R. B. James, and A. Burger, *J. Electr. Mat.* **32**, 778 (2003).
- [6] V. Lyahovitskaya, L. Kaplan, J. Goswami, and D. Cahen, *J. Cryst. Growth* **197**, 106 (1999).
- [7] R. Zucca, M. Zandian, and J. M. Arias, *J. Vac. Sci. Technol. B* **10**, 1587 (1992).
- [8] G. N. Panin, C. Diaz-Guerra, and J. Piqueras, *Semicond. Sci. Technol.* **13**, 576 (1998).
- [9] G. N. Panin, C. Diaz-Guerra, and J. Piqueras, *Appl. Phys. Lett.* **72**, 2129 (1998).
- [10] R. F. C. Farrow, G. R. Jones, G. M. Williams, P. W. Sullivan, W. J. O. Boyle, and J. T. M. Wotherspoon, *J. Phys. D.: Appl. Phys.* **12**, L117 (1979).
- [11] J.-P. Faurie, *Prog. Crystal Growth and Charact.* **29**, 85 (1994).
- [12] J.H. Dinan, private communication (2004).

## C. Carrier Dynamics Studies on InAs/GaAs QDIPs (Norris)

Quantum dot infrared photodetectors (QDIPs) based on intraband infrared absorption have promised improved performance over their quantum well counterparts by their operation at normal incidence, lower dark current, higher responsivity, and relative temperature insensitivity. These operation principles and improved performance of the detector device are fundamentally determined by carrier dynamics. For example one expects that the discrete nature of electron

levels and the LO phonon energy in the zero-dimensional quantum dots will prevent any first-order interaction unless the electron energy level separation is near the LO phonon energy, i.e. the phonon bottleneck. This should be particularly beneficial for unipolar devices such as the QDIPs, since the photoconductive gain, one of the important figures of merit for photodetectors, is fundamentally determined by the effective electron lifetime. Instead of deducing the life time from detector parameters, our goal is to measure the dynamics directly with ultrafast optical techniques.

Carrier dynamics in the quantum dots, however, are still under some debate after years of intense research. Our group has previously measured capture and intersubband relaxation of electrons in InGaAs/GaAs QDs with pump-probe differential transmission (DT) spectroscopy, and directly observed the phonon bottleneck under very low excitation density. These experiments, however, were carried out in undoped, bipolar systems where electrons and holes are optically injected in pairs into the quantum dot structures. This obscures the independent observation of the electron dynamics and direct studies of unipolar devices. In this MURI program we used a mid-infrared photodetector structure to study the electron dynamics in unipolar quantum dots. Differential transmission spectroscopy with mid-infrared intraband pump and optical interband probe was implemented to measure the electron dynamics directly, with no holes present to affect the relaxation. The mid-infrared pump excited the electron distribution without creating extra electron-hole pairs. The electron relaxation after excitation was measured using white light interband differential transmission. It is therefore well suited for characterizing various electron scattering rates and modeling the operation of the QDIP.

Our measurements on the electron dynamics were mainly based on the In<sub>0.4</sub>Ga<sub>0.6</sub>As multicolor QDIP fabricated in Prof. Bhattacharya's group. The active region of the QDIP consisted of 20 layers of undoped In<sub>0.4</sub>Ga<sub>0.6</sub>As /GaAs self-assembled quantum dots, separated by 50 nm GaAs barriers. The self-assembled InGaAs/GaAs quantum dots were grown on (001) Si-doped n<sup>+</sup> (n=10<sup>19</sup> cm<sup>-3</sup>) GaAs substrate by MBE system. The quantum dots were pyramidal in shape, with a base of 25 nm and height of 6 nm. The areal density of the dots was 4×10<sup>10</sup> cm<sup>-2</sup>. Electrons were ionized from the donor sites in the doped contact layers and resided in the quantum dots confined states to enable infrared absorption. At low temperature, the initial Fermi level established in the conduction band was below and close to the quantum dot 1<sup>st</sup> excited states. The QDIP exhibited spectral responses with three peaks centered at ~3.5, 7.5, and 22 μm, corresponding to the bound-to-continuum, bound-to-wetting-layer, and inter-level transitions, respectively.

We measured the electron dynamics in the QDIP structure using intraband (mid-infrared)-pump interband (optical)-probe differential transmission spectroscopy. The mid-IR pulse was generated using different frequency generation (DFG) and optical parametric amplifier (OPA) pumped by a 250-kHz 800-nm Ti:Sapphire regenerative amplified system. The 2-pass OPA generated a near-IR "signal" pulse, tunable from 1.2 to 1.4 μm, along with an idler at 2.4 to 1.8 μm. The OPA signal and idler pulses were then mixed in AgGaS<sub>2</sub>, producing mid-IR pulses ranging from 2.4 to 7.5 μm. The probe pulse was obtained by focusing the recompressed residual 800 nm laser beam on a sapphire substrate for white-light super-continuum generation. This enabled optical access to different quantum dot transitions across the whole near-band-edge spectrum. The broadband pulse was spectrally selected and dispersion compensated with a prism

pair to ensure each spectral component of the optical pulse arrived at the sample within the temporal resolution of 300fs. The probe pulse was put on a translation stage to vary the time delay between the pulses. The samples were kept in a helium-flow cryostat for temperature-controlled measurements.

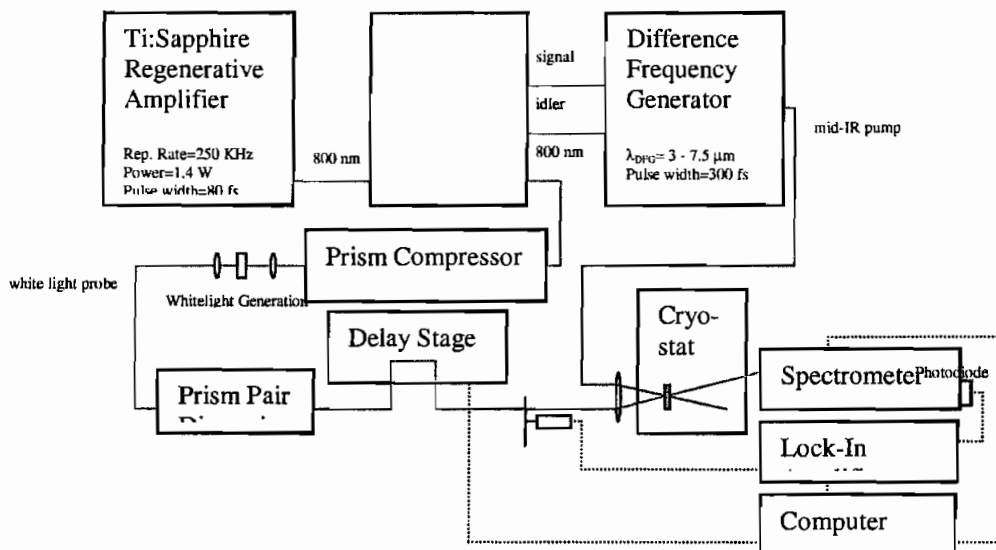


Fig. 1. Experimental setup for mid-IR-pump-optical-probe differential transmission experiments.

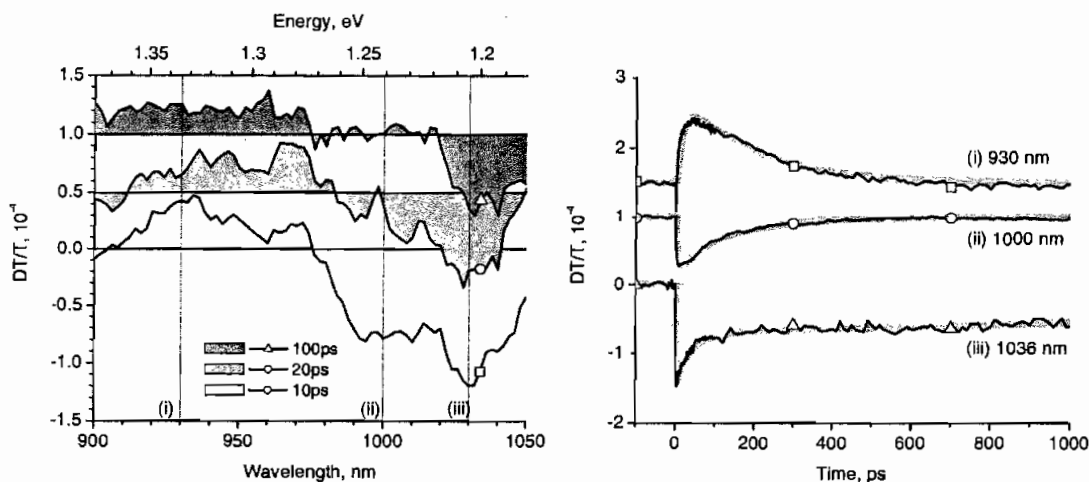


Fig. 2. (a) DT spectra measured at 10 K with 7  $\mu\text{m}$  pump pulse co-linearly polarized as the probe. Spectra of different time delays are shaded with respect to their displaced zero for clarity. (b) DT Time scan at (i) 930, (ii) 1000, and (iii) 1036 nm.

Upon mid-infrared excitation of the quantum dots, electrons were excited out of the quantum dot confined states into the wetting layer and barrier continuum. Fig. 2 shows the DT spectra at several time delays. Rapid re-capture into quantum dot within  $\sim 10$  ps was observed in the excited states from 900 to 970 nm. This temporal feature was attributed to direct capture via the Auger-type electron-electron scattering.

In QDIP devices the electrons density is “high,” i.e. much greater than one electron per dot due to doping, so the capture and intradot relaxation are dominated by Auger-type electron-electron scattering. The direct capture of the electrons in to quantum dot ground state is measured to be dependent of the excited electron density. Fig. 3(a) shows the increasing portion of the direct capture component as the excitation intensity increases. On the other hand, the capture time constant depicted in Fig. 3(b) shows the opposite trend. The results support the idea that the capture process is dominated by Auger-type electron-electron scattering.

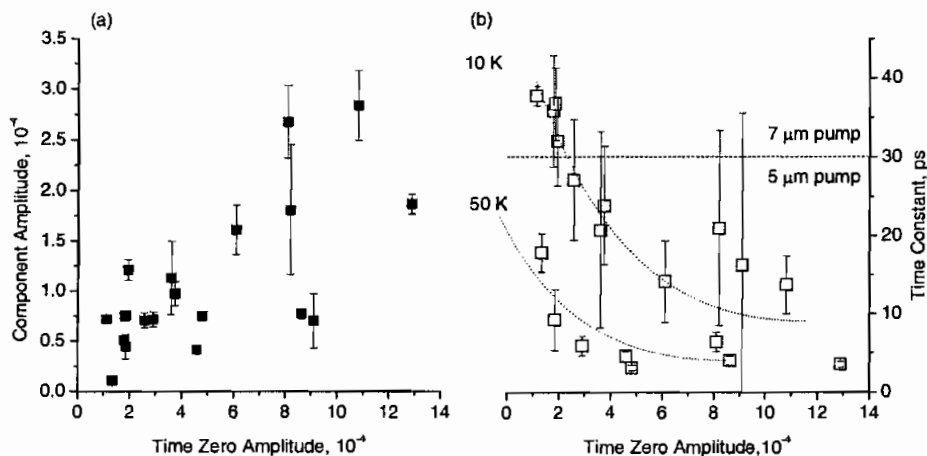


Fig. 3. Fitting results for direct capture (a) component amplitude; (b) time constants. Dash line separates results from different pump wavelength. Dotted line indicates trends for different sample temperature.

Following capture into the excited state, inter-level intradot relaxation from the quantum dot excited state to the ground state was measured to be on the scale of 100 ps. This can be seen in the recovery of the ground state dynamics in Fig. 2(a) and also the complementary decay/recovery between the 930 and 1000 nm DT signals in Fig. 2(b). Because of the high density of the built-in electrons, the phonon bottleneck effect is circumvented by the electron-electron scattering.

Bimodal dynamics were observed and attributed to fluctuations in the quantum dot sizes. In Fig. 2(b), nanosecond-scale recovery dynamics were observed for the deeper ground states of larger dots centered at 1030 nm (trace iii). This was attributed to the loss of electrons in the active region due to band-bending and built-in voltage drift. In the absence of the electron-hole scattering channel, both relaxation processes in unipolar quantum dots structure have time scales longer than that observed in bipolar systems. This enables the capture and inter-sublevel dynamics to be separately observed. The direct capture of the electrons due to Auger-type scattering was measured.

We also developed an ensemble Monte Carlo model to simulate the electron dynamics in the QDIP quantum dot structure. The model showed the phonon bottleneck effect was largely bypassed when the built-in electron density is high and the inter-sublevel relaxation was dominated by the Auger-type scattering. The simulation and experimental results were in good qualitative agreement.

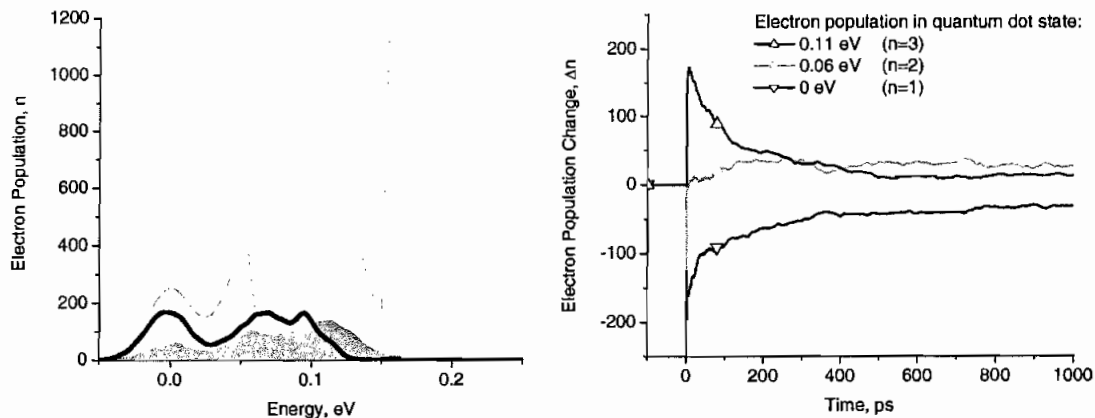


Fig. 4. Monte Carlo simulation (a) electron distribution at two different time delay: 10 ps (gray shaded area) and 100 ps (thick black line). The total density of state of the modeled quantum dots is also shown (thin gray line); (b) Time scan of the electron population at different energies of the quantum dot ensemble model. Complementary dynamics can be seen between the  $n=3$  and  $n=1$  states with the intermediate  $n=2$  state relatively unchanged.

In terms of QDIP device operation, our results suggest that even in the absence of the phonon bottleneck, the electron dynamics are intrinsically slower than in bipolar devices. For real-world detection applications of QDIP's, the excitation is low compared to the coherent laser pulse used in our experiments. The portion of direct capture due to Auger-type scattering in the continuum is thus expected to be small and sequential relaxation through the wetting layer and quantum dot excited states are more likely to occur. The  $\sim 100$  ps inter-sublevel relaxation time enables the electrons in the excited states to tunnel out of the triangular barrier under bias and be collected as photocurrent despite the rapid capture rate.

We have presented a comprehensive picture of electron dynamics in the unipolar quantum dot structure, which directly reflects the operation of an actual QDIP device. These results helped to explain the microscopic operation of the quantum dot infrared photodetector. The measured scattering rates can be used for further theoretical works on the QDIP under biasing conditions, and may also provide basic outline of device design for future applications.

#### D. Quantum Dot Intersublevel Photodetectors (Bhattacharya)

##### Introduction

##### Background

Infrared (IR) photodetectors are used in a range of imaging applications, such as medical diagnosis, law enforcement, environmental monitoring, space science, and industrial equipment diagnosis. IR light is useful for these applications for two main reasons. First of all, the

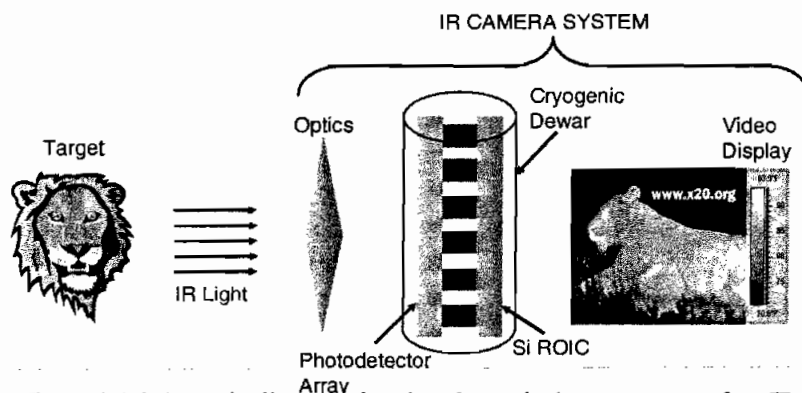


Figure 1.1 Schematic diagram showing the typical components of an IR camera system.

blackbody radiant emittance peaks in the IR wavelength range for temperatures greater than room temperature (300 K). Secondly, due to its longer wavelength, IR light does not have the same scattering and absorption characteristics as visible light. Therefore, transparent windows in the atmosphere permit the transmission of IR light.

The typical components of an IR camera system, shown schematically in Fig. 1.1, include: optics for light collection, a focal plane array for detection and signal processing, a cooling system for photodetector focal plane arrays, and electronics for the digital display of IR images. The focal plane array (FPA), a hybrid, integrated circuit, comprises a detector array and a silicon read-out circuit, and it is positioned at the focal point of the light-collecting optics. The detector array converts incident IR light energy to electrical energy, while the silicon read-out circuit collects the detected signal (current or voltage) and performs initial, digital signal processing. A significant reduction in the cost of IR camera systems is possible if the traditional FPA cooling systems, such as liquid-nitrogen dewars, are replaced by thermo-electric coolers. Such a design change requires the development of an IR photodetector that operates at elevated temperatures ( $\geq 120\text{K}$ ).

A promising nanostructure for high-operating temperature (HOT) IR photodetection is the quantum dot, which offers several advantages for device operation. Quantum dot infrared photodetectors (QDIPs) benefit from long electron lifetime for increased detector efficiency, low dark current for HOT IR photodetection ( $\geq 150\text{K}$ ), normal-incidence detection for simplified device fabrication, and several tuning parameters for controlling IR response as a result of three-dimensional quantum confinement of the active region. Successful demonstrations of low dark current [1, 2], multi-spectral response [3, 4], high-detectivity [5], HOT photodetection [6, 7], and IR imaging [8, 9] in QDIPs have helped establish this technology as a viable alternative to microbolometers and HgCdTe photodiodes for imaging applications in the mid-IR. The measured device performance of In(Ga,Al)As/(Ga,Al)As QDIPs developed during this project and operating in the mid-IR [7, 10] is shown in Table I. Commercially-available IR detector technologies (cooled and un-cooled) [11, 12] are compared in Table II, including microbolometers and low-bandgap photodiodes (HgCdTe and InSb). It is important to note that InAs/GaAs QDIPs (at 150K) have already demonstrated performance (detectivity) comparable to HgCdTe photodiodes (at 77K) in the mid-IR.

**Table I. State-of-the-art QDIP Figures of Merit Obtained in This Work**

QDIP Design	Operating Temperature	Operating Bias	Figure of Merit	Value
15 nm SL DWELL QDIP	78 K	-1.5 V	$\eta_{\text{conv}}$	70 %
			$R_{\text{peak}}$	2.5 A/W
			$J_{\text{dark}}$	$1.83 \times 10^{-2} \text{ A/cm}^2$
70-layer InAs/GaAs QDIP (ARL)	175 K	2.0 V	$\eta_{\text{conv}}$	3.2 %
			$R_{\text{peak}}$	0.120 A/W
			$D^*_{\text{peak}}$	$4.15 \times 10^7 \text{ cmHz}^{1/2}/\text{W}$
			$J_{\text{dark}}$	$5.80 \times 10^{-5} \text{ A/cm}^2$
70-layer InAs/GaAs QDIP (NASA JPL)	150 K	2.0 V	$R_{\text{peak}}$	0.201 A/W
			$D^*_{\text{peak}}$	$3.7 \times 10^{10} \text{ cmHz}^{1/2}/\text{W}$
			NEAT	50 mK
			RT-QDIP	300K

**Table II. Commercially-Available IR Detector Technologies**

	Un-cooled IR Detectors	Cooled IR Detectors	
<b>DRS Technologies, Inc.</b>	<b>U3000 Un-cooled Microbolometer IR Sensor</b>	<b>Missile Seeker IRFPA Module</b>	
<b>Sensor Material</b>	Vanadium Oxide	HgCdTe	
<b>Spectral Range</b>	Long-IR	Mid-IR	Long-IR
<b>Array Size</b>	320x240	480x640	
<b>Pixel Size</b>	51 $\mu$ m x 51 $\mu$ m	25 $\mu$ m x 25 $\mu$ m	
<b>Operating Temperature</b>	300 K	77 K	
<b>Sensitivity (NEDT, D*)</b>	40-100 mK	4x10 <sup>10</sup> Jones	3.5x10 <sup>9</sup> Jones
<b>Operability</b>	> 98%	> 98%	
<b>Dynamic Range</b>	> 66 dB	74 dB	
<b>Frame Rate</b>	60 Hz	60 Hz	
<b>Indigo Systems, Inc.</b>	<b>ThermoVision Micron Camera</b>	<b>Phoenix Camera</b>	
<b>Sensor Material</b>	Vanadium Oxide	InSb	GaAs QWIP
<b>Spectral Range</b>	Long-IR (7.5-13.5 $\mu$ m)	Mid-IR (1.5-5 $\mu$ m)	Long-IR (8.0-9.2 $\mu$ m)
<b>Array Size</b>	160x120	320x256	
<b>Pixel Size</b>	51 $\mu$ m x 51 $\mu$ m	30 $\mu$ m x 30 $\mu$ m	
<b>Operating Temperature</b>	300 K	LN <sub>2</sub>	Stirling Cycle
<b>Sensitivity (NEDT, D*)</b>	≤ 85 mK	< 25 mK	< 35 mK
<b>Operability</b>	≥ 98%	> 99.5%	
<b>Dynamic Range</b>	14 bits (80 dB)	14 bits (80 dB)	
<b>Frame Rate</b>	30 Hz	345 Hz	

*QDIP – Principle of operation and differences with other infrared detectors*

As stated earlier, the QDIP is an intersubband detector, like the QWIP, and therefore differs in its principle of operation and materials requirements from interband (MCT or InSb) detectors. The three-dimensional (3-D) confinement allows normal incidence. The large density of states and the long intersubband relaxation times promise large responsivity.

As will be evident in the next section, the effective carrier lifetime in QDIPs is ~ 100 ps-1ns, whereas that in MCT detectors is ~ tens of milliseconds. If one superficially examines dark current in p-n diodes, the long lifetime in MCT detectors compared to that in QDIPs may appear to translate to lower dark current in MCT detectors. However, a more careful examination shows that is not a correct comparison. In interband detectors, the photocurrent and responsivity depend on the lifetime. The dark current in these devices is primarily a diffusive current, and hence depends inversely on the carrier lifetime. In a QDIP, the photocurrent and responsivity depend directly on the electron lifetime. However, the dark current does not depend on the carrier lifetime; instead it is determined primarily by thermionic emission and field-assisted tunneling rates. *As a consequence, it is important to understand that the parameter  $R_oA$ , a material constant depending on minority carrier parameters and which is a useful measure for the performance of junction detectors (MCT and InSb), is not strictly applicable to quantum intersubband photoconductive detectors (QWIPs and QDIPs).* One can extrapolate a resistance to dark current flow from the I-V characteristics, but the product of the resistance and the device area is not a constant. This resistance depends on device geometry. *A more meaningful parameter for comparison is the dark current density.*

Unlike p-n diodes or QWIP structures, the QDIP structure *does not* have a continuous density of states. The density of states has a form shown in Fig. 1.2.1, which represents broadened  $\delta$ -functions. As the temperature is raised, carrier average energies are, overall, lower than those in QWIP or p-n diode structures. Even though the density of states in QDIPs is discrete for low energy states, it becomes like 3-D continuous states for high energies. As a result, at temperatures above  $\sim 150$  K, the electron occupation is dominated by the excited states. Therefore, in the conventional QDIP, dark current benefits are difficult to sustain at temperatures above 150 K. The reduction of dark current at high temperatures of operation is one of the bigger challenges in the design of QDIPs.

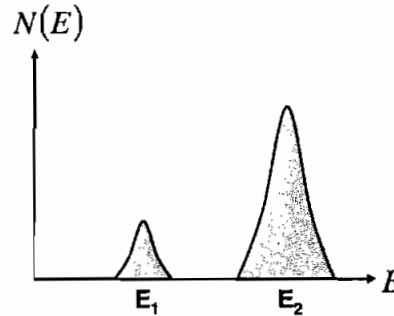


Figure 1.2.1 Density of states in quantum dots.

### Background status of QDIPs in 2000 & reasons for poor performance

Since the first demonstration and characterization of QDIPs in 1999 at the University of Michigan[13], several research groups around the world have investigated these devices, seeking to push the boundaries of state-of-the-art performance. At the beginning of this project, QDIPs had surpassed other detectors in terms of low dark current, thereby exhibiting the potential for high-temperature operation. However, the responsivity and detectivity did not yet exhibit the predicted improvements, particularly at elevated temperatures and in multiple wavelength ranges. Several challenges contributed to this lower-than-expected performance in the past, and they have been investigated during the course of this project.

First, the design and epitaxial growth of QD heterostructures are the most important issues related to obtaining state-of-the-art performance in QDIPs. While the Stranski-Krastanow (S-K) growth mode is well-established, having been reported first in 1938, there is still much to learn about the controlled growth of self-assembled QDs, particularly those with device-quality electrical and optical properties. One of the most significant consequences of the S-K growth mode is the random fluctuation of dot size and dopant incorporation. These non-uniformities lead to an inherently large full-width, half-maximum (FWHM) linewidth ( $\sim 50$ meV) for transitions in a QD ensemble. Such inhomogeneous linewidth broadening adversely affects the absorption coefficient in the active region and has a deleterious effect on QDIP performance. For example, fluctuations in dot size make it difficult to control the spacing between discrete energy levels within QDs, affecting the spectral response of QDIPs; and fluctuations in dopant incorporation affect both the dark current density and the spectral response in QDIPs. In addition, not only is the absorption coefficient reduced due to inhomogeneity, but the total absorption is low since the S-K growth mode leads to the build-up of strain for repeated dot layers. As a result, the absorption region is usually limited for normal-incidence radiation since the QD height is typically less than 10 nm.

Through the CENTROID MURI significant contributions have been made to address these issues, including: i) exploration of the fundamental limitations of QDIP performance, ii) development of MBE growth techniques for increased IR absorption in QDs, iii) development of models for dark current and responsivity that account explicitly for QD ensemble properties, and iv) demonstration of state-of-the-art QDIP performance in discrete devices. As a result, QDIP

operating temperature for devices operating in the 3-5  $\mu\text{m}$  wavelength range has increased from 40 K to 175 K for normal-incidence devices with 70 QD layers. Further, these devices exhibit the requisite performance for integration with silicon read-out circuits. It is important to note that rapid progress has been made towards increasing operating temperature and improving device performance in the 3-5  $\mu\text{m}$  wavelength range. However, accomplishing comparable operating temperature and device performance improvements at longer wavelengths has proven challenging. This is especially relevant for two-color detection in a single device heterostructure for high-resolution imaging in which the LWIR response in the 8-14  $\mu\text{m}$  range provides the limiting factor for operating temperature. However, a new design developed during the course of this project, the resonant-tunneling (RT) QDIP, has enabled multi-spectral IR photoresponse (including 8-14  $\mu\text{m}$  range) at room temperature.

### **Work done in this project**

#### *Objectives in this program: High temperature detectors*

Due to the three dimensional carrier confinement in the quantum dots, the dark current is expected to be lower than other IR detectors. Experimentally, it is found that, in general, dark currents are significantly lower than those in QWIPs due to the higher thermionic emission rates in the latter. As will be evident, in the tunnel QDIP (T-QDIP), the dark current is further reduced. Our goal has therefore been to demonstrate mid IR and FIR detectors that can be operated with acceptable characteristics at high temperatures ( $\geq 150\text{K}$ ). In what follows, highlights of results obtained from the different devices are described, including those from the novel tunnel QDIPs.

#### *MBE of QDs for QDIPs*

InAs/GaAs QDs are grown on either semi-insulating or n+ GaAs substrates with a (100) orientation using a solid-source Varian Gen-II MBE system with an uncracked  $\text{As}_4$  source. The  $\text{As}_4$  overpressure in the growth chamber is maintained at  $\sim 7 \times 10^{-6}$ - $1 \times 10^{-5}$  Torr. The lattice mismatch at the interface of an InAs epi-layer and a GaAs substrate is  $\sim 7\%$ . Therefore, the Stranski-Krastanow growth mode for the self-assembly of 3-D islands will occur under appropriate growth conditions. The typical InAs growth rate is 0.1 ML/sec, and the GaAs substrate temperature is usually cooled to 500  $^\circ\text{C}$ . The wetting layer thickness in the InAs/GaAs QD system is 1.7 monolayers (ML), where 1 ML  $\sim 2.83 \text{ \AA}$  for III-V materials. The transition from the 2-D wetting layer to 3-D islands is observed using in-situ reflection high-energy electron diffraction. InAs overgrowth occurs for 2-5 seconds to provide enough InAs charge (2.2 ML) for pyramidal QDs, and a 30 second growth-interrupt pause is used to allow the complete formation of QDs. After this pause, an intrinsic GaAs cap layer ( $\sim 25$ -60 nm) is grown on top of the InAs QDs, thereby completing the QD potential barrier. This sequence of growth is repeated to achieve a specified number of QD layers. Typically, the QDs are directly-doped with silicon in order to provide free electrons for photoexcitation, and the carrier concentration ranges from  $0.5$ - $1 \times 10^{18} \text{ cm}^{-3}$ . The doping density provides two electrons per dot for typical InAs/GaAs QD densities. During direct-doping, an effort is made to incorporate dopants in the QDs only and not in the wetting layer. Therefore, the silicon shutter is opened after the completion of the wetting layer, and it remains open during the subsequent dot overgrowth and growth-interrupt pause.

(a) Growth of large InAs/GaAs quantum dot stacks

IR detection requires a large absorption volume to efficiently convert photons to electrons. Therefore, the small absorption region in QDIPs should be increased for better quantum efficiency. The most straightforward approach to increase the absorption region is to grow a large number of QD layers in the detector active region. However, the number of QD layers is limited by the ability to incorporate strain coherently in the heterostructure without generating misfit dislocations. In this MBE study, the growth technique for obtaining 70-layers of uncoupled QD layers was determined. The GaAs barrier region thickness required to minimize the effect of the strain field from one dot layer to the next was investigated through transmission electron microscopy (TEM) images. In addition, PL measurements were conducted to demonstrate the optical quality of these large QD stacks.

The most important parameter that had to be calibrated to increase the number of QD layers was the GaAs barrier thickness. As shown in Fig. 2 (a), for a 10-layer InAs/GaAs QD stack, a 25 nm barrier was sufficient to prevent the propagation of misfit dislocations throughout the heterostructure. However, when the number of dot layers was increased to 30, using the same 25 nm GaAs barrier between QD layers, a high dislocation density was present in the material, as shown in Fig. 2(b). In order to determine the required GaAs barrier thickness to prevent such dislocation propagation, a 30-layer QD stack was grown using 50 nm GaAs barrier layers. This growth recipe resulted in 30 QD layers with no observed misfit dislocations, as shown in Figure 2. Thus, having obtained an appropriate GaAs barrier thickness for 30 QD layers, the number of QD layers was increased to 70. The resulting TEM image, shown in Fig 2(d), demonstrated that the dislocation density was minimal in the 70-layer QD stack.

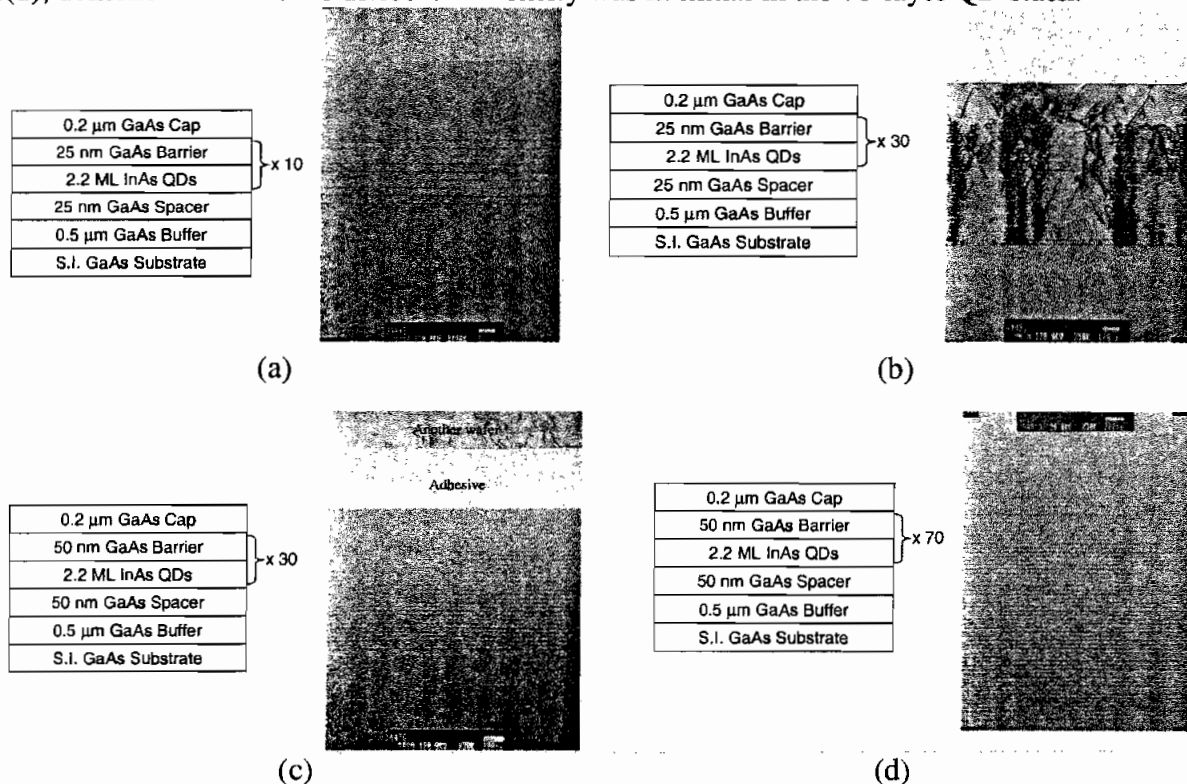


Figure 2. Schematic diagram and TEM image of (a) 10-layer InAs/GaAs QD stack with 25 nm GaAs barrier layers, (b) 30-layer InAs/GaAs QD stack with 25 nm GaAs barrier layers, (c) 30-layer InAs/GaAs QD stack separated by 50 nm GaAs barrier layers, and (d) 70-layer InAs/GaAs QD stack separated by 50 nm GaAs spacers.

Thus, the large GaAs barrier thickness (50 nm) is essential to obtaining large QD stacks for increased absorption of incident IR light. In addition, such barrier layers help reduce thermionic emission and tunneling contributions to the dark current[14]. The excellent optical quality of the 70-layer QD stack was demonstrated by very strong photoluminescence (PL) spectra at  $T = 20$  K and 300 K (using a pump power density of  $\sim 7.64$  W/cm<sup>2</sup>). At  $T = 20$  K, the strong PL peak was centered at 968 nm (1.28 eV) with a PL FWHM linewidth of 62 meV. The PL spectrum at room temperature, while less intense than that obtained at 20 K, was still very strong with a peak wavelength of 1062 nm (1.17 eV) and a PL FWHM linewidth of 93.6 meV. The variation of the PL FWHM linewidth ( $T = 20$  K) as a function of the number of QD layers in the heterostructure is shown in Fig. 3. The linewidth remained fairly constant ( $\sim 60$  meV) as the number of QD layers was increased from 10 to 70. This indicates that the overall size distribution of the self-assembled QDs, which determines the inhomogeneous broadening, was largely unaffected by the number of dot layers in the heterostructure.

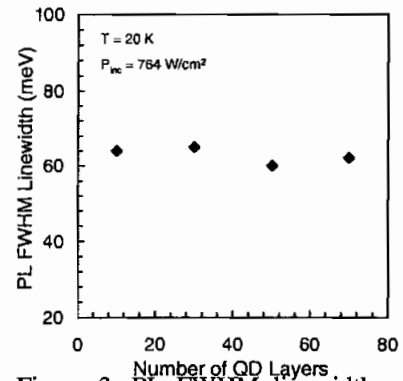


Figure 3. PL FWHM linewidth as a function of the number of InAs/GaAs QD layers at  $T = 20$  K

(b) Growth of laterally-coupled quantum dots using aluminum-bearing compounds

By improving the size and shape uniformity of QD ensembles, the Gaussian linewidth representing inhomogeneous broadening should decrease, thereby increasing the absorption coefficient and improving the device performance of QDIPs. One way to circumvent the QD uniformity issue is to induce lateral coupling of QDs. Laterally-coupled quantum dots (LCQDs) nucleate with a nearest neighbor distance of approximately 10 nm in the plane perpendicular to the growth direction. This proximity results in the formation of minibands and a reduction in the PL FWHM linewidth, approaching the thermal broadening limit ( $\sim 6$  meV at 70 K). In addition, the large QD surface density required to induce lateral coupling also improves IR absorption in QDIPs.

Various techniques have been used to invoke lateral coupling, including reduced substrate temperatures during MBE[15], alternate supply growth techniques[16], strain patterning of QDs either through vertically-coupled QDs[17, 18] or buried stressor QDs[19], and the incorporation of aluminum in the QD[20]. Aluminum incorporation in either the QD or barrier material during MBE growth was used for inducing LCQDs in the material study discussed in this section. Furthermore, the substrate temperature during the MBE growth of a particular InAlAs QD composition was reduced to examine the effect of this technique for inducing lateral coupling. Atomic force microscopy (AFM) images and PL measurements were examined to determine the extent of lateral coupling achieved in each case.

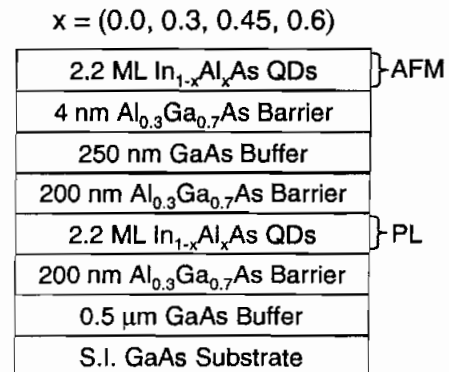


Figure 4. Schematic diagram of the In<sub>1-x</sub>Al<sub>x</sub>As/Al<sub>0.3</sub>Ga<sub>0.7</sub>As QD heterostructures investigated for lateral coupling.

In the first study, the lateral coupling effect of incorporating increasing Al content in InAs QDs was ascertained. The incorporation of Al in the QD active region is expected to increase the lateral coupling of the QDs due to the low mobility of AlAs, which is approximately two orders of magnitude less than that for InAs. This lower mobility prevents adatoms from moving quickly across the epi-layer surface during epitaxial growth, allowing QDs to nucleate more densely. The heterostructure schematic diagram for the  $\text{In}_{1-x}\text{Al}_x\text{As}/\text{Al}_{0.3}\text{Ga}_{0.7}\text{As}$  QD samples used in this study ( $x = 0.0, 0.3, 0.45, \text{ and } 0.6$ ) are shown in Fig. 4. The corresponding PL peak energies and FWHM linewidths for the  $\text{In}_{1-x}\text{Al}_x\text{As}/\text{Al}_{0.3}\text{Ga}_{0.7}\text{As}$  QD samples are listed in Table III. In terms of the PL peak energy, a blue-shift was observed corresponding to increasing Al content. However, it is important to note that such QDs can still be used to detect IR light since the intraband transition within the QD can be engineered. As for the PL FWHM linewidth, there was significant linewidth narrowing due to the presence of Al, again indicating that lateral coupling occurred in these  $\text{In}_{1-x}\text{Al}_x\text{As}/\text{Al}_{0.3}\text{Ga}_{0.7}\text{As}$  QDs. The narrowest FWHM linewidth was obtained for the  $\text{In}_{0.55}\text{Al}_{0.45}\text{As}$  QD system (35.5 meV).

Table III. PL Peak Energy and FWHM Linewidth for  $\text{In}_{1-x}\text{Al}_x\text{As}/\text{Al}_{0.3}\text{Ga}_{0.7}\text{As}$  QDs.

$\text{In}_{1-x}\text{Al}_x\text{As}/\text{Al}_{0.3}\text{Ga}_{0.7}\text{As}$ QDs	PL Peak Energy (eV)	PL FWHM Linewidth (meV)
$x = 0.0$	1.323	244
$x = 0.3$	1.716	59.0
$x = 0.45$	1.840	35.5
$x = 0.6$	1.832	39.2

Since the  $\text{In}_{0.55}\text{Al}_{0.45}\text{As}/\text{Al}_{0.3}\text{Ga}_{0.7}\text{As}$  QDs yielded the best results in terms of the PL FWHM linewidth (and thus the extent of lateral coupling), this QD system was used to study the effect of reduced substrate growth temperatures on lateral coupling. Reduced substrate temperatures should increase lateral coupling of QDs since adatoms have less thermal energy, again nucleating more densely on the epi-layer surface. In this second experiment, the QD composition remained constant while the substrate temperature during MBE growth of the QDs was reduced.

Figure 5 (a)-(c) show the AFM images obtained for  $T_{\text{sub}} = 530^\circ\text{C}, 515^\circ\text{C}, \text{ and } 500^\circ\text{C}$ , respectively. It is evident that as the substrate temperature was reduced, the QDs became denser and the QD size was reduced, again indicating that lateral coupling occurred. The corresponding PL peak energies and FWHM linewidths for the  $\text{In}_{0.55}\text{Al}_{0.45}\text{As}/\text{Al}_{0.3}\text{Ga}_{0.7}\text{As}$  QDs grown at different substrate temperatures are listed in Table IV. As the substrate temperature was reduced, the PL peak energy was blue-shifted, most likely due to the smaller size of the QDs, which increased the ground state energy level within the QDs. The PL FWHM linewidths did not demonstrate any consistent trend with respect to the substrate temperature. However, this was probably due to the Ostwald ripening of smaller QDs, which offset the lateral coupling induced in the QDs by the low-temperature growth.

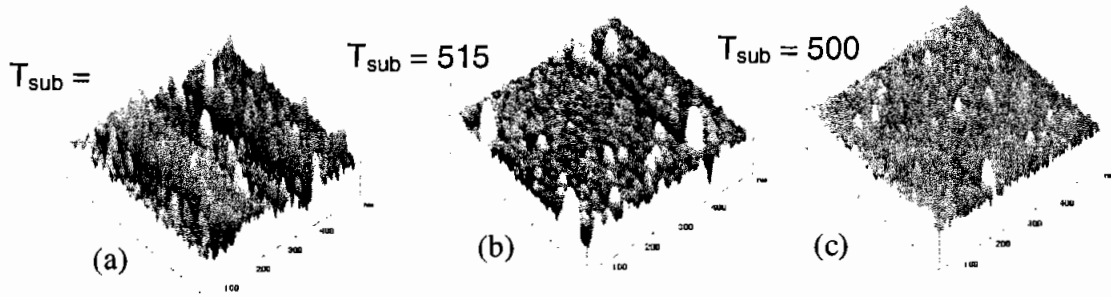


Figure 5. AFM images of  $\text{In}_{0.55}\text{Al}_{0.45}\text{As}/\text{Al}_{0.3}\text{Ga}_{0.7}\text{As}$  QDs, where (a)  $T_{\text{sub}} = 530$  °C, (b)  $T_{\text{sub}} = 515$  °C, and (c)  $T_{\text{sub}} = 500$  °C.

Table IV. PL Peak Energy and FWHM Linewidth for  $\text{In}_{0.55}\text{Al}_{0.45}\text{As}/\text{Al}_{0.3}\text{Ga}_{0.7}\text{As}$  QDs with Varying Substrate Temperature.

$\text{In}_{0.55}\text{Al}_{0.45}\text{As}/\text{Al}_{0.3}\text{Ga}_{0.7}\text{As}$ QDs	PL Peak Energy (eV)	PL FWHM Linewidth (meV)
$T_{\text{sub}} = 530$ °C	1.522	89.5
$T_{\text{sub}} = 515$ °C	1.548	103
$T_{\text{sub}} = 500$ °C	1.586	90.0

(c) Study of doping incorporation in  $\text{Al}_{0.3}\text{Ga}_{0.7}\text{As}$  barrier QDIPs

Due to the random S-K growth mode for the self-assembly of InAs/GaAs QDs, dopant incorporation is also a random process. The ability to better control dopant incorporation in QDs is desirable for two reasons. First, the QD doping density significantly influences the QDIP dark current since electrons occupying QD excited states can escape more easily by thermionic emission.

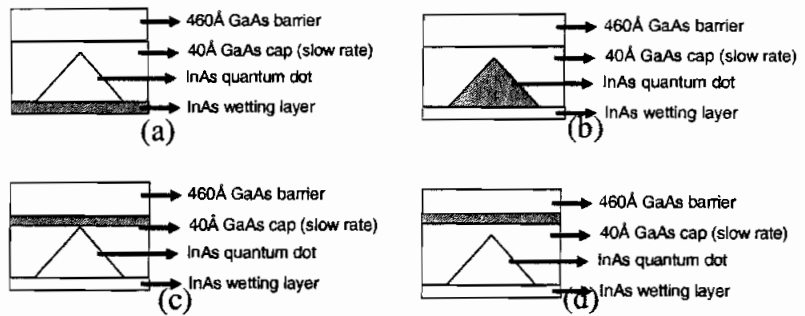


Figure 6. Schematic diagrams of the doping techniques used during MBE growth of the InAs/GaAs QD active region: (a) doped InAs wetting layer, (b) doped InAs QD, (c) doped GaAs cap layer, and (d) doped GaAs barrier layer.

Second, by precisely controlling the electron occupation number of QDs, B-B transitions in the LWIR could be achieved more easily in QDIPs. Therefore, in an effort to better control the random dopant incorporation in QDs, InAs/GaAs QDIPs with n-type dopant deposition occurring in different locations were grown, fabricated, and characterized. As illustrated schematically in Fig. 6, four different doping techniques were used during the growth of the 30-layer QDIPs. First, silicon modulation-doping occurred during deposition of the InAs wetting layer, represented by the shaded layer in Fig. 6(a). Second, as shown schematically in Fig. 6(b), direct silicon-doping occurred during QD formation. In the third doping technique, shown schematically in Fig. 6(c), modulation-doping of silicon occurred during deposition of the GaAs

cap layer, grown at a slow rate after the QDs. Finally, modulation-doping of silicon occurred during the fast deposition of the GaAs barrier layer, after the GaAs cap layer was complete, as shown schematically in Figure(d).

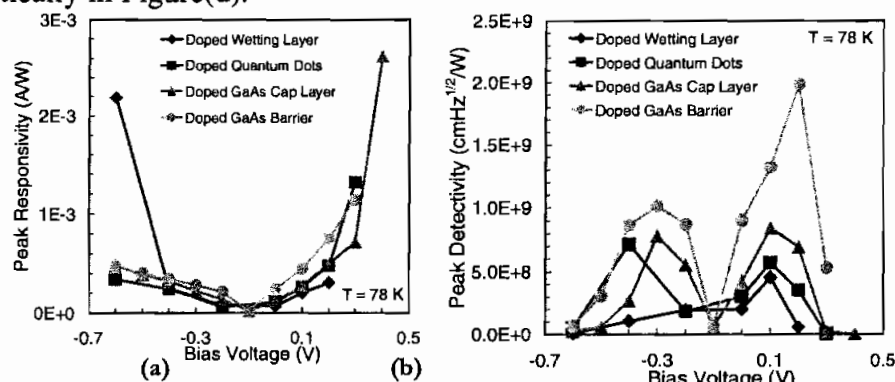


Figure 7. Measured (a) peak responsivity and (b) peak specific detectivity as functions of bias voltage at T = 78 K in the 30-layer, Al<sub>0.3</sub>Ga<sub>0.7</sub>As barrier QDIP subject to different doping techniques.

Detector characteristics were measured in the four different samples at a device temperature of 78 K. The data presented here is limited to the low-bias performance of the QDIPs. The spectral response peak wavelengths for all four devices were in the MWIR range. Fig. 7(a) shows the measured peak responsivity in the QDIPs subject to different doping techniques. For both forward- and reverse-bias, modulation-doping in the GaAs barrier yielded the best performance. The peak specific detectivity is shown in Fig. 7(b) as a function of bias voltage. For both forward- and reverse-bias voltages, the modulation-doped GaAs barrier QDIP demonstrated the largest detectivity.

Additional insight into the device operation of these QDIPs subject to different doping techniques can be derived from considering the measured signal and noise currents, shown in Fig. 8(a) and (b), respectively. In terms of the signal current, the doped GaAs barrier QDIP demonstrated the largest value for all bias voltages (except zero bias).

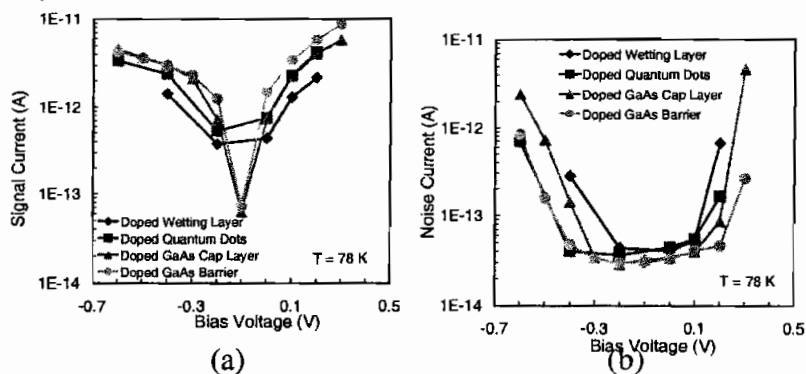


Figure 8. Measured (a) signal current and (b) noise current as functions of bias voltage at T = 78 K in the 30-layer, Al<sub>0.3</sub>Ga<sub>0.7</sub>As barrier QDIP.

Perhaps, more importantly, the noise current in the doped GaAs barrier QDIP maintained low values for a larger bias range. This is most likely due to reduced ion impurity scattering since the donor atoms and free carriers are separated spatially through modulation-doping, leading to reduced generation-recombination noise in the QD active region. Thus, this doping study indicates that modulation-doping in the GaAs barrier of the InAs/GaAs QD active region improves QDIP performance, especially in terms of the measured noise current and detectivity.

### Detector Characterization

The various devices have been characterized at the U.S. Army Research Laboratory, Adelphi, MD (S. Kennerley), the NASA Jet Propulsion Laboratory, Pasadena, CA (S. Gunapala) and Georgia State University, Atlanta, GA (A.G.U. Perera). While the details of the measurements vary slightly at the different locations, the basic principles are the same. Graduate students and post-doctoral fellows have spent time at these laboratories and have conducted the experiments. We thank our collaborators at these laboratories for their interest and help.

Devices are fabricated by a three-step process consisting of standard photolithography, metallization, and wet-etch techniques: 1) evaporation of the top metal ring contact; 2) an approximate 2-4  $\mu\text{m}$  etch to define the circular mesa active region; and 3) evaporation of the bottom metal ring contact. The 100-300  $\mu\text{m}$  radius detectors are then annealed at 400  $^{\circ}\text{C}$  for one minute to form ohmic contacts. The schematics of a mesa-etched QDIP and a SEM micrography of the same are shown in Fig. 3.3.1

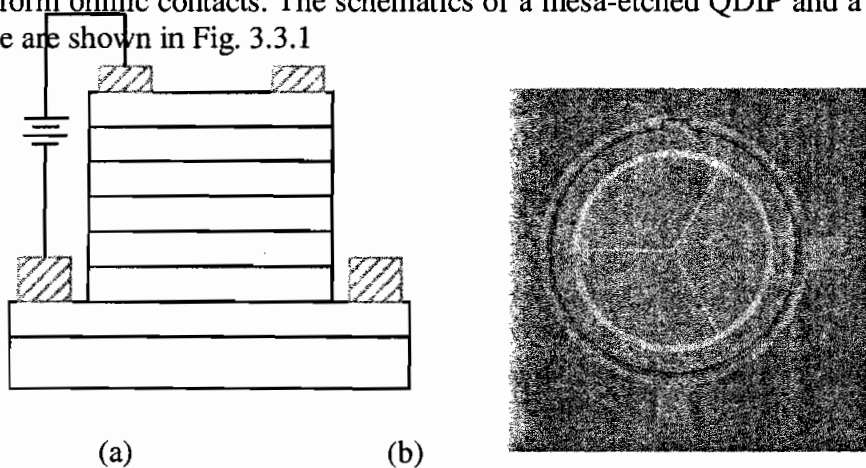


Figure 3.3.1(a) Schematics of a mesa-etched QDIP and (b) microscope image of a single QDIP device

The devices are mounted on chip carriers with silver epoxy and individual devices are wire bonded to separate leads of the carriers. These are then mounted in a variable temperature liquid He cryostat. The dark current-voltage (I-V) characteristics are measured with a Hewlett-Packard 4145 Semiconductor Parameter Analyzer. Measurements are made for both bias polarities, where a positive bias denotes a positive polarity of the top contact. The temperature dependent dark current data of a mid IR QDIP and a 6 $\mu\text{m}$  tunnel QDIP are shown in Figs. 3.3.2(a) and (b), respectively. *These dark current  $\sim 1\text{A}/\text{cm}^2$  at 300K, represent the lowest values in any infrared detector.*

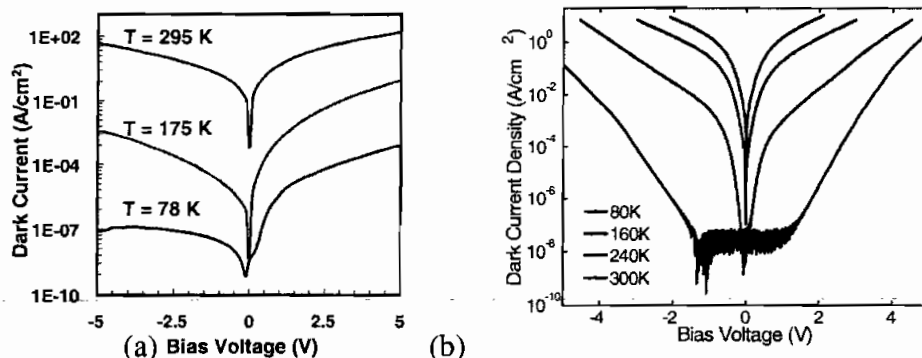


Figure 3.3.1 Dark current density of (a) MID-IR QDIP and (b) a T-QDIP

The spectral response and calibrated responsivity spectra of the devices are measured, under normal incidence, with a global broadband source. The spectral response of the device under test and a composite bolometer, with a known sensitivity, are measured with a S2000 Fourier Transform Infrared Spectrometer (FTIR). The two spectra are obtained concurrently with the same combination of optical window, beamsplitter and filters, so that the optical path is identical. The device spectrum ( $I_d$ ) is then divided by the bolometer spectrum ( $I_b$ ) and multiplied by the bolometer sensitivity ( $S_0$ ) to obtain the voltage responsivity of the device:

$$R(V/W) = GI_d S_0 / I_b \quad (3.3.1)$$

Here  $G$  is a geometrical factor which corrects for differences in the radiation-incident-area of the detector and the bolometer. To obtain the current responsivity, the voltage responsivity is divided by the effective resistance. As the detector and the load resistor act as a voltage divider the effective resistance  $R_e$  is the parallel resistance of the load  $R_l$  and the detector dynamic resistance  $R_d (= dV/dI)$ , yielding  $R_e = R_l R_d / (R_l + R_d)$ . The final current responsivity is given by

$$R(A/W) = GI_d S_0 (R_l + R_d) / (R_l R_d I_b) \quad (3.3.2)$$

At ARL, the photocurrent and responsivity are measured by direct photon counting.

The specific detectivity ( $D^*$ ) of the devices at different temperatures and applied biases is obtained from the measured peak responsivity  $R_p$  and noise density spectra,  $S_i$ . The latter are measured with a dual channel Fast Fourier Transform (FFT) signal analyzer and a low noise pre-amplifier. A thick copper plate is used as the radiation block to provide the dark conditions for the measurements. The value of  $D^*$  is calculated from

$$D^* = R_p A^{1/2} / S_i^{1/2} \quad [\text{cm}\cdot\text{Hz}^{1/2}/\text{W}^{-1}] \quad (3.3.3)$$

where  $A$  is the illuminated area of the detector.

Figure 3.3.3 shows a FFT spectra measured for a mid-IR QDIP at a temperature of 100 K and a bias range from  $-1.5$  V to  $0.35$  V at ARL. As the bias voltages approach zero, the noise floor becomes low and nearly flat above 500 Hz. However, as the bias increases, either negatively or positively, the noise floor also increases, thereby decreasing the signal to noise ratio. Finally, at  $0.35$  V, the noise in the detector has increased so much that the intersubband signal is swamped and no peak is visible in the FFT spectrum. A flat-band noise spectrum is desirable because it indicates that the dominant noise mechanism is generation-recombination (GR) noise. However, at a bias near zero, for frequencies below 500 Hz, the noise band clearly is not GR-noise limited. In fact, it is amplifier-limited because the noise from the detector is so low. While it is advantageous that the dark current from the QDIP is below detection, amplifier-limited measurements prevent the attainment of true  $D^*$  values. In an effort to account for the amplifier noise, the noise spectrum for the amplifier alone is subtracted from the signal and noise FFT spectra measured for the QDIP. Another noise contribution that occurs at low frequencies, known as  $1/f$  noise, also prohibits a flat-band noise spectrum below 500 Hz, and is shown in Fig. 3.3.3. Thus, the photocurrent response measurements are obtained by averaging the detector signal over a 50 Hz bandwidth centered around the chopper frequency and averaging the detector noise over a similar bandwidth in a flat-band region ( $> 509$  Hz) of the FFT spectrum, taking care to avoid the chopper frequency and 60 Hz multiples.

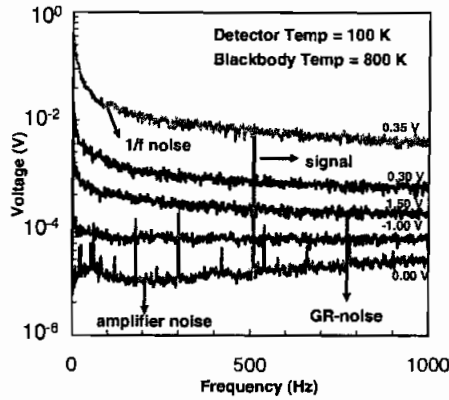


Figure 3.3.3 FFT noise spectra for vertical QDIP, demonstrating an increasing noise floor and decreasing signal-to-noise ratio due to contributions from dark current, GR-noise, amplifier noise, and 1/f noise.

### Transport studies in QDIPs and calculation of performance limits

The mechanism of IR detection in QDs is shown schematically in Figure 3.4.1. When IR photons impinge on the QDIP, photo-excited carriers escape from the QD so that they can be collected as photocurrent. However, once photoexcited carriers are in the continuum, they can experience several additional processes. Possible transport mechanisms include: 1) drift in the continuum under the influence of an electric field, 2) capture into the excited state of either the same QD or a different one, and 3) collection at a device contact. These processes are shown schematically in Figure 3.4.2.

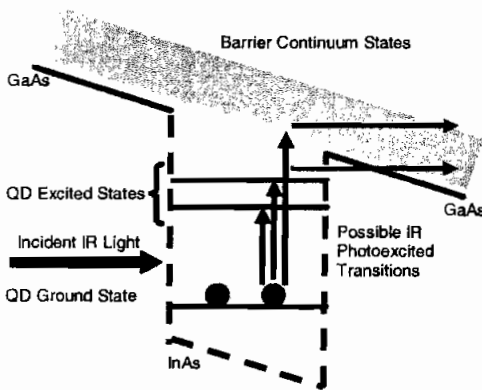


Figure 3.4.1 Schematic diagram of InAs/GaAs QDIP conduction band under bias

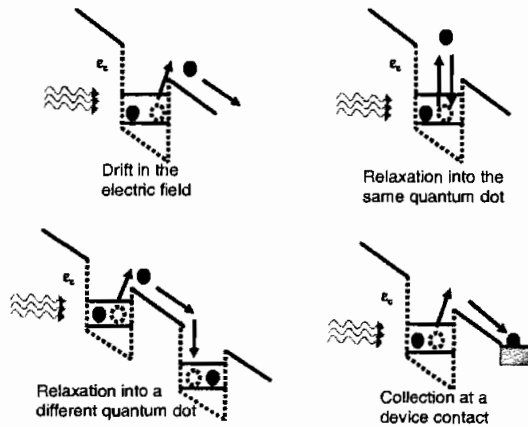


Figure 3.4.2 Schematic depiction of possible transport mechanisms for photoexcited electrons in the QDIP active region. These processes affect the calculation of the effective electron lifetime.

The effective carrier lifetime is essential to QDIP performance in that if the lifetime is too short, a photoexcited carrier will relax to the ground state before it has a chance to be collected as photocurrent. However, if the effective carrier lifetime is long enough, an efficient detector can be realized since photoexcited carriers are more likely to contribute to the photocurrent. We have calculated the effective electron lifetime in InAs/GaAs QDIPs using the Monte Carlo technique for simulating transport in QD heterostructures. The simulation consists of two coupled domains: normal transport in extended states (barrier and wetting layers) and capture of

electrons into quantum-dot confined states, while in the extended states, the simulation consists of free-flight followed by a scattering event, as is the case in standard Monte Carlo simulations. Polar optical, acoustic, and inter-valley phonon scattering are included, as well as scattering from the quantum dots. The simulation includes transport in the  $\Gamma$ ,  $L$ ,  $X$  and valleys. In addition to acting as scattering centers, the InAs–GaAs quantum dots manifest themselves by capturing an electron from the extended states to a confined state. An electron may be captured only when it is spatially within a dot. In this way, the dot density is taken into account. Furthermore, an electron may be captured only if its energy (measured from the barrier conduction band) is less than the optical phonon energy. The calculated lifetime for bound-to-continuum is shown in Figure 3.4.3(a). As can be seen from the calculated result, at low fields, the average excess electron energy above the QD heterojunction step was well below the phonon energy, and the effective carrier lifetime changed very little as a result. However, for electric fields ( $F$ ) greater than 2 kV/cm, the average excess electron energy exceeded the phonon energy, and carrier capture was suppressed resulting in longer effective lifetimes. For a fixed electric field value, the dependence of the effective carrier lifetime,  $\tau_{eff}$ , on the low-field capture time,  $\tau_c$ , was linear. Also, the slope of the  $\tau_{eff}$ – $F$  plot is proportional to  $\tau_c$ , given by:

$$\frac{d\tau_{eff}}{dF} \equiv 0.25 \frac{\tau_c}{F}, \quad (3.4.1)$$

where  $F$  is in kV/cm and  $\tau_c$  is in ps. It is important to note that for typical InAs/GaAs QDIPs, the electric field is  $\sim 5$  kV/cm at the operating bias, which corresponds to an effective electron lifetime of  $\sim 0.1$  ns for a capture time of 100 ps.

Figure 3.4.3(b) shows the calculated effective carrier lifetimes for barrier heights ranging from 5 to 100 meV. Using 30 ps as the low-field relaxation time, we find the same trend in the bound-to-bound detectors that is observed in the bound-to-continuum detectors. That is, at low fields, there is little change in the carrier lifetime since the average electron energy is small, but at higher fields the carrier lifetime increases linearly. It is important to note that for larger barrier heights, there is little improvement in carrier lifetime even for large fields. This again stresses the importance of reducing the barrier height, if possible.

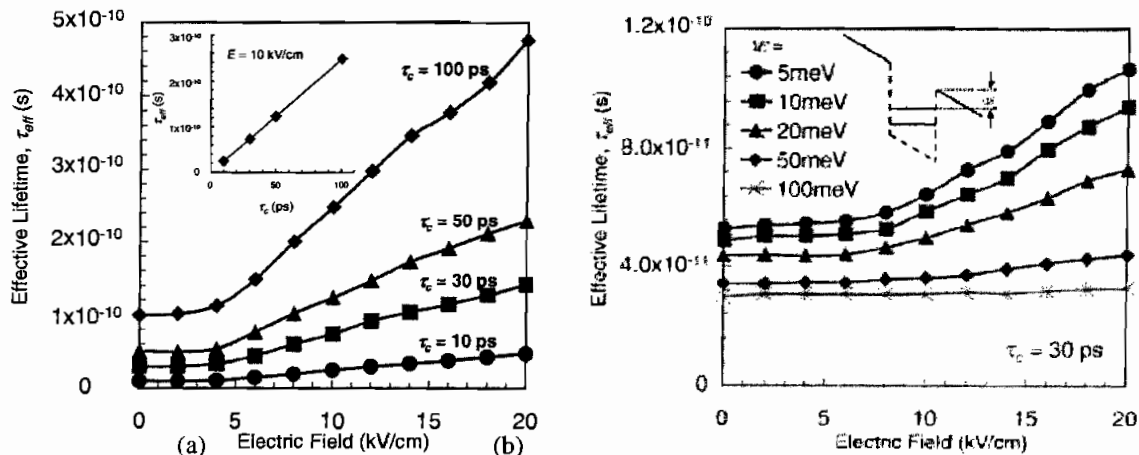


Figure 3.4.3(a) Electron effective lifetime as a function of applied transverse electric field in normal-incidence, bound-to-Continuum InAs/GaAs QDIPs subject to various electron capture times. The inset shows the linear dependence of the effective lifetime on the capture time for a given value of the electric field. (b) Calculated effective carrier lifetime in bound-to-bound QDIPs for various dot barrier heights ranging from 5 to 100 meV.

Models have also been developed by our group in the course of this program, which allow the abinitio calculation and prediction of important QDIP characteristics, such as dark current density and peak responsivity. The dark currents were calculated by assuming thermionic emission and field assisted tunneling to be the main contributors. In these calculations, the effective density of states has contributions from three parts - the quantum dot layer, the wetting layer as well as the bulk. The transfer matrix method was used to calculate the tunneling probability, in which the position of the Fermi level was decided by the doping level in the quantum dots. The scattering of the carriers by the quantum dots during transport was given due consideration. Calculations were done taking into account the various parameters, which affect the dark current namely, temperature, doping level in the quantum dots, barrier thickness and the number of quantum dots layers in the detector structure. The calculated dark current density as a function of bias is shown in Fig. 3.4.4(a) for various parameter values. The calculated dark currents are compared in this figure with the best available measured dark currents of QWIPs and MCT detectors. The spectral responsivity is dependent on the photoconductive (PC) gain as well as the quantum efficiency ( $\eta$ ); and can be expressed as:

$$R(\lambda) = \frac{q\lambda}{hc} \eta_{quant} g \quad (3.4.2)$$

The PC gain exhibits dependence on the bias voltage, the number of quantum dot layers as well as the spacer thickness, while the  $\eta$  values are affected by the number of layers of QD in addition to the absorption coefficient of the QD material. The variation of calculated peak responsivity with bias is being shown in Fig. 3.3.4(b). These calculations will allow us to predict the performance of QDIPs with different heterostructures.

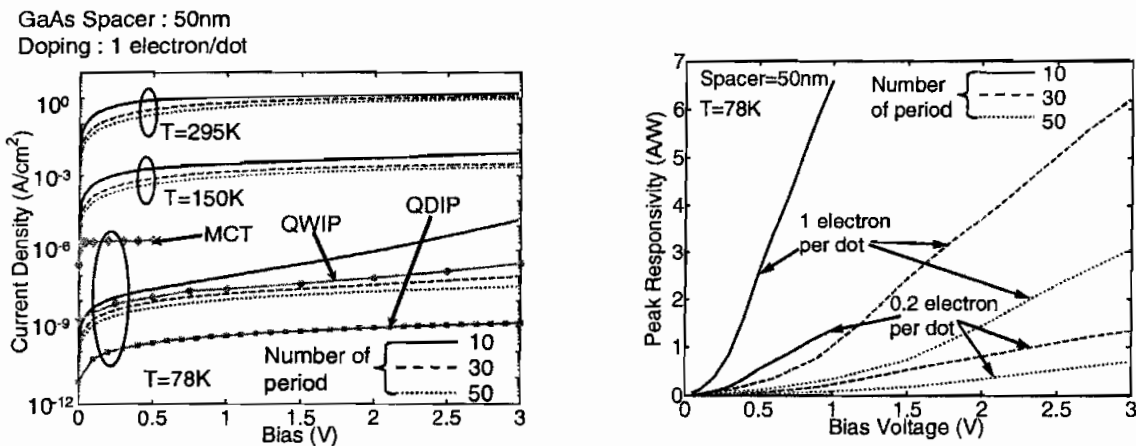


Figure 3.3.4 Calculated (a) dark current density and (b) peak responsivity as a function of bias voltage for a QDIP with varying (i) number of QD layers, (ii) temperature and (iii) doping in QDs.

### Characteristics of MIR detectors

#### (a) 70-layer detectors

In order to optimize detector performance, we have investigated a 70-layer QDIP device heterostructure that has yielded high responsivity, low dark current and large detectivity. The heterostructure schematic is shown in Fig. 3.5.1. The salient features of this device design are the large number of quantum dot layers, leading to increased absorption in the active region, and the thick (50 nm) GaAs barriers in between dot layers, which reduces the dark current.

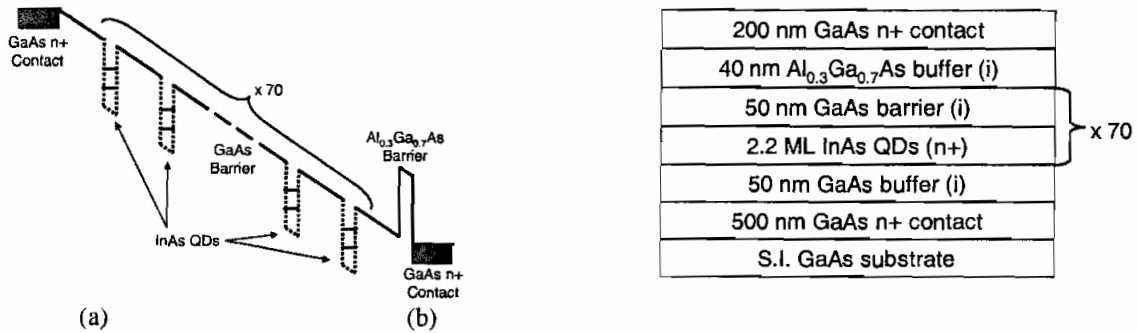


Figure 3.5.1. (a) Conduction band diagram and (b) device heterostructure schematic for the 70-layer QDIP.

The dark current density of the 70-layer QDIP is shown in Fig. 3.5.2. As can be seen from the figure, the device demonstrates extremely low dark current even at elevated temperatures ( $J_{\text{dark}}=2.3 \times 10^{-6} \text{ A/cm}^2$ ,  $V_{\text{bias}}=-2.0 \text{ V}$  and  $T=160 \text{ K}$ ). The device also has a large responsivity, shown in Fig. 3.5.3. The peak responsivity, at temperatures as high as  $T = 150 \text{ K}$ , is  $0.34 \text{ A/W}$  for  $\lambda_{\text{peak}} = 3.65 \mu\text{m}$  at  $V_{\text{bias}} = 4.0 \text{ V}$ .

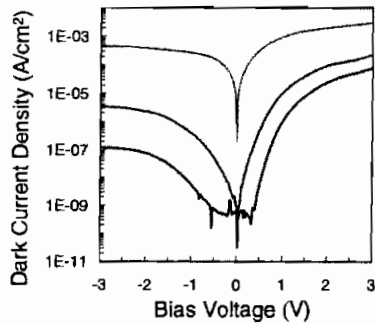


Figure 3.5.2 Measured dark current density as a function of bias.

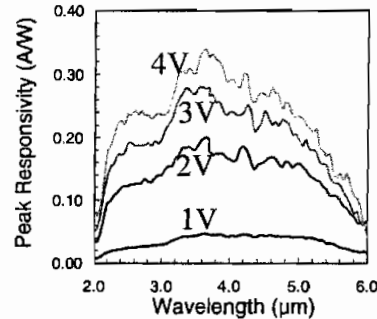


Figure 3.5.3 Measured responsivity under different bias voltage.

The increased absorption and reduced dark current of the 70-layer QDIP has resulted in state-of-the-art performance at very high temperatures. The estimated values of the detectivity and noise-equivalent temperature difference, shown in Figs. 3.5.4(a) and (b), respectively, demonstrate the applicability of these devices to high-temperature focal plane arrays.

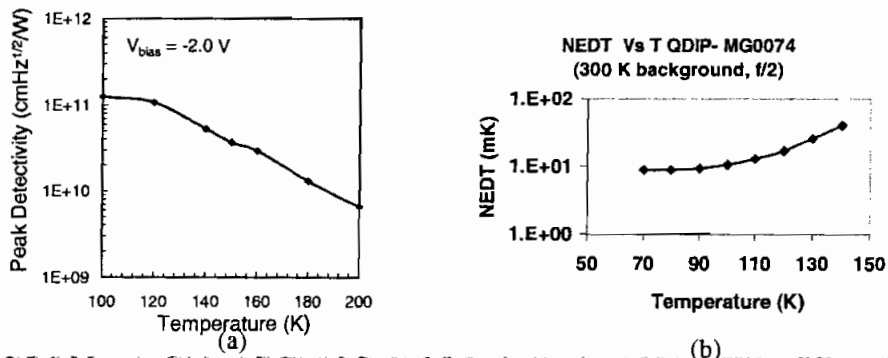


Figure 3.5.4 Measured (a) peak detectivity and (b) noise-equivalent temperature difference as a function of temperature for a 70-layer QDIP.

(b) Superlattice dot-in-a-well QDIP

To increase the responsivity we have investigated a novel superlattice dot-in-a-well (SL DWELL) QDIP heterostructure, which is a variation of the DWELL-QDIP concept. There are several advantages for this device design, the heterostructure schematic for which is shown in Fig. 3.5.5. First, InAs quantum dots grown on AlAs have increased dot density, leading to more efficient absorption. Secondly, the AlAs barrier provides increased carrier confinement in the vicinity of the undoped quantum dots. The creation of electronic minibands provides efficient carrier transport through the device, which is a third advantage. In addition, multiple bound-to-miniband transitions can occur from the quantum dot ground/excited states, providing a method for tuning the spectral response of the device. For example, in Fig. 3.5.6, the electronic minibands of a 10-period AlAs/GaAs SL barrier with a width of 15 nm are shown, having been determined using a self-consistent Schrödinger-Poisson model. Finally, the presence of minibands leads to increased absorption due to the large number of final states therein and greater wavefunction overlap.

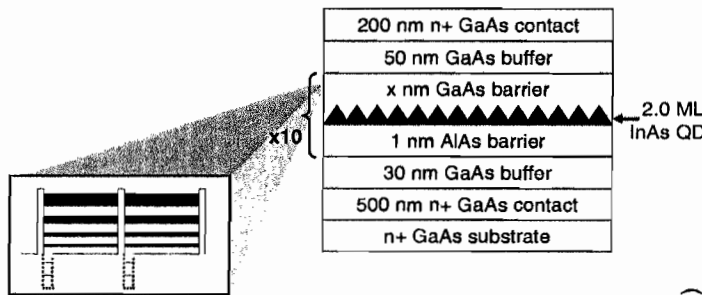


Figure 3.5.5 Heterostructure schematic of AlAs/GaAs SL DWELL QDIP, with a schematic inset of the conduction band showing the SL minibands and quantum dot levels.

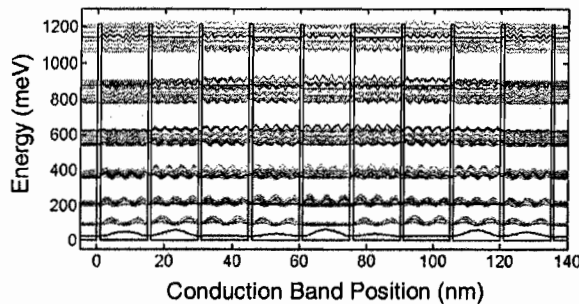


Figure 3.5.6 Calculated minibands for a 15 nm AlAs/GaAs SL barrier.

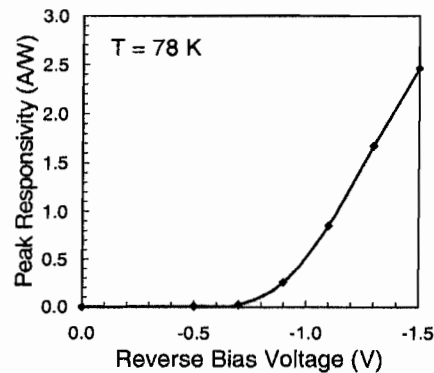


Figure 3.5.7 Peak responsivity as a function of bias voltage in a 15 nm AlAs/GaAs SL barrier QDIP at  $T = 78\text{K}$ .

However, the most important benefit of the SL DWELL QDIP may be that changing the width of the SL period enables the control of essential QDIP figures of merit. We have characterized SL DWELL QDIPs with varying SL width to determine how this parameter affects the responsivity and spectral response in particular. In general, we find that for increasing SL width, the QDIP figures of merit are degraded. The optimal SL width from our study is 15 nm. As shown in Fig. 3.5.7, for this device design, a maximum responsivity of 2.5 A/W is measured at 78 K at a bias of -1.5 V. The spectral response for this device peaks in the mid-wavelength infrared range ( $\sim 4 \mu\text{m}$ ). This compares very favorably with the best values obtained with other technologies.

### Characteristics of 8-12 $\mu\text{m}$ detectors

Long-wavelength (8-12  $\mu\text{m}$ ) detectors are useful for application in infrared focal plane arrays designed for high-resolution and high-sensitivity imaging. Long-wavelength detection based on intersubband transitions in quantum wells and on intersubband transitions from dot-in-well heterostructures, has been reported. There had been no report of long-wavelength detection with quantum dot infrared photodetectors at high temperatures ( $>100\text{K}$ ) before this study, here, we report the performance characteristics of InGaAs/GaAs QDIPs with peak wavelength responses at  $\sim 8 \mu\text{m}$ . This is the first time that long-wavelength detection in QDIPs is being reported at temperatures as high as 200K. The heterostructure schematic of the device is shown in Fig. 3.6.1(a); the dark current densities are also amongst the lowest measured in QDIPs. Unlike most previous work, the QDIPs in this study were grown on Si-doped high conductivity GaAs substrates, reducing the optical cross-talk between devices in the LWIR region. Therefore, the measured data reflect the true characteristics of a single device.

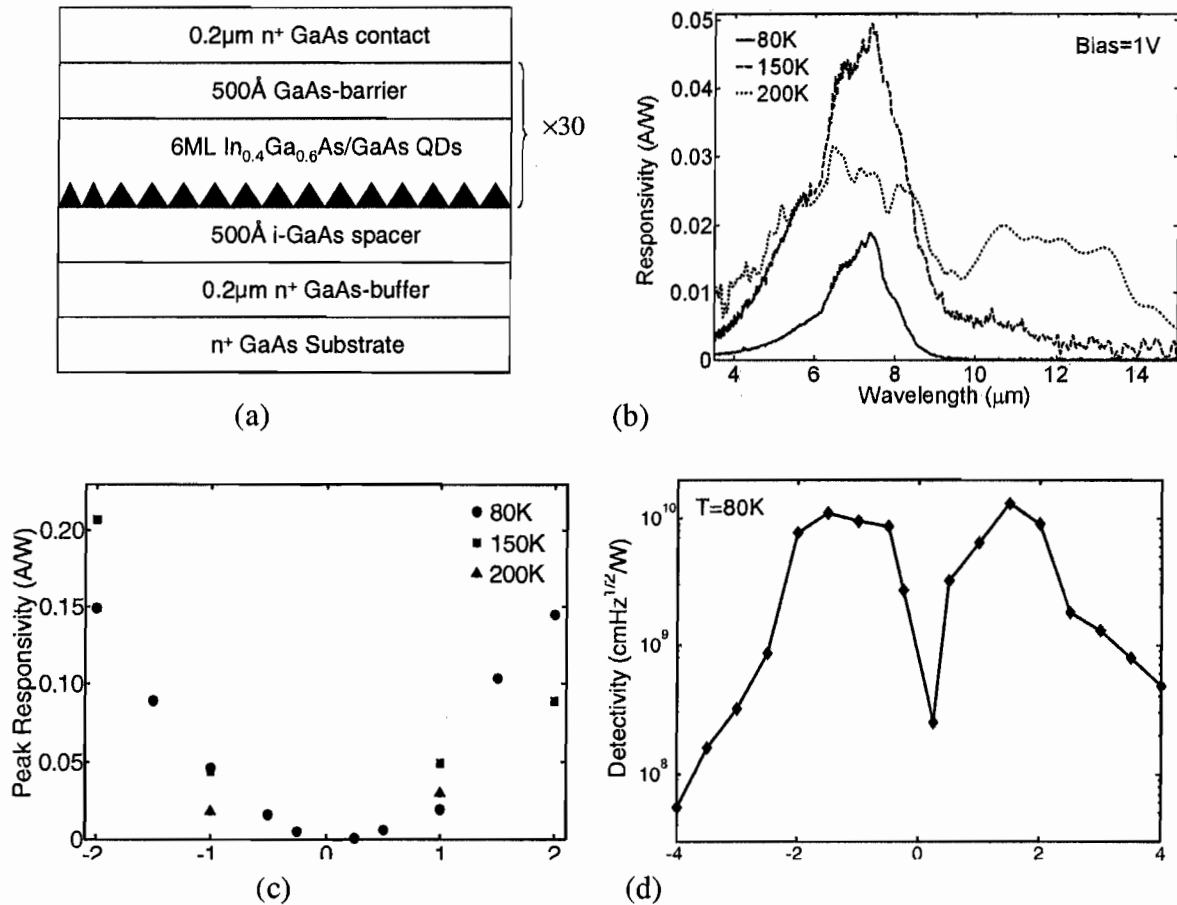


Figure 3.6.1 (a) Schematic of the 50-layer InGaAs/GaAs QDIP heterostructure; (b) Spectral response of the InGaAs/GaAs QDIP as a function of bias at 80, 150 and 200K; Measured (c) peak responsivity at different temperatures and (d) peak detectivity, as a function of applied bias for the 7.8  $\mu\text{m}$  response at T = 80K.

The spectral response of a typical device is shown in Fig. 3.6.1(b). The origin of the peak, centered at 7.8  $\mu\text{m}$ , can be explained by considering the energy positions of electronic states of

the InGaAs quantum dots, calculated with a 8-band  $k \cdot p$  formulation. The transition with a peak at  $\sim 7.8 \mu\text{m}$  (155 meV) is thought to be due to transitions from the dot ground state to the GaAs barrier states or the wetting layer states. The peak responsivity for the  $7.8 \mu\text{m}$  photoresponse is plotted in Fig. 3.6.1(c) as a function of bias for  $T = 80\text{K}$ . The peak responsivity reaches a value of  $0.23 \text{ A/W}$  at  $150\text{K}$  at a bias of  $-2\text{V}$  and is adequately high for application in focal plane arrays. The specific detectivity ( $D^*$ ), which is a measure of the signal-to-noise ratio of the device, was obtained from the measured peak responsivity and noise density spectra at different temperatures and applied biases. The measured values of  $D^*$  for  $7.8 \mu\text{m}$  response at  $80\text{K}$  are plotted in Fig. 3.6.1(d) as a function of bias. The value of  $D^*$  reaches a maximum of  $2.0 \times 10^{10} \text{ cm.Hz}^{1/2}/\text{W}$  at  $2\text{V}$  and decreases thereafter, due to the monotonic increase of the dark current with bias. These values of  $D^*$  are amongst the highest measured for QDIPs in the LWIR range and are attributed to the extremely low dark currents measured in these devices.

### Tunnel quantum dot infrared photodetectors

A central problem in infrared detectors is the commonality of the transport paths of the carriers contributing to the dark- and photo-currents. Hence, any heterostructure design aimed at reducing the dark current also reduces the photo current. In this program we have conceived, designed, and demonstrated the properties of a novel device – the tunneling QDIP – in which the electrons contributing to the photocurrent are selectively collected from the quantum dots by resonant tunneling, while these same tunnel barriers block the electrons, with a broad energy distribution, that contribute to the dark current. The band diagram of the tunneling QDIP (T-QDIP) under an applied transverse bias is shown in Fig. 3.7.1(a). The purpose of the single  $\text{Al}_{0.1}\text{Ga}_{0.9}\text{As}$  barrier, asymmetrically placed on the side of the dot opposite to the tunnel barriers, is to create well-defined quasi-bound final states in the quantum well for the photo-excited electrons. These states also resonate with the tunneling states in the  $\text{In}_{0.1}\text{Ga}_{0.9}\text{As}/\text{Al}_{0.3}\text{Ga}_{0.7}\text{As}$  double barriers resonant tunnel heterostructure, thereby optimizing the tunnel rate and hyperspectral photoresponse. The tunnel probability is therefore near unity, as confirmed by calculations, for photoexcited electron transitions whose energies coincide with the QD bound state to well final state energy difference. The complete device heterostructure is schematically shown in Fig. 3.7.1(b).

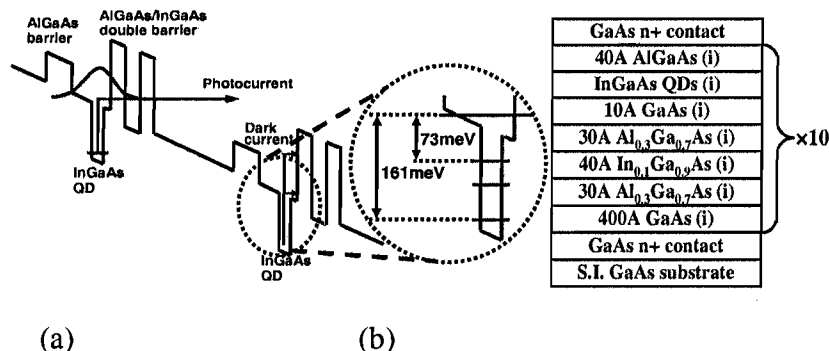


Figure 3.7.1 (a) Schematic diagram of the conduction band profile of InGaAs/GaAs tunneling QDIP (T-QDIP) using resonant AlGaAs double-barriers. The figure also shows the various electronic transitions explaining the measured spectral response; (b) schematic heterostructure of a T-QDIP grown by molecular beam epitaxy.

The bias-dependent dark current in a QDIP can be simply expressed as:

$$I_D(V) = e v(V) n_{em}(V) A \quad (1)$$

where  $v$  is the average electron drift velocity in the barrier continuum,  $n_{em}$  is the concentration of electrons excited out of the quantum dots by thermionic emission and tunneling, and  $A$  is the detector area. Here,

$$v(V) = \frac{\mu F(V)}{\sqrt{1 + (\mu F(V)/v_s)^2}} \quad (2)$$

and

$$n_{em}(V) = \int_{-\infty}^{\infty} N(E) f(E) T(E, V) dE, \quad (3)$$

where  $\mu$  is the electron mobility,  $F$  is the bias-dependent electric field,  $v_s$  is the saturation velocity,  $f(E)$  is the Fermi-Dirac distribution function,  $N(E)$  is the density of states, and  $T(E, V)$  is the tunneling probability (across a triangular barrier).  $E$  is the total energy, rather than the energy associated with the tunneling direction, since in a real system electron scattering causes the electron wavefunction to decay in the barriers in accordance with the total energy of the electrons. The tunneling probability is calculated using the transfer matrix method. For both square and triangular potential barriers, segmentation is employed to simplify the calculations, wherein the barrier potential is a constant  $V_j$  in the  $j^{\text{th}}$  segment. The corresponding one-dimensional plane wave associated with the electron is:

$$\psi_j(z) = A_j \exp(k_j z) + B_j \exp(-ik_j z) \quad (4)$$

where  $k_j = 2\pi\sqrt{2m_j^*(E - V_j)}/h$ ,  $h$  is Planck's constant and  $m_j^*$  is the effective mass. The tunneling probability is then given by:

$$T(E) = m_{N+1}^* k_0 / (m_0^* k_{N+1} M_{22}^2) \quad (5)$$

where  $M_{22}$  is the element of the transfer matrix  $\prod_{n=1}^{N+1} M_n$  with both column and row index equal to

2. The subscripts 0 and  $N+1$  correspond to points outside the barriers. The density of states function,  $N(E)$ , is made up of contributions from the quantum dots, wetting layer, and barrier regions and is given by:

$$N(E) = \sum_i \frac{2N_d}{L_p} \frac{1}{\sqrt{2\pi}\sigma} \exp\left(-\frac{(E - E_i)^2}{2\sigma^2}\right) + \frac{4\pi m^*}{L_p h^2} H(E - E_w) + \frac{8\pi\sqrt{2}}{h^3} m^{*3/2} \sqrt{E - E_c} H(E - E_c) \quad (6)$$

where, in the first term,  $N_d$  is the quantum dot surface density and  $E_i$  is the energy of discrete dot levels. The values of  $E_i$  are determined from an eight-band  $\mathbf{k}\cdot\mathbf{p}$  calculation, assuming a pyramidal shape of the dots and accounting for built-in strain through the valence force field model. A Gaussian distribution is included to take into account the inhomogeneous broadening due to size inhomogeneity of the dots. The second term is the density of the wetting layer states, which is calculated simply by assuming a two-dimensional electron gas in the wetting layer.  $E_w$  is the energy of the wetting layer state, and since the thickness of the wetting layer is small (less than 2 monolayers), only one confined state exists in this layer.  $H(x)$  is a rectangular function such that  $H(x) = 1$  for  $x \geq 0$  and  $H(x) = 0$  for  $x < 0$ . The last term gives the density of states in the bulk barrier material, and  $E_c$  is the energy of the conduction band edge therein.

The dark current formulation described above is for a conventional QDIP design. When a double-barrier resonant tunneling heterostructure is incorporated with the dots, the same

formulation can be used to calculate the dark current after suitably modifying the density of states,  $N(E)$ , and the tunneling probability,  $T(E, V)$ .

We have shown theoretically and experimentally that there is a reduction of dark current by almost 2 orders of magnitude (Fig. 3.7.2(a)). The measured dark currents as a function of bias and temperature are shown in Fig. 3.7.2(b). *The dark current densities shown in this figure are the lowest (e.g. 1.59 A/cm<sup>2</sup> at 300K for a bias of 1V measured in any QDIP.)*

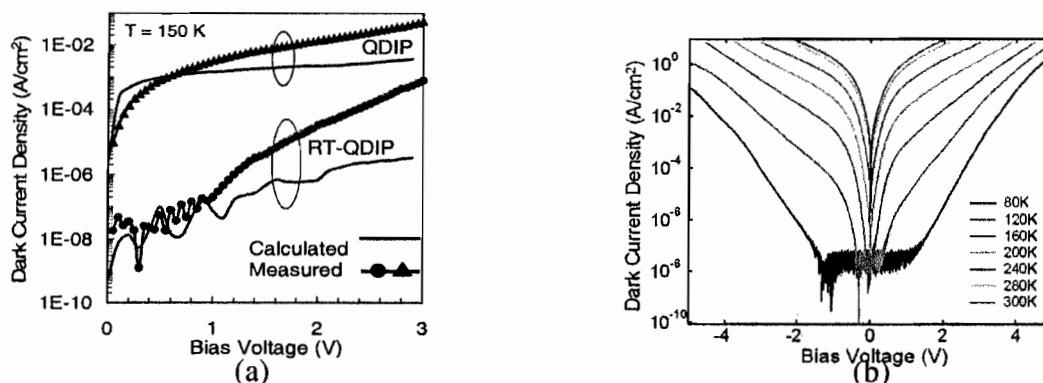


Figure 3.7.2 (a) Measured dark current density as a function of bias at different temperatures for T-QDIP; (b) comparison of dark current density in T-QDIP and conventional QDIP.

The spectral response at different bias at  $T = 80\text{K}$  is shown in Fig. 3.7.3(a). The dual peaks at  $5.7$  and  $6.2 \mu\text{m}$  in the photoresponse, arising from overlap of the wavefunctions of the quantum well states and the bound states of the double barrier heterostructure, provide evidence of the resonant tunneling action in this device. There is also clear evidence of room temperature operation. The measured  $D^*$  at  $80\text{K}$  is  $\sim 3 \times 10^{10} \text{ cmHz}^{1/2}/\text{W}$  at a bias of  $2\text{V}$ , which is shown in Fig. 3.7.3(b).

A strong photoresponse in the FIR, with a peak at  $17\mu\text{m}$ , was observed at high temperatures ( $T > 240\text{K}$ ). At these temperatures, the FIR photoresponse becomes the dominant one. We believe this response results from photoexcitation of electron from the dot excited states, which are preferentially occupied at high temperatures, to the quasi-bound tunneling states in the quantum well, as indicated in Fig. 3.7.1(a). The energy separation of  $73 \text{ meV}$  corresponds exactly to  $17\mu\text{m}$ . The low dark current also aids in room temperature detection of the FIR excitation. The measured spectral responsivity is shown in Fig. 3.7.4(a). The peak responsivity and detectivity at  $280\text{K}$  are  $0.16 \text{ A/W}$  and  $1.57 \times 10^7 \text{ cmHz}^{1/2}/\text{W}$  (Fig. 3.7.4(b)), respectively, and the value of these parameters start to decrease at  $300\text{K}$ .

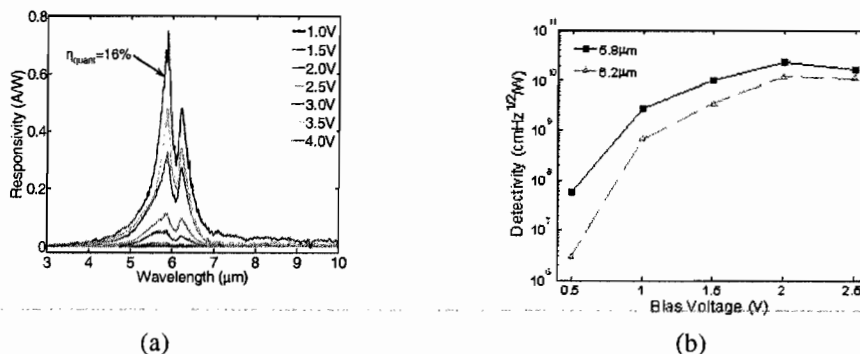


Figure 3.7.3 (a) MID-IR responsivity as a function of wavelength at different biases for T-QDIP at  $80\text{K}$  and (b) detectivity as a function of bias at  $80\text{K}$ .

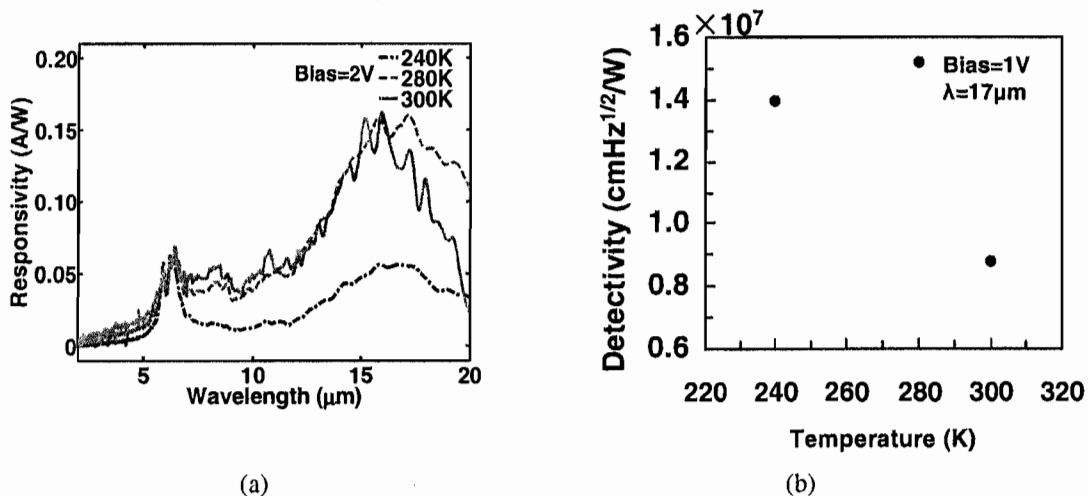


Figure 3.7.4 (a) FIR spectral responsivity of T-QDIP as a function of wavelength at different temperatures and (b) detectivity as a function of temperature under a bias of 1V.

### QDIP for terahertz detection

Terahertz sources and detectors, operable in the 1-3 THz spectral range, have gained importance at the present time for application in spectroscopy, imaging, material testing and communication. The operation of the T-QDIP at THz frequencies is demonstrated, for the first time, made possible by suitable engineering of the energy levels in InAlAs/GaAs quantum dots of reduced size. The peak and cut-off wavelength of the spectral response are at  $50\mu\text{m}$  and  $78\mu\text{m}$  (3.8THz), respectively and the devices can be operated upto 150K.

The dark current density as a function of bias voltage and temperature is shown in Fig. 3.8.1. The dark current densities at a bias of 1V are  $4.77 \times 10^{-8}$ ,  $2.03 \times 10^{-2}$  and  $4.09 \text{A/cm}^2$  at 4.2K, 80K and 150K respectively. These values are very low compared to other THz detectors. The calibrated spectral response of the T-QDIP at 4.6K, with bias of 1.0V, is shown Fig. 3.8.2 (a). The peak responsivity  $R_p$  is  $0.45 \text{A/W}$  at  $50\mu\text{m}$ . The cutoff wavelength is  $\sim 78\mu\text{m}$ , which corresponds to  $\sim 3.8 \text{THz}$ . The response is due to the transition of photoexcited electrons from the ground states in the quantum dot to the quasi-bound states in the well. The dark region (dip) centered at  $\sim 37\mu\text{m}$  is due to GaAs longitudinal optical phonon absorption. Figure 3.8.2 (b) shows responsivity spectra at 150K from devices in which the  $\text{In}_{0.6}\text{Al}_{0.4}\text{As}$  dots are slightly larger. The response peak is shifted to shorter wavelengths. The measured specific detectivity ( $D^*$ ) at 4.6K, obtained from  $R_p$  and noise density spectra, is shown in Fig. 3.8.3. The  $D^*$  values are  $1.45 \times 10^8$  and  $4.98 \times 10^7 \text{cm}\cdot\text{Hz}^{1/2}/\text{W}$  at 4.6K and 80K, respectively, under a bias of 1V.

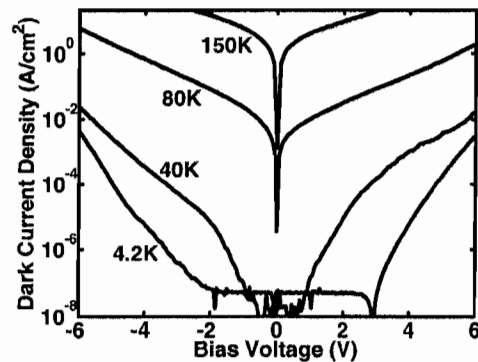
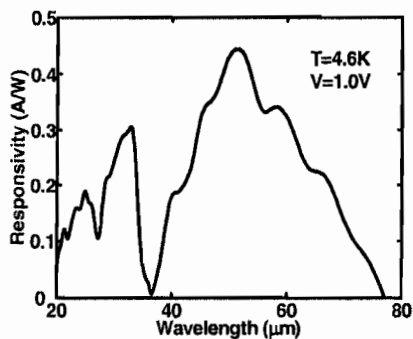
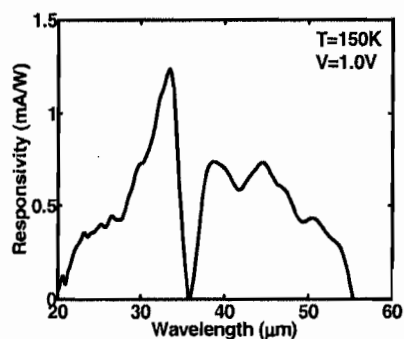


Figure 3.9.1 Measured dark current density as a function of bias and temperature.



(a)



(b)

Figure 3.9.2 Measured spectral responsivity of T-QDIP at (a) 4.6K and (b) 150K under bias of 1V.

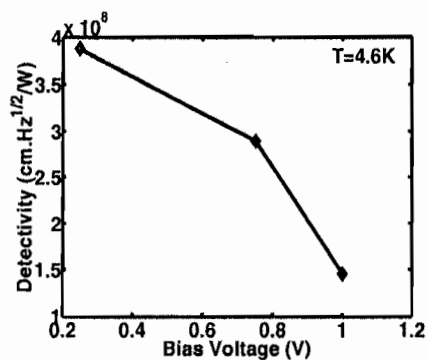


Figure 3.9.3 Measured specific detectivity as a function of bias at 4.6K.

### QDIPs for arrays

The ultimate goal for research on infrared detectors is to incorporate an array of photodetectors into the focal plane array (FPA) of an IR camera. A significant reduction in the cost of IR cameras is possible if the photodetectors operate at temperatures  $\geq 120$  K, enabling the use of thermo-electric coolers.

Imaging with a small array of QDIPs was demonstrated by our group for the first time; details of which will be presented later. Larger QDIP FPA arrays have subsequently been demonstrated and some images taken by QDIP arrays are shown in Fig. 3.9.1.

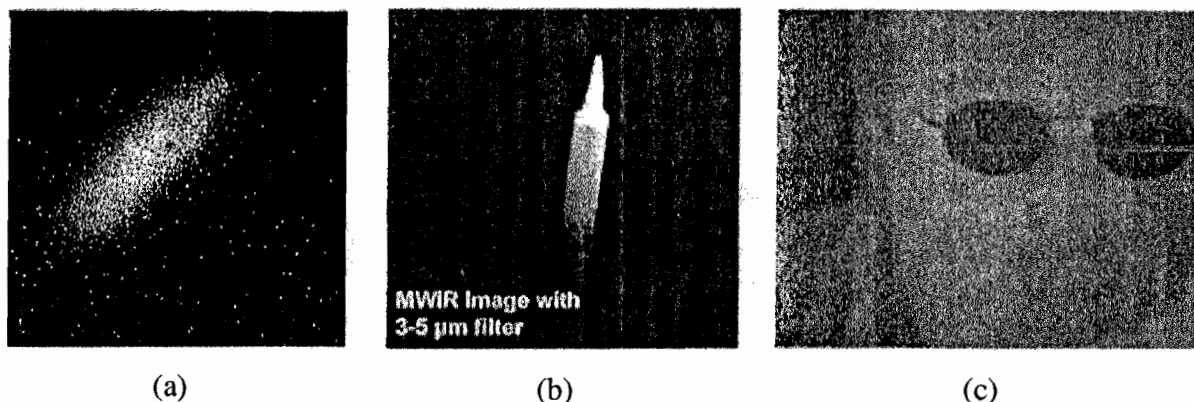


Figure 3.9.1(a) Thermal image of a hot soldering iron head taken by a 256×256 QDIP FPA camera at  $T=120$ . The image was demonstrated by J. Jiang *et al.* (b) images of a soldering iron and (c) thermal image of the scientific personnel obtained from a 320×256 focal plane array at 80k. Both images were demonstrated by S. Krishna *et al.*

### (a) Focal Plane Array Fabrication

FPA fabrication is complicated in that it requires expensive equipment and specific expertise to perform the hybrid bump-bonding, or flip-chip bonding, of the photodetector array and the silicon read out integrated circuit (ROIC). The hybridization required for fabricating a FPA is also difficult due to the stringent requirements of the ROIC, such as operating bias,

charge well capacity, and operating temperature. These requirements impose performance limits on the photodetector array, especially those related to the dark current, responsivity, and detectivity. Photodetector arrays are relatively straightforward to realize independently; requiring the MBE growth of a QDIP heterostructure on a large-area, epi-ready wafer followed by the fabrication of an array of vertical geometry QDIPs with small features (pixel area  $\leq 50 \times 50 \mu\text{m}^2$ , pitch  $\leq 125 \mu\text{m}$ ). Similarly, the ROICs, while expensive, are easily obtained commercially, available in a range of sizes from (1x124) to (1024x1024). The difficult aspect is integrating these two arrays, which is achieved through flip-chip bonding in which large indium bumps electrically connect individual pixels of the photodetector and ROIC arrays.

The In bump, which is deposited as a column on the top surface of each photodetector (or ROIC) pixel through a thick photoresist, should be roughly twice as tall as the pixel height. Therefore, a  $3 \mu\text{m}$  tall detector pixel requires an In bump that is  $5\text{-}6 \mu\text{m}$  tall. The In bumps should not be deposited directly on Au contacts because the two metals react with each other, turning black and leading to the degradation of the device contact. Therefore, an intermediate layer is required between the top detector contact and the In bump. Chromium and palladium are suitable metals for providing the requisite adhesion of the In bump to the gold alloy contact, thus serving as a buffer layer with thickness ranging from  $10\text{-}50 \text{ nm}$ . In this way, the In bumps on each pixel serve as top contacts for transmission of the photocurrent (or photovoltage) signal. However, the bottom contact, which serves as the ground in the vertical QDIP geometry, must also be fabricated for the detector array and the ROIC. Typically, ground contacts are not required for each pixel since all device mesas share the same bottom contact layer, which is  $1\text{-}1.5 \mu\text{m}$  thick. Therefore, the fabrication of several small posts around the perimeter of the QDIP array is sufficient for providing the ground contact. These ground posts should be small enough in surface area so that they can be completely covered during In bump deposition. These posts must also be the same height as the detector pixels so that the ground contacts between the detector array and ROIC are connected during flip-chip bonding. The schematic of a section of a fabricated QDIP array, including In bump deposition and ground post fabrication, is shown in Fig. 3.9.2.

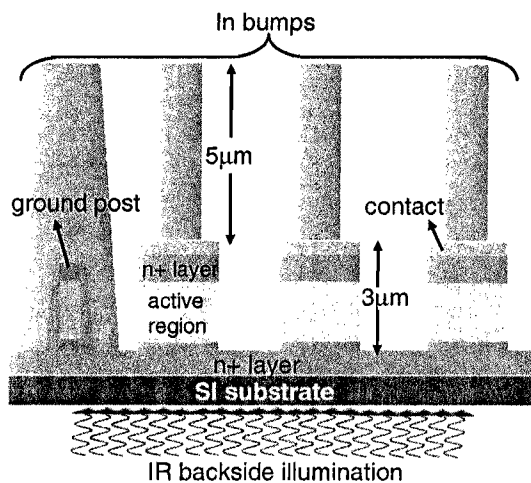


Figure 3.9.2 Schematic diagram of a fabricated QDIP array, illustrating the mesa etch for pixel definition and ground post fabrication, top contact metallization, and In bump deposition.

After In bumps have been deposited on either the detector array or the ROIC, flip-chip bonding is achieved by inverting the photodetector array and pressure-bonding to the silicon ROIC. Since the array features are small and densely packed, very sophisticated equipment is required to perform this flip-chip bonding, especially for the large-area FPAs typically used for IR imaging. Once the photodetector array and ROIC are properly bonded, the semi-insulating, GaAs substrate of the detector array must be thinned and polished so that IR detection can occur through backside illumination. Semi-insulating GaAs substrates, as opposed to n-type or p-type substrates, are used for the epitaxial growth of the QDIP array since these wafers transmit IR light. The substrate thinning process comprises diamond-cut turning of the  $\sim 500 \mu\text{m}$  substrate to roughly  $20 \mu\text{m}$ , followed by chemical etching to remove the rest of the GaAs substrate using an appropriate wet etch, such as HCl acid. An etch-stop layer with high aluminum content must therefore be grown directly above the GaAs substrate and before the bottom contact layer of the QDIP, such that the substrate can be selectively removed. Additional steps in the FPA fabrication process include the deposition of an epoxy at the detector array/ROIC interface for stabilization and the deposition of an anti-reflective coating on the backside of the detector array for better quantum efficiency.

We have been collaborating with Lockheed-Martin, Orlando and Santa Barbara Focal Plane in the realization of QDIP-based IR cameras. We have fabricated and shipped  $320 \times 256$  QDIP arrays to them for bounding with ROICs and characterization. The effort has been slowed down due to resource-related issues. We hope to demonstrate imaging with QDIP-based cameras in the near future.

*(b) Raster-scan imaging using a (13x13) QDIP array*

In an effort to demonstrate imaging using InAs/GaAs QDIPs, a raster-scan imaging system was developed, at the University of Michigan, in which the field-of-view was scanned simultaneously in the x- and y-axes by a raster scan motion provided by two mirrors. An array of photocurrent/voltage values was compiled as the field-of-view array elements were scanned either by a small, interconnected detector array. In this way, IR imaging with InAs/GaAs QDIPs was demonstrated using a raster scanning technique.

While raster-scan imaging should have worked with a single detector, a small array was actually used because it permitted the collection of IR light more easily due to the larger optical area. In addition, the average photocurrent from the array was larger, and therefore, easier to distinguish from background noise. Standard photolithography and wet-etch processing were used to fabricate (9x9) and (13x13) non-addressable (interconnected) arrays of QDIP pixels using as-grown, InAs/GaAs QDIP material. The pixel diameter was  $40 \mu\text{m}$ , and the array pitch was  $120 \mu\text{m}$ . An SEM image of an interconnected, (9x9) QDIP array is shown in Fig. 3.9.3. The entire array has a single top contact and a single bottom contact for all of the pixels, effectively behaving as a single detector with a very large optical area and generating a single photocurrent signal.

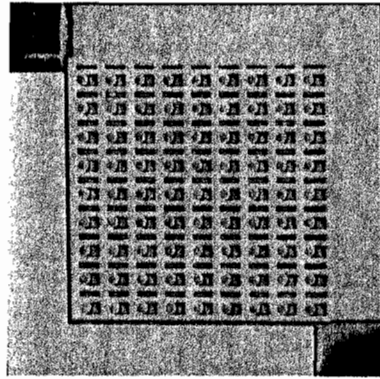


Figure 3.9.3 Scanning electron microscopy image of a (9x9), interconnected, InAs/GaAs QDIP array. A similar, (13x13) InAs/GaAs QDIP array was used for raster-scan imaging.

Raster scanning of the field-of-view (target or IR source) was accomplished using two gold-plated mirrors (highly-reflective in the MWIR and LWIR ranges) servo-actuated by galvanometers and mounted in an XY bracket. User interfacing with the galvanometers' drive circuitry was achieved with a computer-interfaced scan controller. The raster scan motion of the mirrors directed the IR light onto the QDIP for detection. The (13x13) QDIP array, with which the imaging experiments were conducted, was housed in a cryostat with a KRS-5 entrance window and held at a temperature of 80 K. The photocurrent produced in the QDIP array was amplified by a low-noise current amplifier, which also provided the bias voltage to the array. The output was further amplified by lock-in techniques, and the amplified signal was transmitted to the data acquisition system wherein each photocurrent/voltage signal obtained from the QDIP corresponded to the raster scan mirror positions and hence to a segment of the field-of-view. A schematic of the raster scan system is shown in Fig. 3.9.4. The resolution of images obtained by this raster scan technique was determined by the incremental motion of the two scanning mirrors, as well as the integration time (time constant) of the lock-in amplifier. In other words, small steps taken by the galvanometers controlling the scanning mirrors corresponded to a high resolution of the image. Based on the images obtained, which are discussed next, the raster scan measurement system was estimated to have a resolution of approximately 0.1 cm in target feature size.

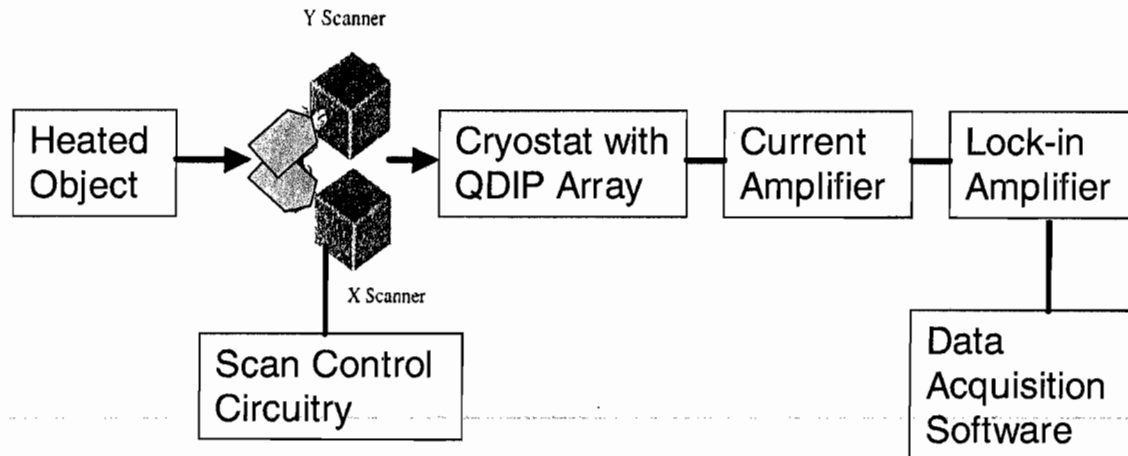


Figure 3.9.4 Schematic diagram of the raster-scan measurement system used to obtain IR images from a (13x13), interconnected, InAs/GaAs QDIP array at  $T = 80$  K.

Ideally, IR detectors are used to image everyday targets that are warm or hot. However, in this raster scan measurement system, a size constraint was imposed by the scanning mirrors in that the exit aperture in the XY bracket limited the field-of-view of the mirrors. Therefore, portions of heated objects or the illumination from suitable light sources were imaged. All of the objects imaged were placed directly in front of the XY mirror bracket, at 90 ° to the QDIP array and no more than 40 cm away from the mirror bracket entrance window. Figure 3.9.5(a) shows the image of a 20 W broadband IR global source through a circular pinhole with a diameter of approximately 2 cm. Figure 3.9.5(b) is the image of a 700 °C furnace igniter shielded by an aluminum block with a 1 cm diameter circular pinhole and a linear slit. There is some distortion present because the computer program used to display the images treats each array element as a rectangle, whereas the image array is actually square. Figure 3.9.5(c) depicts the partial image, in this case limited by the field-of-view of the scanning mirrors, of the heating element of a hot plate at 500 °C. Portions of the heated strips (schematically shown in the inset) are seen as the bright regions. The width of each metal strip is 2 cm with a 1.5 cm space between strips. All three images were obtained at different distances from the QDIP array, thus size comparisons cannot be made from image to image. These results indicate that, with progressive improvement of device performance, QDIPs should be applicable to IR imaging FPAs.

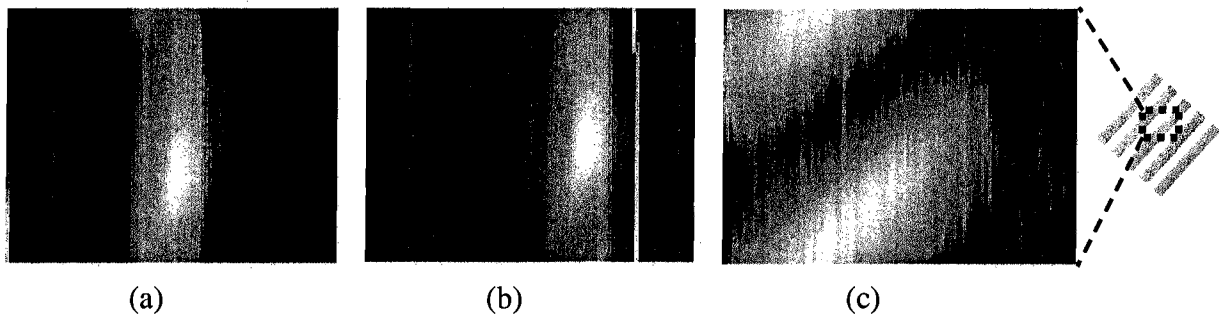


Figure 3.9.5 Raster-scanned images obtained from the (13x13), InAs/GaAs QDIP array at T = 80 K: (a) 20 W broadband IR global source through a circular pinhole, (b) 700 °C graphite furnace igniter through a circular hole and linear slit, and (c) 500 °C heating element from a hot plate, shown schematically in the inset, partially showing two metal strips.

### ***E. InAs/GaSb Type-II Strained-layer Superlattice Infrared Detectors (Bhattacharya)***

#### **Introduction**

InAs/Ga(In)Sb type-II strained-layer superlattices (SLSs) have recently attracted increasing interest as a promising alternative to HgCdTe for mid- and long-wavelength infrared (MWIR and LWIR) detection applications. InAs/GaSb superlattices have staggered band alignments, such that the conduction band edge of the InAs layer is lower than the valence band edge of the GaSb layer. As shown in Figure 1, the bandgap of the resulting type-II superlattices are smaller than their constituents. In addition, strains in InAs/GaInSb SLSs further reduce the superlattice bandgap. As a result, the cut-off wavelengths of InAs/Ga(In)Sb SLSs can be tuned between 3 and 30  $\mu\text{m}$  [1].

Optical absorption coefficients of InAs/Ga(In)Sb SLSs are comparable to that of HgCdTe. In addition, InAs/Ga(In)Sb SLSs have been suggested as having several inherent advantages over HgCdTe material systems, including lower tunneling dark current due to larger

electron effective mass, suppressed Auger recombination, the amenity to band structure engineering for optimum performance, and greater material uniformity [1]. Johnson noise limited detectivity of state-of-the-art MWIR InAs/GaSb SLS detectors exceeds  $10^{13}$  Jones at 77 K [2].

Our efforts to improve the performance and reliability of InAs/GaSb SLS detectors consist of three parts: the development of tunneling InAs/GaSb SLS detectors, carrier lifetime measurements and surface passivation study.

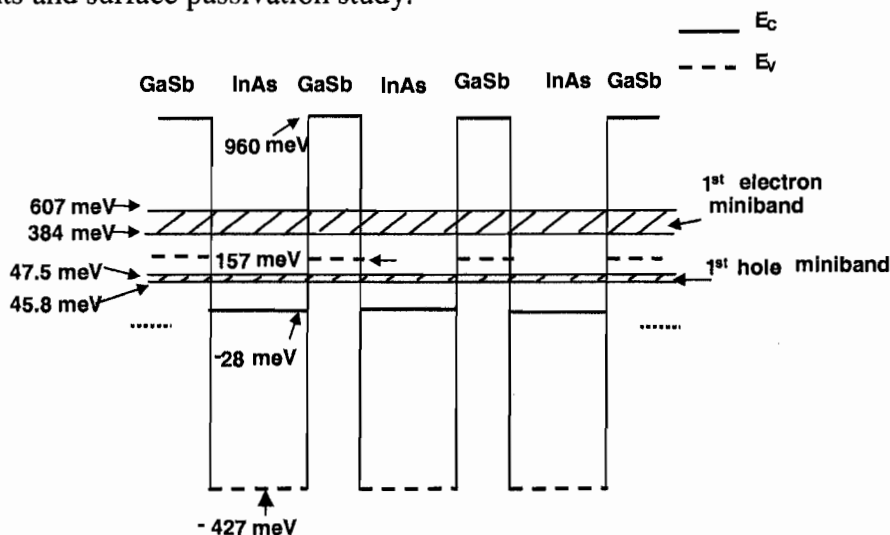


Figure 39. Band diagram of the 8 monolayer (ML) InAs/ 8ML GaSb superlattice calculated using the envelope function approximation method.

### Tunneling InAs/GaSb superlattice infrared photodetectors

Currently, normal intrinsic MWIR and LWIR detectors such as InAs/Ga(In)Sb SLS detectors have large diffusion dark currents at room temperature, which increase the detector noise and decrease the detector detectivity. To solve this problem, it was suggested that resonant tunneling barriers be inserted into a normal InAs/GaSb superlattice to suppress the dark current, while permitting carriers contributing to the photocurrent to pass through. This concept is illustrated in Figure 2.

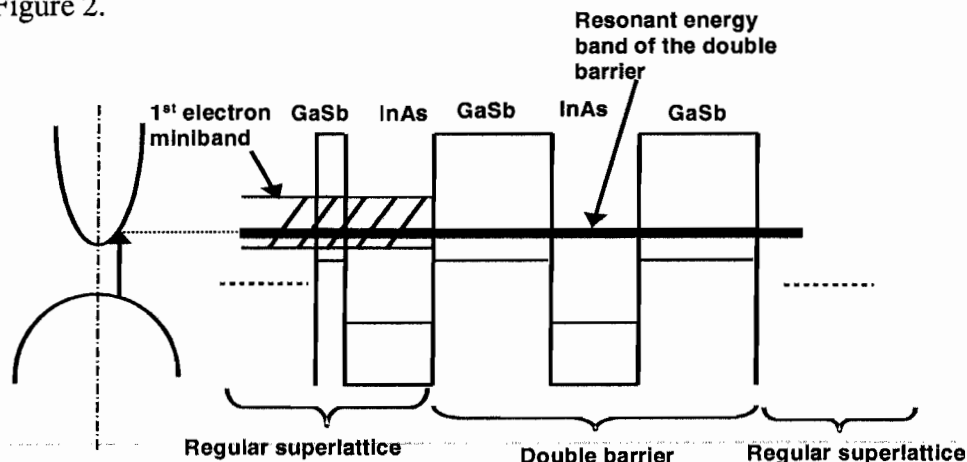


Figure 2. The band diagram of a tunneling InAs/GaSb superlattice under zero bias.

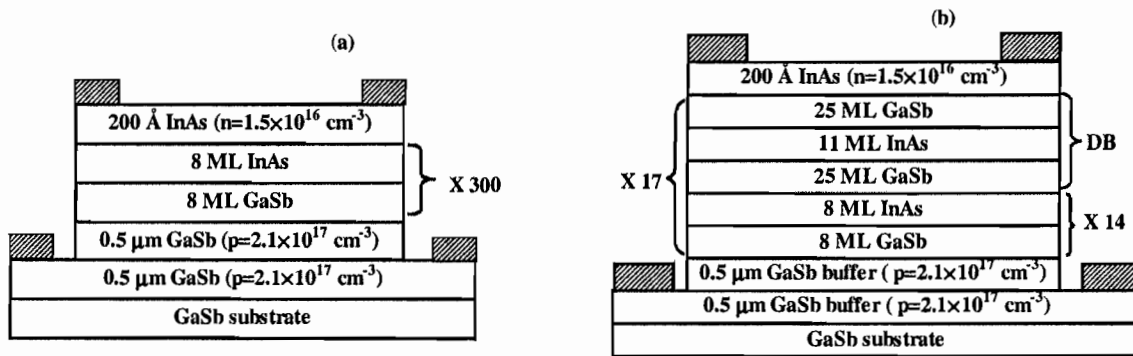


Figure 3. (a) The heterostructure schematic of the normal 300-period 8ML InAs/8ML GaSb SLS detector; (b) the heterostructure schematic of the tunneling 8ML InAs/8ML GaSb SLS detector.

The double barrier (DB) shown in Figure 2 has only one narrow resonant energy band located within the first electron miniband of the superlattice. As a result, the DB blocks most of the thermally generated carriers that are distributed in the entire first electron miniband, most of which have energies that are not aligned with the DB resonant energy. On the other hand, those electrons generated by photons of a specific wavelength have a very narrow energy distribution in the first electron miniband before they are transported over a long distance and significantly scattered. Thus, thicknesses of the InAs well and the GaSb barriers of the DB can be chosen such that the DB resonant energy is aligned with photon-generated electron of the specific energy of interest. In such a detector, the dark current will be more effectively reduced than the photocurrent, thereby improving the detector detectivity.

The heterostructure schematics of the normal and tunneling InAs/GaSb SLS infrared photodetectors are shown in Figure 3. The p-i-n superlattice photodiode structures were grown by molecular beam epitaxy on GaSb substrates and fabricated using standard optical lithography. The processed wafers were passivated in  $(\text{NH}_4)_2\text{S}$  21% : water=1:4 for two hours, diced into individual detectors and wire-bonded to leadless chip carriers.

The measured responsivities of both the normal and the tunneling InAs/GaSb SLS detectors are shown in Figure 4. The responsivity of the tunneling detector is about 27% lower than that of the normal detector. This is expected because the double barriers in the tunneling SLS detector inevitably block a portion of the photo-generated carriers.

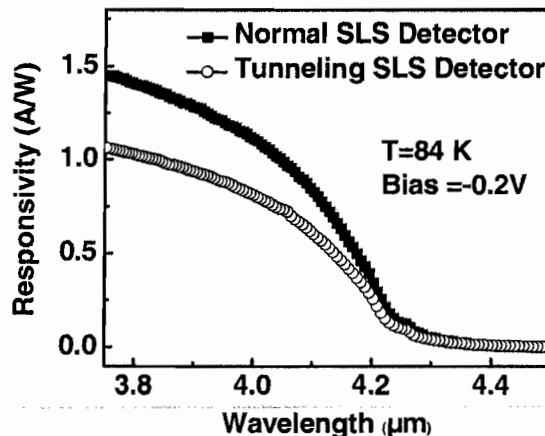


Figure 4. The responsivity spectra of the normal and tunneling 8ML InAs/8ML GaSb SLS detectors.

The measured relative spectral response of the normal InAs/GaSb SLS detector is plotted as a function of temperature in Figure 5 (a). Both the normal and the tunneling SLS detectors can operate at room temperature. The relative response of the normal and tunneling SLS detectors at  $\lambda=4\mu\text{m}$  at various temperatures is plotted in Figure 5 (b). The responses of both detectors peak at 210 K. According to Rodriguez [3], this can be explained by the fact that the background doping concentration of the nominally undoped InAs/GaSb SLS is the lowest when its type changes from n to p around 210 K.

The bias dependence of the response of both types of SLS detectors is shown in Figure 6. In the small bias range ( $-0.25\text{ V} \leq \text{bias} \leq 0.2\text{ V}$ ), the responsivity reaches its minimum at a forward bias of 0.1 - 0.15 V, which is believed to be due to the fact that the electric field in these photodiodes is the weakest at this bias, which counteracts the diode built-in potential. In the large bias range, the response increases monotonically with the bias. In these SLS photodiodes, the electron lifetime (measured to be about 3.7 ns by picosecond excitation correlation experiment) is larger than the transit time (estimated to be less than 0.1 ns), thus the charge neutrality principle causes a gain in these devices. The transit time decreases with the bias, therefore, the conversion efficiency (product of the gain and the quantum efficiency) increases with the bias.

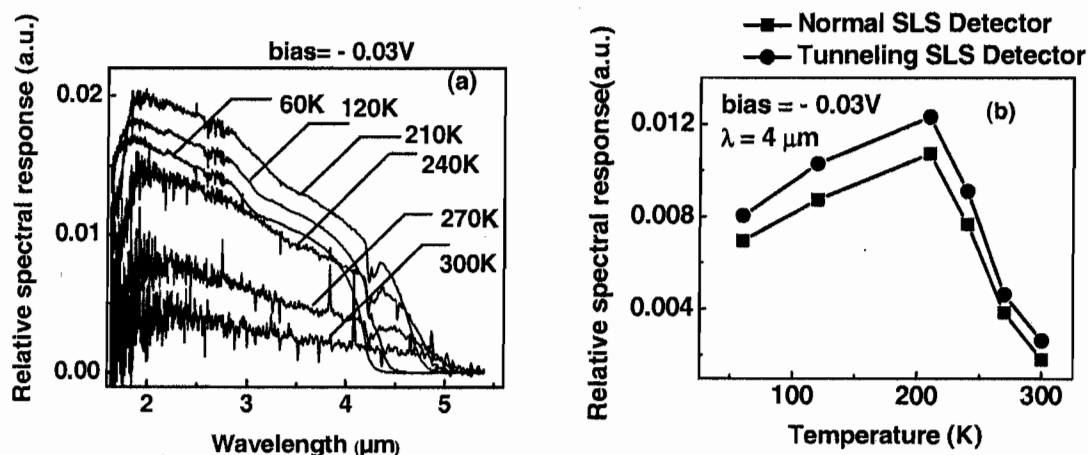


Figure 5 (a) Relative spectral response of the normal InAs/GaSb SLS detector as a function of temperature; (b) relative spectral response of both the normal and the tunneling SLS detector at a wavelength of  $4\mu\text{m}$  at various temperatures.

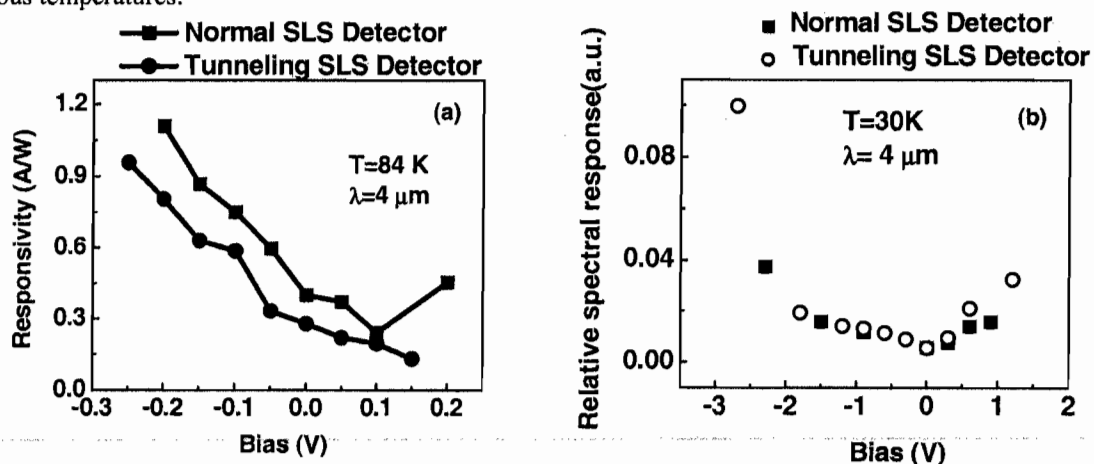


Figure 6 (a) Responsivity of the normal and tunneling SLS detectors as a function of bias (small bias); (b) relative response of the normal and tunneling SLS detectors under various biases (large bias).

Figure 7 (a) shows the dark current density of both types of detectors measured at 30 K. The dark current of the tunneling detector is reduced to about one-fifth of that of the normal SLS detector in the negative bias region. Using the zero-bias responsivity measured at  $\lambda=4\mu\text{m}$  and zero-bias dynamic resistance-area product ( $R_0A$ ), Johnson noise limited detectivity of the normal and tunneling InAs/GaSb SLS detectors at 84 K calculated using  $D_\lambda^* = R(\lambda)\sqrt{R_0A/kT}$  are  $5.6\times 10^9$  and  $6.6\times 10^9$  cm Hz<sup>1/2</sup>/W, respectively.

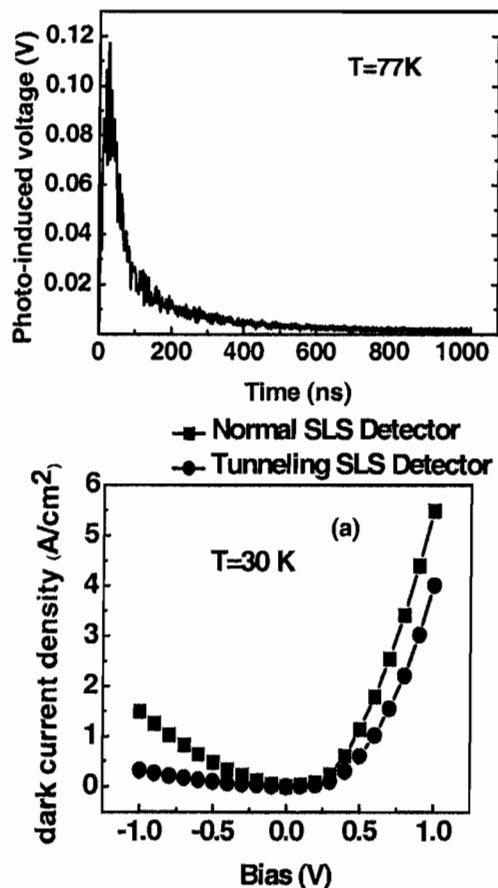


Figure 8. Photo-induced open-circuit voltage decay of the 8ML InAs/8ML GaSb SLS detector induced by a laser pulse.

Figure 7 (a) Dark current density of normal and tunneling InAs/GaSb SLS detectors measured at 30 K; (b) the detectivity of normal and tunneling InAs/GaSb SLS detectors obtained from noise current measurements.

Detectivity of both types of detectors obtained from measured spectral noise current is shown in Figure 7 (b), which does not clearly indicate any advantage of tunneling SLS detectors over normal SLS detectors. This is due to the small dark current reduction (a factor of 4 at 77 K) and the considerable photocurrent decrease (the responsivity is reduced by 27% at 84 K) in the tunneling detector. On the other hand, tunneling quantum dot infrared photodetectors (QDIPs) [4] have demonstrated two orders of magnitude reduction in dark currents. The tunneling SLS detector cannot reduce dark current as effectively as the tunneling QDIP for the following reason: tunneling SLS detectors are bipolar devices; therefore their double barriers cannot block both the electrons and the holes at the same time. This challenge does not exist in tunneling QDIPs that only use electron transition and transport for infrared detection.

### Carrier lifetime measurements

Improving carrier lifetimes is essential in the development of InAs/GaSb SLS detectors. To measure InAs/GaSb SLS carrier lifetimes, photo-induced open-circuit voltage decay (PVD) and picosecond excitation correlation (PEC) measurements were performed.

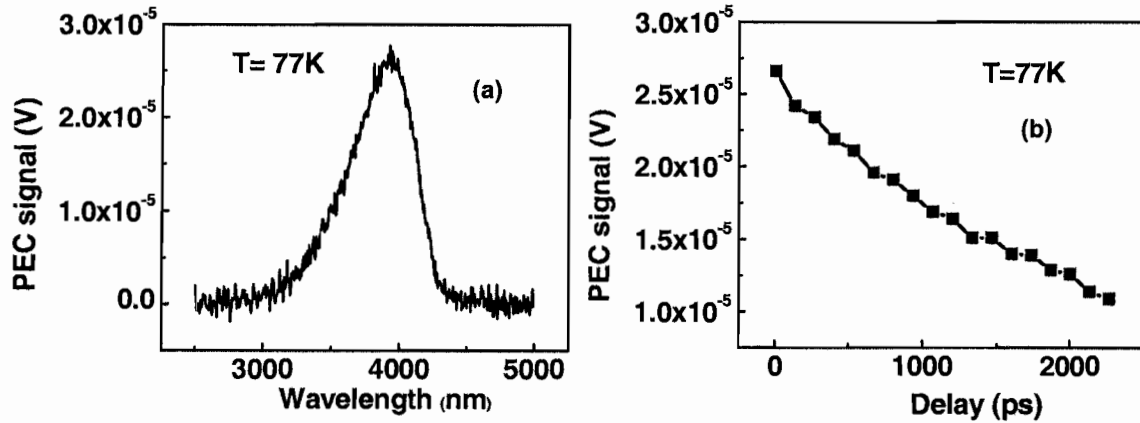


Figure 9 (a) PEC spectrum of the as-grown 8ML InAs/8ML GaSb superlattice; (b) PEC signal versus delay obtained from the as-grown 8ML InAs/8ML GaSb superlattice.

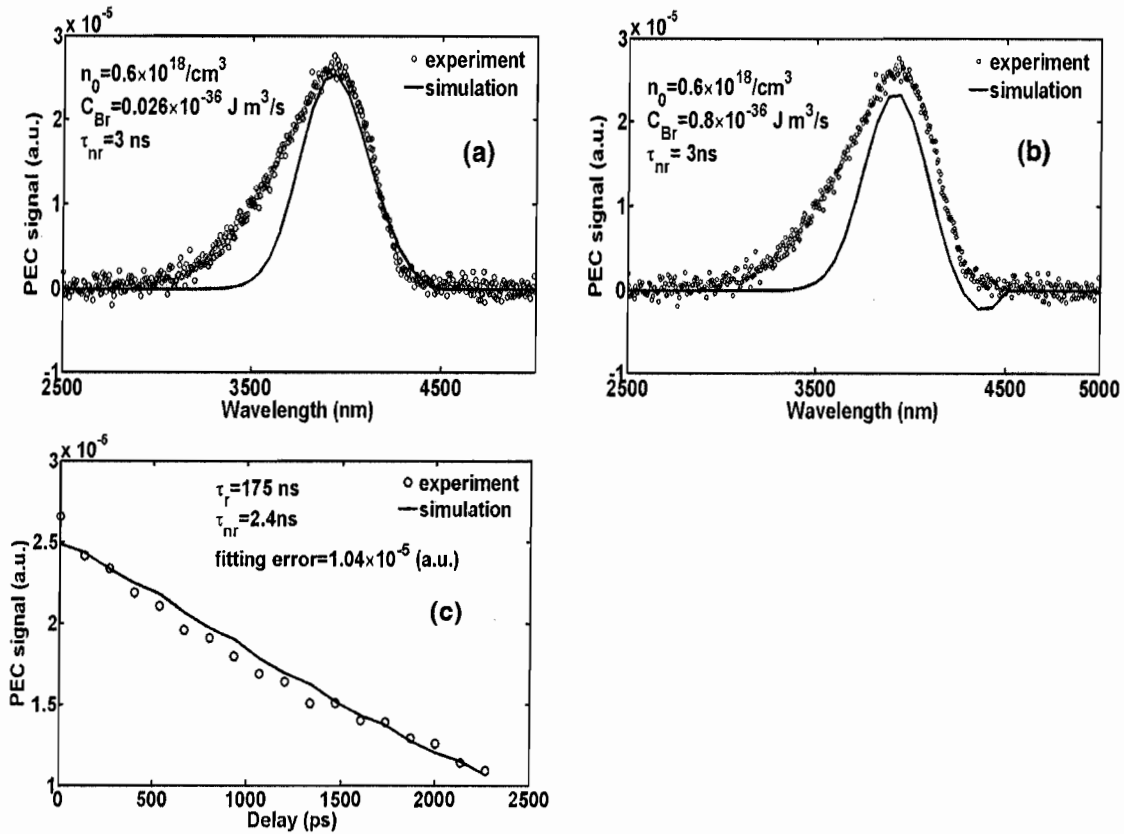


Figure 10. (a) The measured and simulated PEC spectrum that determined  $n_0=0.6 \times 10^{18} \text{ cm}^{-3}$ ; (b) the measured and simulated PEC spectrum that narrowed down the range of possible radiative recombination lifetime values; (c) the measured and simulated PEC signals as a function of delay.

The carrier lifetime in the wet-etched 8ML InAs/8ML GaSb SLS mesa photodiodes was determined to be at least 12 ns based on the PVD experimental result shown in Figure 8.

In PEC measurements, two trains of laser pulses, which are slightly delayed with respect to each other and are chopped at two different frequencies, create carriers that later recombine. Due to the nonlinear relation between the photoluminescence (PL) and the carrier population, the PL signal measured at the sum or difference frequency (PEC signal) gives the cross correlation of the photogenerated carriers. By measuring the PEC signal as a function of the delay between the pulses, information about the dynamics of the photogenerated carriers such as carrier lifetimes may be obtained.

The PEC signal spectrum and the PEC signal as a function of pulse delay obtained from an as-grown InAs/GaSb SLS are presented in Figure 9. We developed a general theoretical model that is capable of simulating the PEC signals obtained from any bulk semiconductor. As shown in Figure 10, fitting the measured and simulated PEC signals using this model determined the radiative and non-radiative recombination carrier lifetimes ( $\tau_r$  and  $\tau_{nr}$ ) of as-grown 8ML InAs/8ML GaSb SLSs to be in the range of 18 – 175 ns and 2.3 – 2.4 ns, respectively, indicating the dominance of non-radiative recombinations. InAs/Ga(In)Sb SLS carrier lifetime measurement results in the range of 0.13 ns – 6 ns have been reported in the literature [5-7].

### Surface passivation study

Currently, a limiting factor in the performance of mesa-type InAs/Ga(In)Sb SLS infrared photodetectors is undesirable surface effects. Common to all III-V semiconductors, the interface between the surface native oxides and the semiconductor has a high density of surface states located in the forbidden energy gap. These surface states cause a strong increase of surface tunneling and generation-recombination dark currents. They also assist non-radiative carrier recombination, thereby reducing carrier lifetimes and decreasing detector responsivity and detectivity. More importantly, on the etched sidewalls of an InAs/Ga(In)Sb SLS photodiode, chemical reactions on the GaSb surfaces exposed to air form an elemental Sb layer, which is conductive and causes large surface leakage current. Therefore, there is an urgent need to develop a reliable surface treatment that is able to reduce the surface native oxides and passivate the exposed clean semiconductor surface in InAs/Ga(In)Sb SLS photodiodes.

From PEC carrier lifetime measurements, we extracted  $\tau_{nr}$  of InAs/GaSb SLSs (with etched mesas) passivated in  $(\text{NH}_4)_2\text{S}$  solutions under various conditions (Table 1). The best passivation condition found in the PEC lifetime measurements was dipping the sample in  $(\text{NH}_4)_2\text{S}$  21%: $\text{H}_2\text{O}$ =1:4 for two hours, which increased the  $\tau_{nr}$  from 1.3 - 1.4 ns to 3.5 – 3.8 ns.

Table 1. Summary of samples used in the PEC carrier lifetime measurement for passivation study

Sample	Sample description	$\tau_{nr}$ (ns)
A	As-grown	2.3 - 2.4
B	Etched and unpassivated	1.3 - 1.4
C	Etched and passivated in $(\text{NH}_4)_2\text{S}$ 21% : water=1:4 for one hour	Not available
D	Etched and passivated in $(\text{NH}_4)_2\text{S}$ 21% : water=1:4 for two hours	3.5 – 3.8
E	Etched and passivated in $(\text{NH}_4)_2\text{S}$ 21% : water=1:6 for one hour	3.2 – 3.5
F	Etched and passivated in $(\text{NH}_4)_2\text{S}$ 21% : water=1:6 for two hours	1.2 – 1.3

Using the best  $(\text{NH}_4)_2\text{S}$  passivation solution found in the PEC lifetime measurements ( $(\text{NH}_4)_2\text{S}$  21%: $\text{H}_2\text{O}$ =1:4, 30 minutes), variable-area diode array (VADA) surface recombination velocity (SRV) measurements were undertaken to compare SRVs in unpassivated and passivated InAs/GaSb SLS diodes. The principle of the VADA technique is as follows. In a series of diodes of the same shape but different sizes, the performance of a diode of smaller area is more dependent on perimeter or surface effects and less dependent on bulk effects than a diode of larger area. By measuring device properties such as  $R_0A$  as a function of the diode size, surface-related effects can be separated from bulk properties.

The SRV of unpassivated and passivated InAs/GaSb SLSs at 77 K were determined from Figure 11(a) to be  $9.5 \times 10^5$  cm/s and  $4.0 \times 10^5$  cm/s, respectively. At 77 K the typical measured values of  $R_0A$  in the passivated devices were 2 – 2000  $\Omega \text{ cm}^2$  versus 0.05 – 0.2  $\Omega \text{ cm}^2$  for the unpassivated diodes. As shown in Figure 11(b), there was no change in the  $R_0A$  values of ammonium sulfide passivated InAs/GaSb SLS diodes measured 24 hours, 45 days and 120 days after the sulfidation, indicating long-term stability of the aqueous ammonium sulfide passivation.

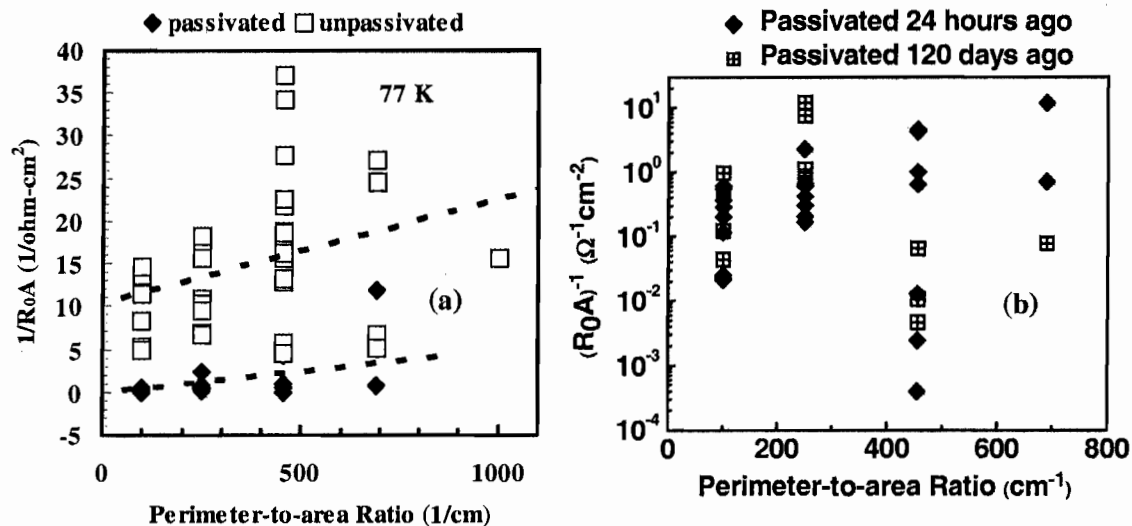


Figure 11 (a)  $1/R_0A$  versus the perimeter-to-area ratio ( $P/A$ ) of the passivated and the unpassivated SLS diodes; (b)  $1/R_0A$  versus  $P/A$  of the SLS diodes passivated 24 hours and 120 days ago.

## References

- [1] A. Rogalski and P. Martyniuk, *Infrared Physics and Technology* (2005)
- [2] M. Walther, R. Rehm, F. Fuchs, J. Schmitz, J. Fleißner, W. Cabanski, D. Eich, M. Finck, W. Rode, J. Wendler, R. Wollrab, and J. Ziegler, *Journal of Electronic Materials* **34**, 722 (2005).
- [3] Jean-Baptiste Rodriguez: *InAs/GaSb superlattices grown by molecular beam epitaxy for room-temperature detection in the 3-5  $\mu\text{m}$  wavelength range*, PhD thesis, CEM2, University of Montpellier II, France, 2005.
- [4] P. Bhattacharya, X. H. Su, S. Chakrabarti, G. Ariyawansa and A. G. U. Perera; *Applied Physics Letters* **86**, 191106 (2005).
- [5] I. H. Campbell, I. Sela, B. K. Laurich, and D. L. Smith, *Applied Physics Letters* **59**, 846 (1991)
- [6] E. R. Youngale, J. R. Meyer, C. A. Hoffman, F. J. Bartoli, and W.I. Wang, *International Journal of Nonlinear Optics Physics*, **2**, 415 (1993)
- [7] J. V. Li, S. L. Chuang, E. M. Jackson, E. Aifer, *Applied Physics Letters* **85**, 1984 (2004)

## 7. Interaction with ARO and Other DOD Personnel:

(Sivananthan/Grein)-

1. We have been collaborating closely with the Army Night Vision and Electronic Sensors Directorate (NVESD) (Dr. J.H. Dinan, Dr. L.A. Almeida, Dr. J. Markunas and Dr. S. Lewis) through the routine exchange of knowledge on the MBE growth of HgCdTe and through both *in situ* and *ex situ* characterization of MBE grown HgCdTe layers. This has led to several joint publications.
2. We have also been closely working with the Army Research Laboratory (Dr. N. Dhar, Dr. Wijewarnasuriya, Dr. G. Brill and Dr. Y. Chen) in the areas of MBE growth, characterization and detector fabrication. One of the goals of this collaboration is to establish standard HgCdTe-pertinent comprehensive databases that include information on material growth and characterization, and on detector fabrication and performance. We also have performed much characterization work on their samples to help them optimize their growth. This collaboration led to several joint publications.
3. We collaborated with the Air Force Research Laboratory (Dr. V. Nathan, Dr. S. Guha, Dr. L. Brown) in the areas of infrared absorption properties and of characterization, especially the optical characterization of HgCdTe. This collaboration also led to a joint publication.
4. We also conducted extensive collaboration with other DoD industrial contractors, such as DRS Technologies, Raytheon Vision Systems, Rockwell Scientific and BAE systems. This included personal contacts and seminars, joint publications and the exchange of HgCdTe samples. Some of the sample exchanges were arranged by Dr. J.H. Dinan of the Army Night Vision and Electronic Sensors Directorate and Dr. W. W. Clark of the Army Research Office.
5. MPL also sent internship students to work in DoD and related industrial research laboratories. Mr. Chad Fulk worked at ARL, NVESD, and BAE Systems; Mr. Ernest Robinson at NVESD, ARL and DRS Technologies; Miss Rajni Kiran at ARL; Miss Jennene Fields at ARL; Mr. Rasdip Singh at ARL; and Mr., Craig Lennon at ARL; among others.

(Wang)- Discussion with ARO and night vision laboratory personnel.

(Goldman)- Interactions with Night Vision Laboratory (NVL) in the area of UHV-XSTM studies of MCT-based IR detector structures have commenced. In collaboration with J.H. Dinan of NVL and M. Chu of Fermionics, we have made significant progress toward achieving this goal. For UHV-XSTM measurements, there are four factors which are critical for success: (1) the production of an atomically flat cleaved surface, (2) the ability to tunnel into that cleaved surface, (3) extreme chamber cleanliness and lack of sample oxidation made possible by UHV integrity, and (4) the ability to reliably position the tip over the interfaces of interest. To date, we have made several attempts to cleave a variety of CZT crystals, as summarized in Table I.

Sample Type	Orientation	Doping	Resistivity	Flat Cleave?	Tunneling?
CZT1	(100)	Undoped wafer	$\sim 5 \times 10^{10} \Omega\text{-cm}$	No	No
CZT2	(100)	Undoped strips	$\sim 5 \times 10^{10} \Omega\text{-cm}$	No	No
CZT3	(111)	$\sim 8 \times 10^{16} \text{cm}^{-3}$	$\sim 0.5 \Omega\text{-cm}$	Yes	No

Table I: Results of cleaving and scanning various CdZnTe samples. Several attempts were made of each sample type.

(Bhattacharya)-We have close collaboration with Drs. S. Kennerly and J. Little at ARL, who have immensely helped us to characterize our QDIPs. They have been extremely cooperative in allowing our graduate students visit ARL and participate in the measurements. In addition, we have collaborated with personnel at NASA-JPL (Drs. Sarath Gunapala and Sumith Bandara), who have characterized the QDIPs and personnel at Lockheed Martin (E. Braunstein), who are evaluating our devices for high temperature focal plane arrays.

*DoD/Government/University Collaboration:*

U. S. Army Research Laboratory – Adelphi, MD  
Night Vision Laboratory – Fort Belvoir, VA  
NASA Jet Propulsion Laboratory – Pasadena, CA  
National Institute of Standards and Technology – Boulder, CO  
Georgia State University  
University of New Mexico

*Industrial Collaboration:*

Northrup Grumman  
Rockwell International Science Center  
HRL Laboratories  
Texas Instruments/DRS Technologies  
EPIR Limited  
Lockheed Martin  
Santa Barbara Focalplane  
BAE Systems  
AFRL  
Wizdom Systems, Inc

**8. Technology Transfer/Initiatives:**

(Sivananthan/Grein)-We transferred technology and skills primarily by producing well-trained graduates of our doctoral program to work in DoD research laboratories and for DoD contractors. A new CdZnTe optical constant/dielectric function library with higher precision for *in situ* growth control has been collected and established in our laboratory and is available to our governmental and industrial co-workers. Computer software has also been distributed to DoD laboratories and contractors. Some of the ideas that we obtained from our MURI research, such as the use of interfacial layers, is being transferred to the MBE growth of novel heteroepitaxial systems and form the basis of new research proposals to be submitted to the ARO.

(Wang)-Working on detector design with Michigan group; Detector calibration. Transport of carriers from quantum dots with Michigan J. Singh's group. Discussing with JPL about the calibration.

(Singh)- Our models for k.p bandstructure have been transferred to other University groups (e.g Duke University)

(Goldman)-In May 2004, RSG visited Soitec, in Bernin, France, and discussed opportunities for collaborations which are of interest for the MURI. Both of these involve wafer bonding. One project involves the use of twist-bonded substrates for controlled nucleation of InAs/GaAs quantum dots for QDIPs. This approach will lead to greater control of QD sizes and densities, in order to further optimized QDIP performance. The other project involves using a new approach to materials synthesis and integration, termed, "ion-cut-synthesis". To date, we have applied this to the GaAsN system. In the future, this could be applied to the integration of MCT with silicon, similar to what was proposed in a recent report by T.D. Golding et al [1].

[1] T.D. Golding, O.W. Hollan, M.J. Kim, J.H. Dinan, L.A. Almeida, J.M. Arias, J. Bajaj, H.D. Shih, W.P. Kirk, J. Electron. Mat. **32**, 882 (2003).

(Bhattacharya)-We are working with Lockheed-Martin and Santa Barbara Focal Plane toward the characterization of 256x320 mid-IR FPAs. The arrays are fabricated at University of Michigan.

## **9. Report of Invention:**

(Sivananthan/Grein)- The concept of equivalent growth conditions and interfacial layers, and the technique of using the depolarization effects to evaluate the layer growth as well as using SE to precisely measure the growth temperature all are new inventions and have proven to be useful for enhancing the MBE growth yield.

(Wang)- Diblock copolymer nano-patterned substrates. High aspect ratio diblock copolymer nano-patterned substrates

(Goldman)- X. Weng and R.S. Goldman "Narrow energy band gap gallium arsenide nitride semi-conductors and an ion-cut-synthesis method for producing the same" U.S. Patent #7,056,815 (June 6, 2006).

(Bhattacharya)- The conception and demonstration of high-temperature tunnel QDIPs.

## **10. Scientific Personnel (Honors/Award/degrees received):**

(Sivananthan/Grein)- The training of new personnel in the field of MCT growth and characterization represents a crucial achievement for an academic institution such as MPL at UIC. Under the support of this project, in particular, 5 new PhD students have been trained in the fields of epitaxial growth, optical characterization and device fabrication. Also, several post-doctoral fellows have joined the related research works, enriching it with their experience and bringing much necessary dedication and effort.

### *Ph.D.s Graduates:*

(1) Mikhail Daraselia, - "In-situ ellipsometry monitoring of the MBE grown CdZnTe(211)B/Si(211) and CdTe(211)B/Si(211) structures", Jan 2003, currently working at Rockwell Scientific Company.

(2) Giacomo Badano – “Temperature-dependent adsorption of Te and Hg species on CdTe studied by spectroscopic ellipsometry”, June 2003.

(3) Yusuf Selamet, “HgCdTe heterojunction grown by molecular beam epitaxy for infrared detection applications: an in situ doping approach”, Jan. 2004.

(4) Rasdip Singh, “Researches of Oxygen and Silane with Hf and Zr Dioxide (0001) surfaces, Feb. 2006, currently working at EPIR Technologies

(5) Toshihiro Aoki, “Characterization of HgCdTe/CdZnTe(211)B Heterostructures and HgTe/HgCdTe Superlattices”, Dec. 2003, currently working at JEOL USA

M.S.:

(1) Dayna Grajewski – currently employed at Intel

(2) Abe Akhiyat - currently employed at Northrop Grumman

(3) Ernest Robinson – currently employed at DRS Technologies (Cypress)

(4) Dustin Guidry – currently employed at AFRL

(Smith)-

*Ph.D.s graduated:* Toshihiro Aoki

*Honors and Awards:* D.J. Smith

Elected Fellow, American Physical Society, 2002

Listed in ISI Highly Cited in Materials Science, 2003

(Wang)-

*Ph.D.s graduated (names):*

Ph.D.s graduated: Fei Liu – June 2006, currently employed at IBM

M.S. graduated: Christopher Chen – June, 2006, currently working at Altera

Ph.D.s graduated: Filipp Baron-March 2005, currently working at Willinx

Ph.D.s graduated: Jianlin Liu-March 2003, currently working at UCR

Post-Doctors: Song Tong- currently employed at Skyworks

Graduate students (Ph.D.): Dongho Cha, Masaki Ogawa, and Siguang Ma

*Honors and awards:*

TSMC Honor Lectureship (2004)

Honoris Causa, University Professor at Politecnico University, Torino, Italy (2005)

Honorary Professor at Tsinghua University and Nanjing University, China

(Singh)- Number of Ph.D.'s graduated in the MURI program in the last 5 years:

*Two students were graduated:*

Boaz Kochman (co-chair with Prof. P. Bhattacharya);

YihYin Lin

(Goldman)-

*PhDs Graduated:*

Dr. Xiaojun Weng

Dr. Matt Reason

*Honors/Awards:*

2002 Peter Mark Memorial Award, American Vacuum Society (presented to a young scientist or engineer for outstanding theoretical or experimental work)

Citation: "for contributions to the fundamental understanding of strain relaxation, alloy formation, diffusion, and the correlations among microstructure, electronic, and optical properties"

- 2004 Ted Kennedy Family Team Excellence Award, UM College of Engineering
- 2005-2006 Radcliffe Faculty Fellowship, Radcliffe Institute of Advanced Study, Harvard University
- 2005 UM Faculty Fellowship Enhancement Award

*Awards to students associated with the project:*

Jeff Gleason, Best Student Award, 2004 Electronic Materials Conference  
Scott Hanson (undergraduate student), Award Winner, 2004 Undergraduate Student Research Award, the AVS Science and Technology Society  
Scott Hanson (undergraduate student), 2004 Henry Ford II Prize, UM

(Norris)-

*PhD's Graduated:* Zong-kwei (John) Wu

*Honors and Awards:*

Fellow, American Physical Society, 2006.  
University of Michigan Faculty Recognition Award, 2004.  
College of Engineering Ted Kennedy Team Award, 2004.

(Bhattacharya)-

*PhDs Graduated:*

A. D. Stiff-Roberts  
X. H. Su  
Z. Zhu

*Honors and awards:*

Nicholas Holonyak, Jr. Award, Optical Society of America, 2002  
Quantum Devices Award, Fujitsu and International Symposium on Compound Semiconductors, 2003  
Fellow, Institute of Physics (UK), 2004  
Ted Kennedy Family Team Excellence Award, University of Michigan, College of Engineering, 2004  
Charles M. Vest Distinguished University Professor at the University of Michigan, 2004.  
Fellow, American Physical Society, 2005

## 11. List of Publications:

1. Yong Chang, J. Zhao, H. Abad, C. H. Grein, S. Sivananthan, T. Aoki, D. J. Smith, Performance and Reproducibility Enhancement of HgCdTe Molecular Beam Epitaxy Growth on CdZnTe Substrates Using Interfacial HgTe/CdTe Superlattice Layers, *Appl. Phys. Lett.*, 86, 131924(2005).
2. Yong Chang, Christoph H. Grein, Sivalingam Sivananthan, Michael Flatte, V. Nathan, S. Guha, Narrow Gap HgCdTe Absorption Behavior Near the Band Edge Including Nonparabolicity and the Urbach Tail, *Appl. Phys. Lett.*, 89, 062109(2006).
3. Y. Chang, G. Badano, J. Zhao, C. H. Grein, S. Sivananthan, T. Aoki, and David J. Smith, Formation Mechanism of Crater Defects on HgCdTe/CdZnTe (211)B Epilayers Grown by Molecular Beam Epitaxy, *Appl. Phys. Lett.*, 83, 4785(2003).
4. G. Badano, Y. Chang, J. W. Garland, and S. Sivananthan, Temperature-dependent adsorption of Hg on CdTe(211)B studied by spectroscopic ellipsometry, *Appl. Phys. Lett.*, 83, 2324(2003).
5. T. Aoki, D.J. Smith, Y. Chang, J. Zhao, G. Badano, C. Grein, and S. Sivananthan, Mercury cadmium telluride/tellurium intergrowths in HgCdTe epilayers grown by molecular-beam epitaxy, *Appl. Phys. Lett.*, 82, 2275(2003).
6. Yong Chang, G. Badano, E. Jiang, J. W. Garland, J. Zhao, C. H. Grein and, S. Sivananthan, Composition and Thickness Distribution of HgCdTe Molecular Beam Epitaxy Wafers By Infrared Microscope Mapping, *J. Crystal Growth*, 277, 78(2005).
7. T. Aoki, M. Takeguchi, P. Boieriu, R. Singh, C. Grein, Y. Chang, S. Sivananthan, D. J. Smith, Microstructural characterization of HgTe/HgCdTe superlattices, *J. Crystal Growth*, 271, 29(2004).
8. Changzhen Wang, David J. Smith, Steve Tobin, Themis Parodos, Jun Zhao, Yong Chang, and Sivalingam Sivananthan, Understanding ion-milling damage in Hg<sub>1-x</sub>Cd<sub>x</sub>Te epilayers, *J. Vac. Sci. Technol. A*24, 995(2006).
9. Changzhen Wang, Steve Tobin, Themis Parodos, and David J. Smith, "Investigation of HgCdTe p-n device structures grown by liquid-phase epitaxy", *J. Electron. Mat.* 35, 1192(2006).
10. G.A. Carini, C. Arnone, A.E. Bolotnikov, G.S. Camarda, R. De Wames, J.H. Dinan, J.K. Markunas, B. Raghathamachar, S. Sivananthan, R. Smith, J. Zhao, Z. Zhong, and R.B. James, Material Quality Characterization of CdZnTe Substrates for HgCdTe Epitaxy, *J. Electron. Mater.* 35, 1495(2006).
11. J. Zhao, Y. Chang, G. Badano, S. Sivananthan, J. Markunas, S. Lewis, J. H. Dinan, P. S. Wijewarnasuriya, Y. Chen, G. Brill and N. Dhar, Correlation of the CdZnTe(211)B substrate surface morphology and HgCdTe (211)B epilayer defects, *J. Electron. Mat.* 33,881(2004).
12. Yong Chang, G. Badano, J. Zhao, Y. D. Zhou, R. Ashokan, C. H. Grein and V. Nathan, Near Band Gap Infrared Absorption Properties of HgCdTe, *J. Electron. Mat.*, 33, 709(2004).
13. G. Badano, Y. Chang, J. W. Garland and S. Sivananthan, In-situ Ellipsometry Studies of Adsorption of Hg on CdTe(211)B/Si(211) and Molecular Beam Epitaxy Growth of HgCdTe(211)B, *J. Electron. Mat.*, 33, 583(2004).
14. Yong Chang, J. W. Garland and S. Sivananthan, Infrared optical characterization of the narrow gap semiconductor HgCdTe, in: *Adv. Mat. Electron.*, Edit by Q. X. Guo (Japan), Chapter 11249, 2004.
15. T. Aoki, David J. Smith, Y. Chang, J. Zhao, Y. Zhou, G. Badano, C. Grein, S. Sivananthan, HgCdTe/Te intergrowths and Precipitates in HgCdTe Alloys grown by Molecular Beam Epitaxy, *Microscopy and Microanalysis*, 9, 464(2003).
16. G. Badano, J. Zhao, Y. Chang, J. W. Garland, and Sivananthan, Ellipsometric study of the nucleation of (2 1 1) HgCdTe on CdZnTe(2 1 1)B, *J. Crystal Growth*, 258, 374(2003).
17. T. Aoki, Y. Chang, G. Badano, J. Zhao, C. Grein, S. Sivananthan, and David J. Smith, Electron microscopy of surface-crater defects on HgCdTe/CdZnTe(211)B epilayers grown by molecular-beam epitaxy, *J. Electron. Mat.*, 32, 703(2003).
18. Rajni Kiran, Shubhrangshu Mallick, Suk-Ryong Hahn, T.S.Lee, Sivalingam Sivananthan, Siddhartha Ghosh and P. S. Wijewarnasuriya, Passivation Effect on Optical and Electrical Properties of MBE Grown HgCdTe/CdTe/Si Layers, *J. Electron. Mat.*, 35, 1379(2006).

19. G. Badano, M. Daraselia and S. Sivananthan, "In situ monitoring of molecular-beam-epitaxy grown HgCdTe by Fourier transform infrared spectroscopy", *J. Vac. Sci. Technol. B* **19**, 1576(2001).
20. G. Badano, J.W. Garland and S. Sivananthan, "Accuracy of the in situ determination of the CdZnTe temperature by ellipsometry before the growth of HgCdTe by MBE", *J. Crystal Growth*, **251**, 571(2003).
21. M. Daraselia, J.W. Garland, B. Johs, V. Nathan, and S. Sivananthan, Improvement of the Accuracy of the In-situ Ellipsometric Measurement of Temperature and Alloy Composition for MBE Grown HgCdTe LWIR/MWIR Structures, *J. Electron. Mat.* **30**, 637(2001).
22. Y. Chang, C.H. Grein, J. Zhao, S. Sivananthan, C.Z. Wang, T. Aoki, D.J. Smith, P. Wijewarnasuriya and V. Nathan, Improve Molecular Beam Epitaxy Growth of HgCdTe on CdZnTe (211)B Substrates Using Interfacial Layers of HgTe/CdTe Superlattices, *J. Appl. Phys.*, in press.
23. Y. Chang, C. Fulk, J. Zhao, C.H. Grein and S. Sivananthan, Molecular Beam Epitaxy Growth of HgCdTe for High Performance Infrared Photon Detectors, *Infrared Phys. Tech.*, accepted.
24. T. Aoki, D.J. Smith, Y. Chang, J. Zhao, G. Badano, C. Grein, and S. Sivananthan, Mercury cadmium telluride/tellurium intergrowths in HgCdTe epilayers grown by molecular-beam epitaxy, *Appl. Phys. Lett.* **82**, 2275 (2003).
25. T. Aoki, Y. Chang, J. Zhao, G. Badano, C. Grein, S. Sivananthan, and D.J. Smith, Electron microscopy of surface-crater defects on HgCdTe/CdZnTe(211)B epilayers grown by molecular-beam epitaxy, *J. Electronic Mater.* **32**, 703 (2003).
26. T. Aoki, Y. Chang, G. Badano, J. Zhao, C. Grein, S. Sivananthan, and D.J. Smith, "Defect characterization for epitaxial HgCdTe alloys by electron microscopy", *J. Cryst. Growth*, **265**, 224 (2004).
27. C. Wang, D.J. Smith, S. Tobin, T. Parodos, J. Zhao, Y. Chang, and S. Sivananthan, "Understanding ion-milling damage in Hg<sub>1-x</sub>Cd<sub>x</sub>Te epilayers, *J. Vac. Sci. Technol. A* **24**, 995 (2006).
28. C. Wang, S. Tobin, T. Parodos, and D.J. Smith, "Investigation of HgCdTe p-n device structures grown by liquid-phase epitaxy, *J. Electronic Materials*, **35**, 1192 (2006).
29. Xie YH, Zhao ZM, Yoon TS, Feng W, Li BY, Kim JH, Liu J, Hulko O, Kim HM, Kim KB, Kim HJ, Wang KL, Ratsch C, Caflisch R, Ryu DY, Russell TP, "The challenges in guided self-assembly of Ge and InAs quantum dots on Si", *Thin Solid Films*, vol.508, no.1-2, 5 June 2006, pp. 195-9. Publisher: Elsevier, Switzerland.
30. Liu, J.L., Yang, Z, Wang, K.L., "Sb surfactant-mediated SiGe graded layers for Ge photodiodes integrated on Si", *Journal of Applied Physics*, vol.99, no.2, 15 Jan. 2006, pp. 24504-1-8. Publisher: AIP, USA.
31. Liu, J.L., Tong, S., Wang, K.L., "Self-Assembled Germanium Quantum Dots on Silicon and Their Optoelectronic Devices", *Handbook of Semiconductor Nanostructures and Nanodevices*, American Scientific Publishers, Vol.1, pp,1-32, 2006.
32. Tong, S., Hyung-Jun Kim, Wang, K.L., "Normal incidence intersubband photoresponse from phosphorus doped Ge dots", *Applied Physics Letters*, vol. 87, no. 8, pp. 81104-1-3, August 22, 2005. Publisher: AIP, USA.
33. Wang, K.L., S. Tong, and H.J. Kim, "Properties and applications of SiGe nanodots," *Materials Science in Semiconductor Processing*, Vol 8., no. 1-3, pp 289-399, Feb-June 2005. Publisher: Elsevier, UK.
34. Liu, F., Wang, K.L., "Low radiation temperature thermal photovoltaic cell", *J. Appl. Phys.* **97**, 044910-1~044910-6, February 15, 2005
35. Tong, S., Lee, J.Y., Kim, H.J., Liu, F., Wang, K.L., "Ge dot mid-infrared photodetectors", *Optical Materials*, vol. 27, no. 3-4, pp. 1097~1100, February 2005. Publisher: Elsevier, Netherlands.
36. Liu, F., Tong, S., Kim, H.J., Wang, K.L., "Photoconductive gain of SiGe/Si quantum well photodetectors," *Optical Materials*, Vol 27, pp 864-867, February 2005. Publisher: Elsevier, Netherlands.

37. Liu, J.L., Wang, K.L., Xie, Q.H., Thomas, S.G., "The effect of plastic strain relaxation on the morphology of Ge quantum dot superlattices," *Journal of Crystal Growth*, vol. 274, no. 3-4, pp. 367-71, February 1, 2005. Publisher: Elsevier, Netherlands.
38. Liu, J.L., Wang, K.L., Xie, Q.H., and Thomas, S.G., "The effect of plastic strain relaxation on the morphology of Ge quantum dot superlattices", *Journal of Crystal Growth*, vol. 274, no. 3-4, pp. 367-71, January 2, 2005.
39. Liu, F., Tong, S., Kim, H.J., Wang, K.L., "Photoconductive gain of Si-Ge/Si quantum well photodetectors", *Optical Materials*, 27, pp. 864-867, (2005).
40. Song, T., Fei, L., Khitun, A., Wang, K.L., Liu, J.L. "Tunable normal incidence Ge quantum dot midinfrared detectors". *Journal of Applied Physics*, vol.96, no.1, 1 July 2004, pp.773-6. Publisher: AIP, USA.
41. Jin, G., Liu, J.L., Wang, K.L., "Temperature Effect on the Formation of Uniform Self-Assembled Ge Dots", *Applied Physics Letters*, 83(14), pp. 2847-2849, October 2003.
42. Liu, J.L., Wan, J., Wang, K.L., Yu, D.P., "Critical Thickness of Self-Assembled Ge Quantum Dot Superlattices", *Journal of Crystal Growth*, 251 (1-4), pp. 666-669, April 2003.
43. Liu, J.L., Khitun, A., Wang, K.L., Liu, W.L., Chen, G., Xie, Q.H., Thomas, S.G., "Cross-Plane Thermal Conductivity of Self-Assembled Ge Quantum Dot Superlattices", *Physical Review B – Condensed Matter*, 67(16), 165333-1-6, April 2003.
44. Liu, J. L., Tong, S., Wang, K.L., "Molecular Beam Epitaxy Growth of Ge Detectors on Si Using Sb Surfactant-mediated Graded SiGe Buffers," *ICS13 Third International Conference on SiGe Epitaxy and Heterostructures*, March 2003.
45. Tong, S., Liu, J.L., Wang, K.L., "Ge Quantum Dot Light Emitting Diodes and Photodetectors," *ICS13 Third International Conference on SiGe Epitaxy and Heterostructures*, March 2003.
46. Liu, J.L., Wan, J., Jiang, Z.M., Khitun, A., Wang, K.L., Yu, D.P., "Optical Phonons in Self-Assembled Ge Quantum Dot Superlattices: Strain Relaxation Effects" *Journal of Applied Physics*, 92(11):6804 - 6808 (December 2002).
47. Tong, S., Liu, J.L., Wan, J., Wang, K.L., "Normal-Incidence Ge Quantum-Dot Photodetectors at 1.5  $\mu$ m Based on Si Substrate" *Applied Physics Letters*, 80(7):1189 - 1191 (February 2002).
48. Wang, K.L., Liu, J.L., Jin, G., "Self-Assembled Ge Quantum Dots on Si and Their Applications" *Journal of Crystal Growth*, 237-239:1892 - 1897 (2002).
49. Liu, J.L., Tong, S., Luo, Y.H., Wan, J., Wang, K.L., "High-Quality Ge Films on Si Substrates Using Sb Surfactant-Mediated Graded SiGe Buffers" *Applied Physics Letters*, 79(21):3431 - 3433 (November 2001).
50. Wan, J., Luo, Y.H., Jiang, Z.M., Lin, G., Liu, J.L., Wang, K.L., Liao, X.Z., Zou, J., "Ge/Si Interdiffusion in the GeSi Dots and Wetting Layers" *Journal of Applied Physics*, 90(8):4290 - 4292 (October 2001).
51. Wan, J., Luo, Y.H., Jiang, Z.M., Jin, G., Liu, J.L., Wang, K.L., Liao, X.Z., Zou, J., "Effects of Interdiffusion on the Band Alignments of GeSi Dots" *Applied Physics Letters*, 79(13):1980 - 1982 (September 2001).
52. Jin, G., Wan, J., Luo, Y.H., Liu, J.L., Wang, K.L., "Uniform and Ordered Self-Assembled Ge Dots on Patterned Si Substrates with Selectively Epitaxial Growth Technique" *Journal of Crystal Growth*, 227-228:1100 - 1105 (July 2001).
53. Krapf, D., Adoram, B., Shappir, J., Sa'ar, A., Thomas, S.G., Liu, J.L., Wang, K.L., "Infrared Multispectral Detection Using Si/Si<sub>x</sub>Ge<sub>1-x</sub> Quantum Well Infrared Photodetectors" *Applied Physics Letters*, 78(4):495 - 497 (January 2001).
54. Luo, Y.H., Wan, J., Forrest, R.L., Liu, J.L., Jin, G., Goorsky, M.S., Wang, K.L., "Compliant Effect of Low-Temperature Si Buffer for SiGe Growth" *Applied Physics Letters*, 78(4):454 - 456 (01/22/2001).
55. Jin, G., Liu, J.L., Luo, Y.H., Wang, K.L., "Cooperative Arrangement of Self-Assembled Ge Dots on Pre-Grown Si Mesas" *Thin Solid Films*, 380(1-2):169 - 172 (December 2000).

56. Jin, G., Liu, J.L., Luo, Y.H., Wang, K.L., "Control of the Arrangement of Self-Organized Ge Dots on Patterned Si(001) Substrates" *Thin Solid Films*, 369(1-2):49 - 54 (July 2000).
57. Yih-Yin Lin and Jasprit Singh, Self-assembled quantum dots: A study of strain energy and intersubband transitions, *Journal of Applied Physics* Vol. 92 (10), pp.-6205-6210 Nov. 15 2002.
58. B. Kockman, S.Ghosh, J.Singh and P. Bhattacharya, In-Plane velocity-field characteristics of InAs self-assembled quantum dot layers, *Electronics Letters*, vol. 38, pp. 752-753, 2002.
59. Lateral hopping conductivity and large negative magnetoresistance in InAs/AlGaAs self-organized quantum dots, *Rapid Communications, J. Physics D*, vol. 35 L65-L68, 2002.
60. A Theoretical Study of Structural Disorder and Photoluminescence Linewidth in InGaAs/GaAs Self Assembled Quantum Dots, Y. Lin and J. Singh, *MRS Proceedings Volume 692: H3.4*, Boston, November, 2002.
61. Yih Yon Lin and Jasprit Singh, Theory of polarization dependent intersubband transitions in p-type SiGe/Si self assembled quantum dots, *Journal of Applied Physics*, 96, 1059 (2004).
62. R.S. Goldman, "Characterization of Interfaces by Cross-Sectional Scanning Tunneling Microscopy", *Encyclopedia of Materials Science and Technology*, Elsevier Press (2001).
63. B. Shin, A. Lin, K. Lappo, R.S. Goldman, M.C. Hanna, S. Francoeur, A.G. Norman, A. Mascarenhas, "Initiation and Evolution of Phase Separation in Heteroepitaxial InAlAs Films", *Appl. Phys. Lett.*, **80**, 3292 (2002).
64. B. Shin, B. Lita, R.S. Goldman, J. Phillips, and P.K. Bhattacharya, "In-In Pair Correlations within the wetting layers of buried InAs/GaAs quantum dots", *Appl. Phys. Lett.* **81**, 1424 (2002).
65. R.S. Goldman, B. Shin, and B. Lita, "Mechanisms of Semiconductor Nanostructure Formation", *Physica Status Solidi A* **195**, 151 (2003).
66. W. Chen, B. Shin, R.S. Goldman, A. Stiff, and P.K. Bhattacharya, "Mechanisms of Lateral Ordering of InAs/GaAs Quantum Dot Superlattices", *J. Vac. Sci. Technol. B* **21**, 1920 (2003).
67. B. Shin, W. Chen, R.S. Goldman, J.D. Song, J.M. Kim, and Y.T. Lee, "Initiation and Evolution of Phase Separation in GaP/InP Short-Period Superlattices", *J. Vac. Sci. Technol. B* **22**, 216 (2004).
68. R.S. Goldman, "Nanoprobing of Semiconductor Heterointerfaces: Quantum Dots, Alloys, and Diffusion", *Invited Topical Review for J. Phys. D*. 37, R163 (2004).
69. J.N. Gleason, M. Hjelmstad, V.D. Dasika, R.S. Goldman, S. Fathpour, S. Charkrabarti, and P.K. Bhattacharya, "Nanometer-scale Studies of Point Defect Distributions in GaMnAs Alloys", *Appl. Phys. Lett.* **86**, 011911 (2005).
70. W. Ye, S. Hanson, X. Weng, and R.S. Goldman, "Control of InAs/GaAs Quantum Dot Density and Alignment using Modified Buffer Layers", *J. Vac. Sci. Technol. B* **23**, 1736 (2005).
71. Jun-Qiang Lu, H. T. Johnson, V. D. Dasika, and R. S. Goldman, "Moments-based tight-binding analysis of local electronic structure in InAs/GaAs quantum dots," *Appl. Phys. Lett.* **85**, 053109 (2006).
72. V. Dasika, J.N. Gleason, J.D. Song, and R.S. Goldman, "Scanning Tunneling Spectroscopy Studies of InAs/GaAs Quantum Dots", in preparation (2006).
73. T.B. Norris, K. Kim, J. Urayama, J. Wu, J. Singh, and P.K. Bhattacharya "Density and temperature dependence of carrier dynamics in self-organized InGaAs quantum dots," *J. Phys. D* **38**, 2077 (2005), Special Issue on Quantum Dots (invited paper).
74. K. Kim, T.B. Norris, J. Singh, and P. Bhattacharya, "Level Degeneracy and Temperature-Dependent Carrier Distributions in Self-Organized Quantum Dots," *Appl. Phys. Lett.* **82**, 1959 (2003).
75. Z.-K. Wu, H. Choi, T. Norris, S. Chakraborti, X. Su, and P. Bhattacharya, "Time-Resolved Electron Dynamics in N-Doped Quantum Dot Infrared Detector Structures," manuscript in preparation (for submission to *J. Quant. Electron.*)
76. A.D. Stiff, S. Krishna, P. Bhattacharya, and S. Kennerly, "Low-Bias, High-Temperature Performance of a Normal-Incidence InAs/GaAs Vertical Quantum Dot Infrared Photodetector with a Current-Blocking Barrier", *Journal Vacuum Science Technology B*, **20**, 1185, 2002.
77. S. Krishna, A.D. Stiff-Roberts, J.D. Phillips, P. Bhattacharya, and S.K. Kennerly, "Hot Dot Detectors", *IEEE Circuits and Devices*, **18**, 14, (2002).

78. B. Kochman, S. Ghosh, J. Singh and P. Bhattacharya, "In-Plane Velocity-Field Characteristics of InAs Self-Assembled Quantum Dot Layers", *Electronics Letters*, **38**, 752, 2002.
79. B. Kochman, A.D. Stiff-Roberts, J.D. Phillips, S. Krishna, and P. Bhattacharya, "Absorption, Carrier Lifetime and Gain in InAs/GaAs Quantum Dot Infrared Photodetectors", *Journal of Quantum Electronics*, **39**, 459, 2003.
80. P. Bhattacharya, S. Ghosh, S. Pradhan, J. Singh, Z-K. Wu, J. Urayama, K. Kim and T. Norris, "Carrier Dynamics and High-speed Modulation Properties of Tunnel Injection InGaAs/GaAs Quantum Dot Lasers", *IEEE Journal of Quantum Electronics*, **39**, 952, 2003.
81. "Quantum Dot Long-Wavelength Detectors", P. Bhattacharya, A.D. Stiff-Roberts, S. Krishna, and S. Kennerly, *Material Research Society Symposium Proceedings*, **692**, 109, 2002.
82. B. Kochman, A.D. Stiff-Roberts, S. Chakrabarti, J.D. Phillips, S. Krishna, J. Singh, and P. Bhattacharya, "Absorption, Carrier Lifetime, and Gain in InAs-GaAs Quantum Dot Infrared Photodetectors", *IEEE J. of Quantum Electronics*, **39**, 459 2003.
83. K. Stewart, M. Buda, J. Wong-Leung, L. Fu, C. Jagadish, A. Stiff-Roberts, and P. Bhattacharya, "Influence of Rapid Thermal Annealing on a 30-Stack InAs/GaAs Quantum Dot Infrared Photodetector", *Journal of Applied Physics*, **94**, 5283, 2003.
84. S. Chakrabarti, P. Bhattacharya, A.D. Stiff-Roberts, Y.Y. Lin, J. Singh, Y. Lei and N. Browning, "Intersubband Absorption in Annealed InAs/GaAs Quantum Dots: A Case for Polarization-Sensitive Infrared Detection", *J. of Physics D*, **36**, 1794, 2003.
85. P. Bhattacharya, A.D. Stiff-Roberts, S. Krishna, and S. Kennerly, "Quantum Dot Infrared Detectors and Sources", *International Journal of High Speed Electronics and Systems*, **12**, 969, 2003.
86. A.D. Stiff-Roberts, X.H. Su, S. Chakrabarti, and P. Bhattacharya, "Contribution of Field-Assisted Tunneling Emission to Dark Current in InAs/GaAs Quantum Dot Infrared Photodetectors", *IEEE Photonics Technology Letters*, **16**, 867, 2004.
87. S. Chakrabarti, S. Fathpour, K. Moazzami, J. Phillips, Y. Lei, N. Browning and P. Bhattacharya, "Pulsed Laser Annealing of Self-Organized InAs/GaAs Quantum Dots", *Journal of Electronic Materials*, **33**, 382, 2004.
88. S. Chakrabarti, A.D. Stiff-Roberts, P. Bhattacharya, S. Gunapala, S. Bandara, S.B. Rafol and S.W. Kennerly, "High-Temperature Operation of InAs/GaAs Quantum Dot Infrared Photodetector with Large Responsivity and Detectivity", *IEEE Photonics Technology Letters*, **16**, 1361, 2004.
89. S. Chakrabarti, A.D. Stiff-Roberts, P. Bhattacharya, and S.W. Kennerly, "Heterostructures for Achieving Very Large Responsivity in InAs/GaAs Quantum Dot Infrared Photodetectors", *Journal of Vacuum Science and Technology (B)*, **3**, 1499, 2004.
90. S. Chakrabarti, A.D. Stiff-Roberts, P. Bhattacharya, and S.W. Kennerly. "High Responsivity AlAs/InAs/GaAs Superlattice Quantum Dot Infrared Photodetector", *Electronics Letters*, **40**, 197, 2004.
91. X. H. Su, S. Chakrabarti, A.D. Stiff-Roberts, J. Singh and P. Bhattacharya, "Quantum Dot Infrared Photodetector Design Based on Double-Barrier Resonant Tunneling", *Electronics Letters*, **40**, 1082, 2004.
92. J. Phillips, A.D. Stiff-Roberts, and P. Bhattacharya, "Quantum Dot Infrared Photodetector", *Encyclopedia of Nanoscience and Nanotechnology*, (ed. H.S. Nalwa), American Scientific Publishers, vol. 9, pp. 131-141, 2004.
93. S. Chakrabarti, X.H. Su, P. Bhattacharya, G. Ariyawansa and A.G.U. Perera, "Characteristics of a Multi-Color InGaAs/GaAs Quantum Dot Infrared Photodetector", *Photonics Technology Letters*, **17**, 178, 2005.
94. "Characteristics of a Tunneling Quantum Dot Infrared Photodetector Operating at Room Temperature", *Applied Physics Letters*, **86**, 191106-1, 2005.
95. X.H. Su, S. Chakrabarti, P. Bhattacharya, G. Ariyawansa and A.G.U. Perera, "A Resonant Tunneling Quantum Dot Infrared Photodetector", *IEEE Journal of Quantum Electronics*, **41**, 974 2005.

96. S. Chakrabarti, A.D. Stiff-Roberts, X.H. Su, P. Bhattacharya, G. Ariyawansa and A.G.U. Perera, "High-performance Mid-infrared Quantum Dot Infrared Photodetectors", *Journal of Physics D: Applied Physics*, **38**, 2135, 2005.
97. X.H. Su, J. Yang, P. Bhattacharya, G. Ariyawansa, and A.G.U. Perera, "Terahertz Detection with Tunneling Quantum Dot Intersublevel Photodetectors", *Applied Physics Letters*, **86**, 031117-1, 2006.
98. Z. M. Zhu, P. Bhattacharya, E. Plis, X. H. Su, and S. Krishna, "Low dark current InAs/GaSb type-II superlattice infrared photodetectors with resonant tunneling filters", submitted to *Journal of Physics D*, 2006.

## 12. Invited and Plenary Talks:

(Sivananthan/Grein):

1. G. Badano, "Characterization of MBE-Grown HgCdTe/CdZnTe (211)B Alloy by in-situ Ellipsometry and ex-situ FTIR Spectroscopy", 3rd Int. Symposium on "Quantum Functional Systems"-ISQFS 2003, Fremantle, WA, Australia, Sept. 5-6, 2003.
2. G. Badano, H. Abad, S. Sivananthan, D. J Smith, R. Sporcken, N. Dhar, G. Brill, Y. Chen, "Growth of HgCdTe/CdTe/Si by Molecular Beam Epitaxy", Proceedings of the International Workshop on Crystal Growth and Characterization of Technologically Important Materials, Feb. 24-28, 2004, Anna University, Chennai, India.
3. S. Sivananthan, "Molecular Beam Epitaxy Growth of HgCdTe for Advanced Infrared Detectors and Emitters", The 4th International Symposium on Quantum Functional Structures, Korea, 2004.
4. A. K. Sood, S. A. Jamison, N. K. Dhar, R. G. Driggers, R. S. Balcerak, S. Sivanathan, J. R. Buss, PANEL DISCUSSION, Use of EO/IR technology systems for border security, Optics and Photonics in Global Homeland Security 2003, SPIE International Workshop, Dec. 3-4, Washington, DC, USA.
5. S. Sivananthan, C.H. Grein, P. S. Wijewarnasuriya, "Present Status of HgCdTe Material and Detectors and its Future Directions", QWIP2006 International Workshop on Quantum Well Infrared Photo detectors, June 18-24, 2006 Kandy Sri Lanka.
6. S. Sivananthan, C. Fulk, "Status of compliant technologies for HgCdTe heteroepitaxy on Si", ICCE-14 July 2-8, 2006 in Boulder, Colorado, USA.

(Bhattacharya):

1. P. Bhattacharya, S. Krishna, and A. Stiff, "Quantum Dot Intersubband Devices" (INVITED), 2001 *International Conference on Solid State Devices and Materials*, Tokyo, September 2001.
2. P. Bhattacharya, S. Krishna, and A. Stiff, "Quantum Dot Long Wavelength Detectors", (INVITED), *Materials Research Society's 2001 Fall Meeting*, Boston, November 2001.
3. P. Bhattacharya, A.D. Stiff, S. Krishna and S. Kennerly, "Quantum Dot Infrared Photodetectors", (INVITED), *SPIE Photonics West*, San Jose, CA, January 2002.
4. "Carrier Dynamics in Self-Organized Quantum Dots and Their Application to Infrared Detectors and Sources", (INVITED) *American Physical Society Meeting*, Austin, TX, March 2003.
5. "Quantum Dot Optoelectronic Devices", (INVITED), *Nanomaterials For Defense Applications Symposium*, Maui, HI February 2004.
6. "Quantum Dot Photodetectors" (INVITED), *Military Sensing Symposia*, Tucson, AZ, March 2004.
7. "Self-Organized Semiconductor Quantum Dots and Their Application to Optoelectronic Devices", (KEYNOTE), *Great Lakes Photonics Symposium*, Cleveland, OH, June 2004.
8. "Quantum Dot Lasers and Detectors Using Tunneling of Carriers", (INVITED), *International Symposium on Quantum Dots and Photonic Crystals*, Tokyo, Japan, March 2005.
9. "In(Ga)As/Ga(Al)As Self-Organized Quantum Dots and Their Device Applications", *16<sup>th</sup> American Conference on Crystal Growth and Epitaxy*, Big Sky Montana, July 2005.
10. "Quantum Dot Infrared Detectors", (INVITED), *US Workshop on the Physics and Chemistry of II-VI Materials*, Cambridge, MA, September 2005.

11. "Tunnel Quantum Dot Infrared Detectors for High Temperature Applications", (INVITED), P. Bhattacharya, *2nd Symposium on Infrared Materials and Technologies*, State College, PA, November 2005.
12. "Quantum Dot Infrared Photodetectors", (INVITED), P. Bhattacharya, *IEEE-LEOS Summer Topical Meeting*, Quebec City, Canada, July 2006.
13. "High Performance Quantum Dot Optoelectronic Devices", (INVITED), P. Bhattacharya, *Annual Meeting of the Optical Society of America*, Rochester, NY, October 2006.

(Goldman):

- 5/24/01 American Vacuum Society, New Mexico Annual Symposium, Albuquerque, New Mexico
- 7/3/01 International Conference on Materials for Advanced Technologies, Symposium H, Singapore
- 7/5/01 International Conference on Materials for Advanced Technologies, Symposium O, Singapore
- 10/8/01 International Narrow Gap Nitride Workshop, Singapore
- 5/26/02 EXMATEC 2002, Budapest, Hungary
- 11/6/02 Peter Mark Memorial Award Lecture, AVS International Symposium, Denver CO
- 12/5/02 Symposium W, Materials Research Society Fall Meeting, Boston, MA
- 1/29/03 SPIE 2003 International Symposium (Photonics West), San Jose, CA
- 6/17/03 ASME Summer Meeting of the Applied Mechanics and Materials Division, Scottsdale, AZ
- 6/22/03 Gordon Research Conference, Mount Holyoke College, Mt. Holyoke, MA
- 8/25/03 ASTATPHYS-MEX-003, Puerto Vallerto, Mexico
- 9/19/03 American Vacuum Society, Pacific Northwest Chapter Annual Symposium, Portland, Oregon
- 12/9/03 International Conference on Materials for Advanced Technologies (ICMAT), Singapore
- 1/19/04 Upgraded Talk, Physics and Chemistry of Semiconductor Interfaces Conference, Kona, Hawaii
- 5/19/04 First U.S.-China Workshop on Nanotechnology Forum, Beijing, China
- 7/26/04 International Conference on Computational & Experimental Engineering & Science, Madeira Island, Portugal
- 8/17/04 NSF-NIST Workshop on Nanotechnology, Boulder, CO
- 9/13/04 Nano and Giga Challenges in Microelectronics Meeting, Crakow, Poland
- 1/24/05 Conference on the Physics and Chemistry of Semiconductor Interfaces, Bozeman, Montana
- 2/22/05 WOCSEMAD, Miami, Florida
- 3/23/05 March Meeting of the American Physical Society, Los Angeles, CA
- 6/27/05 Gordon Conference on "Thin Films & Crystal Growth Mechanisms", Mt. Holyoke College, MA
- 12/3/05 International Conference on Computational and Experimental Engineering and Science, Chennai, India
- 12/14/05 Radcliffe Fellow Seminar, Radcliffe Institute of Advanced Study, Harvard University, Cambridge, MA
- 2/19/06 WOCSEMMAD, Tempe, AZ (cancelled due to surgery on 2/21/06)

### 13. Contributed Conference Presentations

1. Yih-Yin Lin and Jasprit Singh, Self organized quantum dots: A study of strain energy and electronic spectrum, Y. Lin, A Theoretical Study of Self Assembled InAs/GaAs and InAs/GaP/GaAs Quantum Dots: Effects of Strain Balancing, American Physical Society, March Meeting, Indianapolis, IN, March 18-22, 2002.
2. P. Bhattacharya, . Norris and J. Singh, Carrier Dynamics in InGaAs/GaAlAs self-organized quantum dots, Invited paper at Photonics West 2002.
3. Y. Lin, H. Jiang and J. Singh, Self organized quantum dots: A study of strain energy and electronic spectrum, presented at the Material Research Society Conference, November, 2001, Boston.

4. A. Yadav, K. P. Pipe, W. Ye, and R. S. Goldman, "In-plane thermoelectric properties of horizontally aligned InAs/GaAs quantum dot superlattices", International Mechanical Engineering Congress & Exposition, Chicago, IL (November 2006).
5. Jun-Qiang Lu, H. T. Johnson, V. D. Dasika, and R. S. Goldman, "Comparison of atomistic and continuum calculations with experimental measurements of strain and local electronic structure in InAs/GaAs quantum dots", Society of Engineering Science Meeting, State College, PA (August 2006).
6. A. Yadav, K.P. Pipe, W. Ye, and R.S. Goldman, "Thermoelectric Properties of Vertically Aligned InAs/GaAs Quantum Dot Superlattices", Oral Presentation, Electronic Materials Conference, State College, PA (June 2006).
7. Jun-Qiang Lu, H. T. Johnson, V. D. Dasika, and R. S. Goldman, "Moments-method tight-binding analysis of InAs quantum dots with realistic disorder", Oral Presentation, Fall Meeting of the MRS, Boston, MA (December 2005).
8. W. Ye, X. Weng, M. Reason, and R.S. Goldman, "Control of InAs/GaAs Quantum Dot Density and Positioning Using Modified Buffer Layers", oral presentation at the AVS International Meeting, Boston MA (November 2005).
9. W. Ye, X. Weng, M. Reason, R.S. Goldman, F. Watanabe, and D.G. Cahill, "Control of InAs/GaAs Quantum Dot Positioning via Surface Patterning", oral presentation at the Electronic Materials Conference (June 2005).
10. V. Dasika, R.S. Goldman, and J.D. Song, "Cross-Sectional Scanning Tunneling Microscopy and Spectroscopy of Confined States in InAs/GaAs Quantum Dots", oral presentation at the Electronic Materials Conference (June 2005).
11. W. Ye, M. Reason, X. Weng, and R.S. Goldman, "Buffer Layer Patterning of InAs/GaAs Quantum Dot Superlattices", oral presentation at the American Physical Society Meeting (March 2005).
12. W. Ye, M. Reason, X. Weng, and R.S. Goldman, "Buffer Layer Patterning of InAs/GaAs Quantum Dot Superlattices", oral and poster presentations at the Physics and Chemistry of Semiconductor Interfaces Meeting, Bozeman, MT (January 2005).
13. W. Ye, M. Reason, X. Weng, and R.S. Goldman, "Buffer Layer Patterning of InAs/GaAs Quantum Dot Superlattices", oral presentation at the Materials Research Society Meeting (November 2004).
14. J.N. Gleason, M.E. Hjelmstad, V.D. Dasika, S. Fathpour, S. Charkrabarti, P.K. Bhattacharya, and R.S. Goldman, "Nanometer-Scale Studies of Point Defect Distributions in GaMnAs Films", oral presentation at the Gordon Research Conference on Defects in Semiconductors (July 2004).
15. J.N. Gleason, M.E. Hjelmstad, V.D. Dasika, S. Fathpour, S. Charkrabarti, P.K. Bhattacharya, and R.S. Goldman, "Nanometer-Scale Studies of Point Defect Distributions in GaMnAs Films", oral presentation at the Electronic Materials Conference (June 2004).
16. J.N. Gleason, M.E. Hjelmstad, V.D. Dasika, S. Fathpour, S. Charkrabarti, P.K. Bhattacharya, and R.S. Goldman, "Nanometer-Scale Studies of Point Defect Distributions in GaMnAs Films", Poster Presentation at AVS-MI Spring Symposium, May 2004.
17. W. Ye, M. Reason, X. Weng, and R.S. Goldman, "Effects of Buffer Layer Patterning on Lateral Ordering of InAs/GaAs Quantum Dot Superlattices", Poster Presentation at AVS-MI Spring Symposium, May 2004.
18. J.N. Gleason, M.E. Hjelmstad, V.D. Dasika, S. Fathpour, S. Charkrabarti, P.K. Bhattacharya, and R.S. Goldman, "Cross-Sectional Scanning Tunneling Microscopy Studies of Mn Segregation in GaMnAs Films", Upgraded Oral Presentation at the Conference on the Physics and Chemistry of Semiconductor Interfaces, January 2004.
19. J.N. Gleason, M.E. Hjelmstad, R.S. Goldman, S. Fathpour, S. Ghosh, P.K. Bhattacharya, "Cross-Sectional Scanning Tunneling Microscopy Studies of Mn Segregation in GaMnAs Films", Oral Presentation at the Fall Meeting of the Materials Research Society, December 2003.
20. W. Ye, S. Hanson, M. Reason, X. Weng, and R.S. Goldman, "Stress Relaxation and Ordering of InAs/GaAs Quantum Dot Superlattices", Oral Presentation at the Fall 2003 Meeting of the Materials Research Society, December 2003.

21. A. Roshko, S.Y. Lehman, R.P. Mirin, K.D. Cobry, W. Ye, M. Reason, X. Weng, and R.S. Goldman, "Lateral and Height Distributions of Self-Assembled InGaAs Quantum Dots on GaAs Substrates", Oral Presentation at the Fall 2003 Meeting of the Materials Research Society, December 2003.
22. J.N. Gleason, M.E. Hjelmstad, R.S. Goldman, S. Fathpour, S. Ghosh, P.K. Bhattacharya, "Cross-Sectional Scanning Tunneling Microscopy Studies of Mn Segregation in GaMnAs Films", Oral Presentation at AVS International Symposium, November 2003.
23. W. Ye, S. Hanson, M. Reason, X. Weng, and R.S. Goldman, "Anisotropic Stress Relaxation and Ordering of InAs/GaAs Quantum Dot Superlattices", Oral Presentation at the 2003 International Symposium of the AVS Science and Technology Society, November 2003.
24. R.S. Goldman, B. Shin, W. Chen, A. Lin, K. Lappo, M.C. Hanna, S. Francoeur, A.G. Norman, A. Mascarenhas, J.D. Song, J.M. Kim, and Y.T. Lee, "Initiation and Evolution of Alloy Phase Separation in Heteroepitaxial Semiconductor Films", oral presentation at the International Conference on the Formation of Semiconductor Interfaces, Madrid, Spain, September 2003.
25. W. Chen, B. Shin, R.S. Goldman, A. Stiff, and P.K. Bhattacharya, "Mechanisms of Lateral Ordering of InAs/GaAs Quantum Dot Superlattices", Oral and Poster presentations at the Physics and Chemistry of Semiconductor Interfaces Meeting, January 2003.
26. B. Shin, W. Chen, A. Lin, K. Lappo, R.S. Goldman, M.C. Hanna, S. Francoeur, A.G. Norman, A. Mascarenhas, J.D. Song, J.M. Kim, and Y.T. Lee, "Mechanisms of Alloy Phase Separation in Heteroepitaxial Semiconductor Films", Oral Presentation at the 2002 Fall Meeting of the Materials Research Society, December 2002 (INVITED).
27. B. Shin, B. Lita, J.D. Phillips, P. Bhattacharya, and R.S. Goldman, "Indium-Indium Pair Correlations within the Wetting Layers of Buried InAs/GaAs Quantum Dots", Oral presentation at the Electronic Materials Conference, June 2002.
28. B. Shin, W. Chen, R.S. Goldman, J.D. Song, J.M. Kim, and Y.T. Lee, "Cross-sectional Scanning Tunneling Microscopy Studies of Phase Separation in InP/GaP Short Period Superlattices", Oral presentation at the Electronic Materials Conference, June 2002.
29. W. Chen, B. Shin, R.S. Goldman, A. Stiff, P.K. Bhattacharya, "Effects of Annealing on the Lateral Ordering of InAs/GaAs Quantum Dot Superlattices", Oral presentation at the Electronic Materials Conference, June 2002.
30. B. Shin, B. Lita, R.S. Goldman, J.D. Phillips, and P. Bhattacharya, "Indium-Indium Pair Correlations within the wetting layers of Buried InAs/GaAs Quantum Dots", Poster Presentation at the Materials Research Society Spring Meeting, April 2002.
31. B. Shin, A. Lin, K. Lappo, R. S. Goldman, M. C. Hanna, S. Francoeur, A. G. Norman, and A. Mascarenhas, "Evolution of Phase Separation in Heteroepitaxial InAlAs Films", Oral and Poster Presentations at the Physics and Chemistry of Semiconductor Interfaces Conference, January 2002.
32. B. Shin, A. Lin, K. Lappo, R. S. Goldman, M. C. Hanna, S. Francoeur, A. G. Norman, and A. Mascarenhas, "Nanometer-scale Studies of Phase Separation in Misfit-Free InAlAs Semiconductor Alloys", Oral Presentation at the Materials Research Society Fall Meeting, November 2001.
33. B. Shin, A. Lin, K. Lappo, R. S. Goldman, M. C. Hanna, S. Francoeur, A. G. Norman, and A. Mascarenhas, "Nanometer-scale Studies of Phase Separation in Compound Semiconductor Alloys", Oral Presentation at American Vacuum Society International Symposium, San Francisco, CA, Oct 2001.
34. B. Shin, A. Lin, R. S. Goldman, D. Mars, M. C. Hanna, S. Francoeur, A. G. Norman, and A. Mascarenhas, "Cross-sectional Scanning Tunneling Microscopy Studies of Phase Separation in III-V Compound Semiconductor Alloys", Poster Presentation at the Gordon Conference on Thin Film and Crystal Growth Mechanisms, Williamstown, Massachusetts, July 2001.
35. B. Shin, A. Lin, R.S. Goldman, M.C. Hanna, S. Francoeur, A.G. Norman, and A. Mascarenhas, "Cross-sectional Scanning Tunneling Microscopy Studies of Phase Separation in InAlAs Alloys", Oral Presentation at the International Symposium on the Formation of Semiconductor Interfaces, Sapporo, Japan, June 2001.

36. B. Shin, A. Lin, R. S. Goldman, M. C. Hanna, S. Francoeur, A. G. Norman, and A. Mascarenhas, "Cross-sectional Scanning Tunneling Microscopy Studies of Phase Separation in InAlAs Alloys", Oral Presentation at Electronic Materials Conference, Notre Dame, Indiana, June 2001.
37. B. Shin, A. Lin, K. Lappo, R. S. Goldman, D. Mars, M. C. Hanna, S. Francoeur, A. G. Norman, and A. Mascarenhas, "Nanometer-scale Studies of Phase Separation in Compound Semiconductor Alloys", Poster Presentation at the Spring Meeting of Michigan Chapter of the America Vacuum Society, Detroit, Michigan, May 2001.
38. Z.-K. Wu, H. Choi, T. Norris, S. Chakraborti, X. Su, and P. Bhattacharya, "Electron Dynamics in N-Doped In<sub>0.4</sub>/Ga<sub>0.6</sub>As/GaAs Quantum Dot Infrared Detector Structures," paper QTuK3 presented at QELS, Long Beach, 2006.
39. Z.K. Wu, H. Choi, T.B. Norris, A.D. Stiff-Roberts, and P. Bhattacharya, "Ultrafast Electronic Dynamics in Unipolar N-Doped InAs/GaAs Quantum Dot Structures," paper QThC6 presented at CLEO, Baltimore, 2005.
40. Z.-K. Wu, K. Kim, T.B. Norris, S. Ghosh, and P. Bhattacharya, "Ultrafast Carrier Dynamics in Tunneling Injection Quantum Dot Lasers," paper QTHI2, presented at QELS, Baltimore, 2003.
41. K. Kim, T.B. Norris, S. Ghosh, J. Singh, P. Bhattacharya, "Temperature-Dependent Carrier Distributions and Level Degeneracy in Self-Assembled Quantum Dots, " paper QthI6, presented at QELS, Baltimore, 2003.
42. Z.-K. Wu, A. Stiff-Roberts, P. Bhattacharya, and T.B. Norris, "Two-photon absorption in a quantum dot infrared photodetector," paper CthM11, presented at CLEO, Baltimore, 2003.
43. K. Kim, T. Norris, J. Singh, P. Bhattacharya, "Temperature-dependent transparency conditions and spatial degeneracy in self-organized quantum dots," paper WC4 presented at the OSA Topical Meeting on Ultrafast Electronics and Optoelectronics, Washington, DC, 2003.
44. W. Chen, B. Shin, R.S. Goldman, A.Stiff-Roberts, and P. Bhattacharya, "Mechanisms of Lateral Ordering of InAs/GaAs Quantum Dot Superlattices", Oral and Poster presentations at the *Physics and Chemistry of Semiconductor Interfaces Meeting*, January, 2003.
45. Z-K. Wu, K. Kim, T.B. Norris, S. Ghosh, and P. Bhattacharya, "Ultrafast Carrier Dynamics in Tunneling Injection Quantum Dot Lasers", *QELS*, Baltimore, MD, 2003.
46. K. Kim, T.B. Norris, S. Ghosh, J. Singh, and P. Bhattacharya, "Temperature-Dependent Carrier Distributions and Level Degeneracy in Self-Assembled Quantum Dots", *QELS*, Baltimore, 2003.
47. A.D. Stiff-Roberts, S. Chakrabarti, S.W. Kennerly, and P. Bhattacharya, "High Responsivity, Polarization-Sensitive, 70-layer InAs/GaAs Quantum Dot Infrared Photodetector", *Conference on Lasers and Electro-Optics*, Baltimore, MD June 2003.
48. S. Chakrabarti, A.D. Stiff-Roberts, P. Bhattacharya, and S. Kennerly, "Heterostructures for Achieving Very Large Responsivity in InAs/GaAs Quantum Dot Infrared Photodetectors", *North American Conference on Molecular Beam Epitaxy*, Keystone, CO, March 2003.
49. A.D. Stiff-Roberts, S. Chakrabarti, P. Bhattacharya, and S. Kennerly, "Tailoring of Quantum Dot Infrared Photodetector Performance with AlAs/GaAs Superlattice Barriers", *Lasers and Electro-Optics Society Meeting*, Tucson, AZ, October 2003.
50. "Self-Organized Semiconductor Quantum Dots and Their Application to Optoelectronic Devices", *Frontiers in Nanoscience and Nanotechnology*, Ann Arbor, MI November, 2003.
51. Z-K. Wu, H. Choi, T.B. Norris, A.D. Stiff-Roberts, and P. Bhattacharya, "Two-Photon Absorption in Quantum Dot Infrared Photodetector", *Quantum Electronics and Laser Science Conference*, Baltimore, MD June 2003.
52. S. Chakrabarti, X.H. Su, G. Ariyawansa, A.G.U. Perera and P. Bhattacharya, "Room Temperature Operation of Resonant Tunneling Quantum Dot Infrared Detectors", *Conference on Lasers and Electro-Optics (CLEO/QELS)*, Baltimore, MD, May 2005.
53. P. Bhattacharya, "Self-Organized Quantum Dots for Optoelectronics", *Nano-Optoelectronic Workshop*, University of California, Berkeley, CA, August 2005.

54. X. H. Su, S. Chakrabarti, P. Bhattacharya, G. Ariyawansa, and A. G. U. Perera, "A Tunnel Quantum Dot Infrared Photodetector", *The 8th International Conference on Intersubband Transitions in Quantum Wells*, Cape Code, MA, September 2005.
55. X. H. Su, J. Yang, P. Bhattacharya, G. Ariyawansa, and A. G. U. Perera, "Terahertz Detection With Tunneling Quantum Dot Intersubband Photodetector", *Device Research Conference*, State College, PA, June 2006.